INVESTIGATION OF 2D POLYMER THIN FILMS IN 3D STRUCTURES INVOLVING CRUMPLING, ORIGAMI, KIRIGAMI AND ADHESION

A Dissertation
Submitted to the Graduate Faculty
of the
North Dakota State University
of Agriculture and Applied Science

By

Wathsala Mayurika Amadoru Jayawardana

In Partial Fulfillment of the Requirements
for the Degree of
DOCTOR OF PHILOSOPHY

Major Department:
Physics

March 2024

Fargo, North Dakota

NORTH DAKOTA STATE UNIVERSITY

Graduate School

Title

INVESTIGATION OF 2D POLYMER THIN FILMS IN 3D STRUCTURES INVOLVING CRUMPLING, ORIGAMI, KIRIGAMI AND ADHESION

By

Wathsala Mayurika Amadoru Jayawardana

The Supervisory Committee certifies that this dissertation complies with North Dakota State University's regulations and meets the accepted standards for the degree of

DOCTOR OF PHILOSOPHY

SUPERVISORY COMMITTEE:

Prof. Andrew B. Croll
Chair

Prof. Silvio May

Prof. Mila Kryjevskaia

Prof. Kalpana S. Katti

Approved:

27 March 2024
Date

Prof. Silvio May
Department Chair

ABSTRACT

This dissertation delves into the fascinating world of thin films and their ability to transform into three-dimensional (3D) structures. One can simply crush a sheet of paper into a ball to make a 3D object a faster, yet more complex structure or by following a more organized folding technique (Origami) to create 3D objects with predictable structures. This dissertation mainly focuses on such 3D structures and introduces cuts (Kirigami) and adhesion to those 3D structures to understand more of their mechanical behavior.

The investigation of polymer crumple mechanics by introducing the Kirigami approach, and exploring how the sheet's topology influences crumpling, is discussed in this dissertation, which employs confocal microscopy, force experiments, and molecular dynamics simulations to investigate the effects of cutting on the behavior of crumpled sheets. The findings reveal that cutting does not significantly alter the compressive behavior; force scales according to a power law regardless of cuts, with only minor reductions in magnitudes.

The second chapter of this dissertation studies Origami-inspired adhesive capable of securely holding objects on a wall yet easily removable without damage, which should withstand significant forces when attached, and then swiftly transition to a low-adhesion state for removal. Bi-stability of the proposed Origami designs with different compliance to achieve noticeable switching ratios has been investigated. These devices demonstrate moderate switching ratios and scalability, offering the potential for arrayed applications through repetition of the Origami pattern.

Crumples combined with adhesion create stable 3D structures made from elastic thin sheets. The last chapter discusses the impact mitigation of such crumpling systems by observing sticky crumpled matter subjected to simple ball drop tests. These findings highlight the potential utility of sticky crumples as replacements for intricate engineered structures in protective layers.

ACKNOWLEDGEMENTS

I extend my deepest gratitude to my advisor, Professor Andrew B. Croll, whose mentorship and encouragement have been instrumental in shaping this thesis. His expertise, patience, and unwavering support have guided me through every step of this journey. His belief in my potential has been a constant source of motivation, and I am truly grateful for his invaluable insights and constructive feedback. His constant guidance shaped me into a better researcher, and presenter throughout these past six years.

I would like to thank my esteemed Ph.D. committee members: Professor Silvio May, Professor Mila Kryjevskaia, and Professor Kalpana S. Katti for their generous investment of time, insightful comments on my work, and multifaceted support that have been invaluable throughout my academic journey.

In expressing my gratitude, I extend heartfelt thanks to the members of the Croll research group whose efforts have significantly contributed to the fruition of this work. Especially Dr. Tim Twohig, Dr. Theresa Elder, Kurt VanDonselaar, and Leo-Stanley Ndunagum for being more than just lab mates and pouring me with friendship, guidance as well as all the valuable discussions. I would also like to extend my gratitude to all collaborators we worked with including Professor Wenji Xia, Dr. Yangchao Liao and Dr. Zhaofan Li.

I am deeply grateful to the Physics Department at North Dakota State University for providing a nurturing environment conducive to learning and research. Their unwavering support, resources, and collaborative spirit have been instrumental in shaping my academic journey. I extend my sincere appreciation to the faculty, staff, and fellow students for their guidance, encouragement, and all the volunteering and gathering events throughout these years. Apart from my committee, I would like to take a moment to thank Professor. Alan Denton for being an exceptional graduate student coordinator at the beginning of my graduate student years and for the constant support. A special mention goes to Dr. Brianna Santangelo

for being my swimming partner, Dr. Lina Alhalhooly for engaging lab conversations, Saffana Ismeal for her adept organization of girls' gatherings, and to Sakurako Tani, Mahesh Aryal, and Eric Roeschlein for the memorable escapades. Your presence has made my experience as a graduate student truly unforgettable.

I want to extend my heartfelt gratitude to my dear friends, who have been an unwavering source of encouragement and inspiration throughout this journey. I am immensely grateful to Casey, Courtney, Charlie, Isamar, and Pam for being my first circle of friends in Fargo, the countless gatherings, meals, game nights, and hangouts that have filled my days with joy and laughter. To Katie, Merrit and the whole Hall-Carlson family, your warm embrace and hospitality have made me feel like part of your family, especially during American holiday celebrations and for letting me have a therapy time with my adorable paw friends Buddy, Champ and River. Special thanks to Chamari Idamawatta and Waruna Kalanchige for their constant friendship, unwavering support and being siblings away from homeland. Heartfelt gratitude to Dr. Vishwa Dewage and Dr. Sadisha Nanayakkara, my high school besties in the States, who always sharing grad-student tips and lifted my spirits whenever needed. To my soul sister, Prathibha Udayakantha and my beloved UoC besties Boku, Ju, and Nu, your group birthday calls have been a highlight of each year. APS-UoC buddy Piumi Samarawickrama for all the good times. Middle school bestie Dilsi Rangika and all my high school besties -Manushi Wijayapala, Thila, Hassa, Dus, Piyu, Himz, Nipz, Upz, Vinu, Menu, Ishi, Sabi, Era, Gath, Dulashani and her baby Amy - their friendship, chit-chats, special celebration gifts, cards and calls have been a constant source of joy and comfort. I am grateful for the cherished memories we've shared and still keeping in touch.

I want to dedicate this heartfelt gratitude to my beloved husband, Dr. Chanaka Bulathsinghalage, whose unwavering companionship and unwavering belief in me have been the cornerstone of my journey. His constant support and unwavering presence have been my greatest sources of strength and inspiration. Equally, I am profoundly indebted to my cherished family, especially my mother, Nihathamani, my sister, Uthpala, my brother, Chethiya, and my in-laws Chandra and Hemasiri Cooray, my closest relatives Chutiamma Nilmini, Mama and Bonju Dahamdee for their boundless love, unwavering support, and profound understanding throughout this remarkable journey. Their endless encouragement, patience, and sacrifices have laid the foundation upon which I've pursued my academic ambitions. Their presence in my life is a cherished blessing, and I am forever grateful for their enduring love and support.

Finally, I'd like to express my heartfelt gratitude to everyone who has supported and encouraged me throughout my journey I wish I had more space to spare to individually thank each person. I'm immensely grateful to my professors, mentors, and friends at the University of Colombo, Sri Lanka. I owe a debt of gratitude to all my teachers from kindergarten through high school, as well as my colleagues and managers from my previous workplaces I had fun working with. I deeply appreciate the countless others who have played a role in shaping my path including all the relatives, and friends who always wish me success. Lastly, I want to thank all US funding agencies who funded my research, NDSU Physics and NDSU Graduate School for funding me as a Teaching Assistant, Awards and for Tuition waivers. And all the taxpayers in my small motherland Sri Lanka who funded my education all the way through to my bachelor's degree. I am proud to say that I am a product of free education, and I did my best to give the highest possible value to their hard-earned money by achieving the most I could from my education. This achievement would not have been possible without their investment in my future.

DEDICATION

This thesis is dedicated to my mom, whose belief in my potential as a scientist since my 4th grade and to my life partner CC for always believing in me through thick and thin.

TABLE OF CONTENTS

LIST OF TABLES

LIST OF FIGURES

LIST OF ABBREVIATIONS

NDSU	North Dakota State University
PDMS	Polydimethylsiloxane
PC	Polycarbonate
PAA	Polyacrylic acid
1D	One dimensional
2D	Two dimensional
3D	Three dimensional
kPa	Kilo Pascal
MPa	Mega Pascal
GPa	Giga Pascal
N	Newtons
D-cone	Developable cone
DNA	Deoxyribonucleic acid
MEMS	Microelectromechanical systems
°C	Degrees Celsius
G_c	Critical energy release rate
cos	cosine
E	Young’s modulus
nu	Poisson ratio
COR	coefficient of restitution
m	meter(s)
cm	centimeter(s)
mm	Millimeter(s)
μm	Microometer(s)
NI DAQ	National instruments data acquisition device
CAD	computer-aided design

SLA	stereolithography
CG-MD	coarse-grained molecular dynamics
LAMMPS	Large-scale Atomic/Molecular Massively Parallel Simulator

LIST OF SYMBOLS

A	Area (m^2)
$\mathscr{F}$	Helmholtz free energy
π	22/7(3.14159265359)

LIST OF APPENDIX TABLES

LIST OF APPENDIX FIGURES

1. BACKGROUND

1.1. Introduction

1.1.1. From 2D to 3D

When a film's thickness is significantly smaller than its length and width (1), it is categorized as a 2D structure and commonly referred to as a thin film. Thin films can be transformed into three-dimensional (3D) structures by introducing phenomena such as buckling, and folding (2). Buckling occurs when a thin film is subjected to compressive or bending forces, resulting in the formation of out-of-plane deformations (1; 3). Buckling can be observed in a variety of systems, including thin film microbeams (3), thin film shells (4), the petals of flowers(5), crumpled paper (6)and even the skin of elephants (7). Folding is the process of fixing a 3D object from a 2D sheet by forcing bends to a specific location (1; 8). Folding can be used to create complex 3D structures, such as origami and origami-inspired robots (9).

Nature, across a dazzling array of scales, showcases the power of transformation through thin-film mechanics ranging from atomic scales, such as the formation of wrinkles in graphene (10), to nano scales, such as the buckling of carbon nanotubes (11), and progressing to micro scales, such as the folding of insect wings (12), and even extending to macro scales, such as the formation of wrinkles in the Earth's crust (13). Furthermore, these phenomena are not limited to our terrestrial realm; they can be observed on astronomical scales as well, such as the buckling of the solar corona (14). The study of thin film mechanics is a captivating field that offers a multitude of physical phenomena ripe for exploration and the application of physics principles. By understanding the mechanics of thin films, researchers can develop new structures and devices with unique properties and functionalities.

Origami('ori', fold; 'kami', paper) is the ancient Japanese art of paper folding (15), where intricate and beautiful sculptures are created by folding a single sheet of paper, without cutting or gluing. It's a captivating blend of mathematics, creativity, and precision that has evolved over centuries allowing the creation of simple paper cranes and complex geometric shapes. Origami not only serves as a creative outlet but also finds applications in various fields, such as science and engineering (16), where it inspires innovations in deployable structures and space exploration (17), to medical applications(18). This timeless art form inspires and connects people across cultures, reminding us of the immense beauty that can emerge from the simplest of materials and techniques.

Crumples, on the other hand, can be identified as a complex origami system with disordered folding and bending pattern with randomly arranged d-cones, folds and ridges. Making a crumple is an easy act compared to folding an origami pattern, yet understanding the physics behind it is more complex than understanding origami. The volume of a spherical crumple can be more than 75% air (19), yet the crumpled paper ball is very rigid. Scientists have focused on studying crumples because of the complexity of these structures and the extraordinary strength they hold compared to a flat sheet of thin paper.

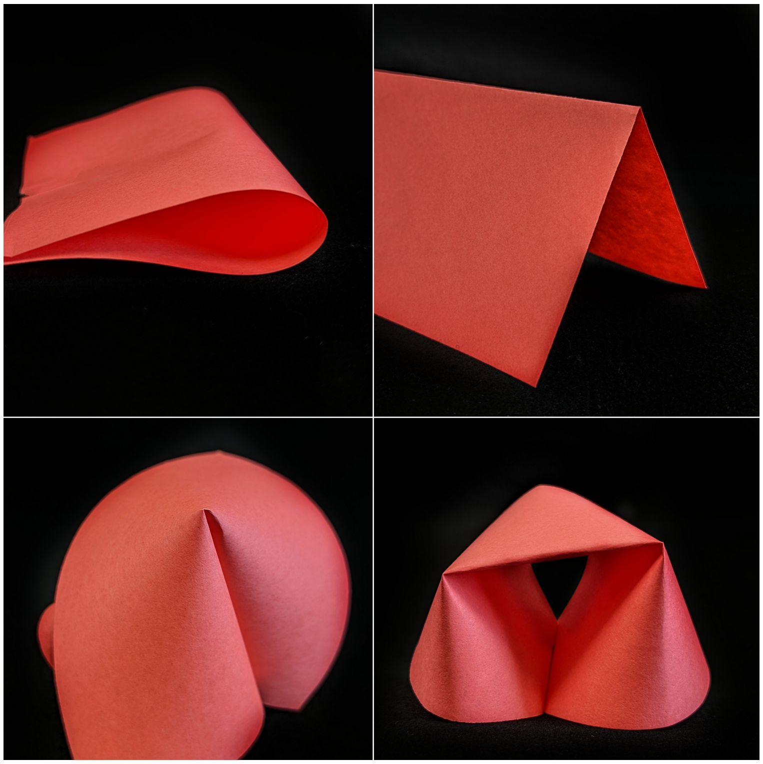

Figure 1.1. Basic structural features of a crumple. a) Bend b) Fold c) D- cone d) Ridge

When we make 3D structures out of 2D thin films we can identify basic structural features associated with ordered folding patterns in origami and disordered complex folding patterns in crumpling structures. Understanding the cause of the rigidity in crumples or the actuation of origami mechanisms requires identifying the basic structural features that occur in those 3D structures. The structure consists of 4 structural “building blocks” - folds, ridges, bends, and point-like peaks (D-cones) (20). A bend is defined as a region of the film where the radius of the curvature is larger than its thickness (1.1a). A sharper bend where plastic damage has occurred is a fold (1.1b). The plasticity will lead to memory formation in the original film. A point-like peak is called a D-cone(1.1c). More accurately, a developable cone (D-cone) is a conical dislocation in the structure due to localized stretching at the peak of the cone. A ridge is a smooth structure that joins two D-cones (1.1d).

1.1.2. Models of Crumple Compressibility

There are three basic models developed to understand the rigidity of a crumpled sheet. These models include a model based on ridges, a model based on folds and a model favouring d-cones and their motion. In the following sections we describe each in detail.

1.1.2.1. Model of Ridges

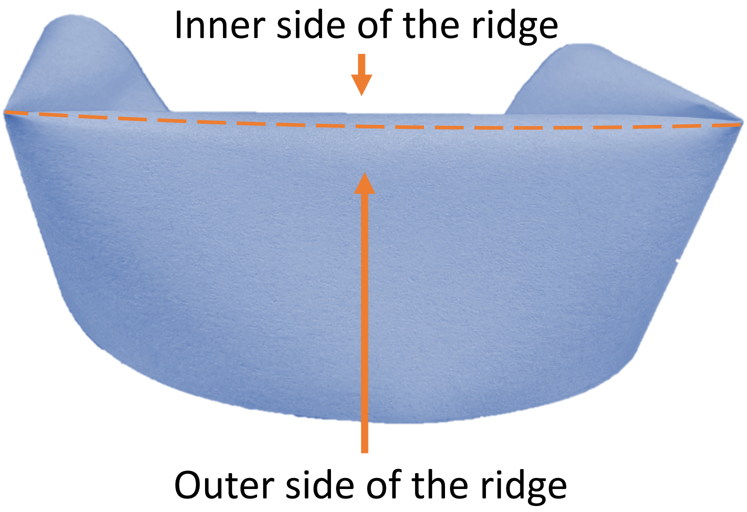

Figure 1.2. A ridge created in-between two d-cones. Crest of the ridge, where the stretching occurs shown by a dashed lines.

Compared to fold where radius of the curvature of the film is very close to it thickness, ridges between two developable cones (d-cones) contain finite radius of curvature which is higher than a simple fold. If a person crushes a lightly crumpled paper into more tight ball, comparatively long-range structural features such as ridges will break into much smaller ridges as confinement increases. Matan et al (19) proposed the model of ridges based on the assumption that the ridges are the dominant energy storing structures and that they will break into smaller ridges as compression is added.

They used a large circular sheet of Aluminized mylar which they crumpled for their experiment. The crumpled ball was placed inside a cylindrical cell that has a weighted piston. Their 1st experiment was to find the equilibrium height for a fixed mass on top of the piston. They obtained some time-dependence logarithmic results to the Mylar height(h) during the entire duration of the experiment,

$$h = a - blog(t)$$

where a and b are constants. In the next part of their experiment, they varied mass to apply increasing forces to the crumple while measuring the gap height. They came up with a power-law function to describe how the force depended on the gap height. This power-law function has a negative value as the exponent of plate separation. The model also predicted a negative exponent. In detail, the model predicted

$$F \sim Et^{8/3}R^{-10/3}L^{16/3}H^{-8/3} \tag{1.1}$$

In this equation, F is Force, E is Young's modulus, t is the film thickness, R is the spherical radius of the crumple, L is the average length of the film and H is the cell gap (19).

1.1.2.1.1. Derivation for the above equation 1.1

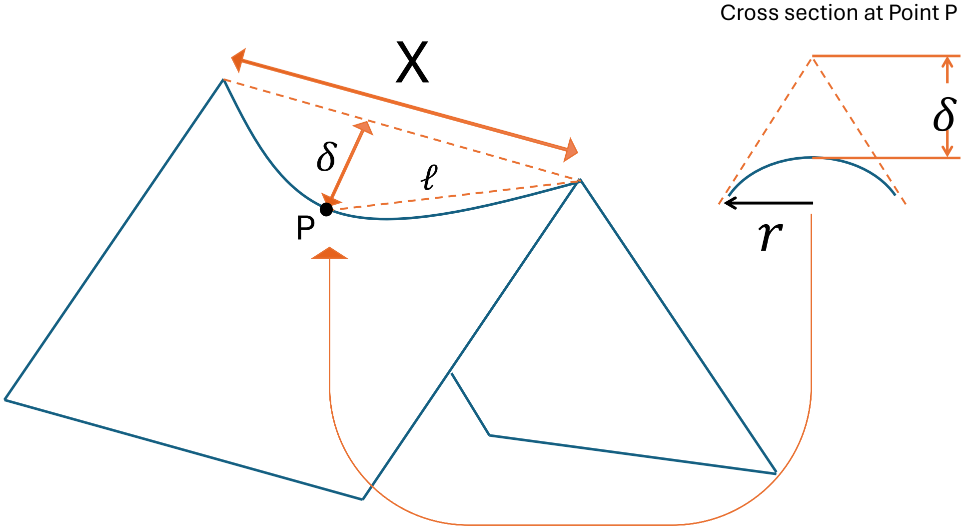

Figure 1.3. A thin film with thickness t creating a ridge between two D-cones with length X and deflected down by length δ

Due to the stretching that occurs at the ridge, ridge length X stretched to the length 2ℓ.

By simple trigonometry,

$$\ell = \sqrt{\delta^2 + (\frac{X}{2})^2}$$

by simplifying,

$$\ell = \frac{X}{2}\sqrt{\frac{\delta^2}{X^2} + 1}$$

this result can be expanded in a Taylor series which simplifies to,

$$\ell \sim X(1+\frac{\delta^2}{2X^2}+...)$$

as $\frac{\delta}{X}$is $\ll 1$ we can drop higher than second order terms which simplifies to,

$$\ell \sim X + X\frac{\delta^2}{2X^2}$$

The strain of the bending ridge is given by,

$$\epsilon = \frac{L-L_0}{L_0} = \frac{2\ell - X}{X} \sim \left(\frac{\delta}{X}\right)^2$$

The radius of curvature r grows linearly with distance from the vertex. From the geometry, $\delta \sim r \sim \frac{1}{C}$ where C is the characteristic ridge curvature. If X is the length of a ridge, then the characteristic strain $\epsilon = (XC)^{-2}$ (21). Total Stretching energy then be written as:

$$U_s \sim Et \int \epsilon^2 dA \sim EtX^{-3}C^{-5}$$

where dA denotes the surface integration elements. Similarly energy in a bending ridge given by the characteristic ridge curvature C can be written as(22)(23),

$$U_b \sim \kappa \int C^2 dA \sim \kappa C^2 \frac{X}{C} \sim CX\kappa$$

where κ is the bending modulus. Minimizing the total energy yields, $C \sim t^{-\frac{1}{3}}X^{-\frac{2}{3}}$ .Then the energy per ridge is given by,

$$U_{ridge} \sim Et^{\frac{8}{3}}X^{\frac{1}{3}}$$

and the force per ridge given by,

$$F_{ridge} \sim Et^{\frac{8}{3}}X^{-\frac{2}{3}}$$

If assume a small volume fraction with a uniform network of ridges with ridge-length X between nearly flat facets and if facets are randomly orientated such that 1 facet per X^3 volume. Then the energy contain in the volume V(24),

$$U_{crumple} \sim \frac{V}{X^3}Et^{\frac{8}{3}}X^{\frac{1}{3}}$$

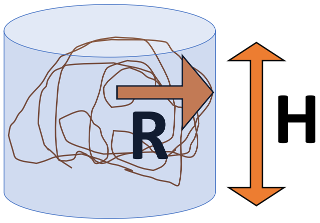

Figure 1.4. Crumple made with a sheet with dimensions L x L confined in a cylinder with radius R and height H

If space occupied by one facet is large enough to contain stack of X/t facets, volume fraction $\phi = \frac{t}{X}$. By assuming a cylindrical volume, macrosopically $\phi = \frac{tL^2}{\pi R^2 H}$. Then the energy of the crumple given by,

$$U_{crumple} \sim Et^{\frac{8}{3}}R^{-\frac{10}{3}}L^{\frac{16}{3}}H^{-\frac{5}{3}}$$

And the force to compress the crumple given by,

$$F \sim E t^{\frac{8}{3}} R^{-\frac{10}{3}} L^{\frac{16}{3}} H^{-\frac{8}{3}} \tag{1.2}$$

1.1.2.2. Model of Folds

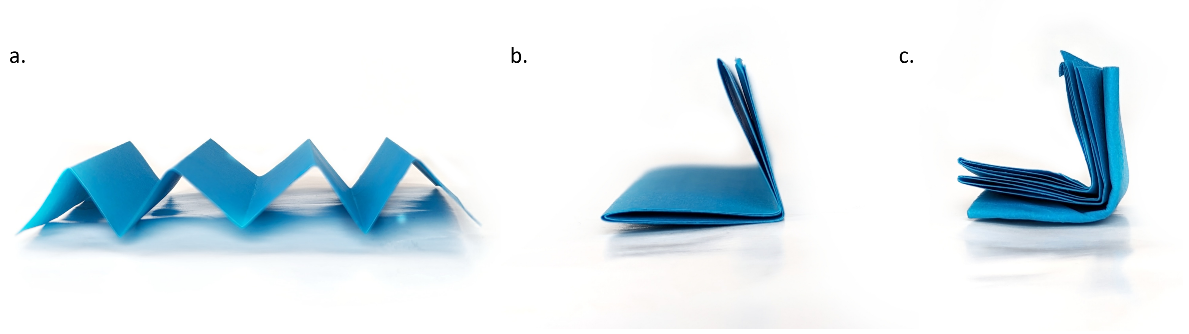

Figure 1.5. 1D, 2D and 3D folding of the sheets. (a) 1D like sheet folded in 1D; (b) 1D like sheet folded in 2D; (c) 2D like sheet folded in 3D

If a person folds a paper in half and keeps repeating the process, the maximum number of folds that a paper can have are either five or six and it is independent of the size of the sheet (25). This is because the elementary force needed to create a unique fold into two grows exponentially with the increasing number of folds. For a sheet folded n times, the energy balance gives,

$$F(n) \sim \frac{B_n}{h_n} \sim F_0 2^{2n}$$

Where B is the bending rigidity and h is the width. No one can fold a paper in half an infinite number of times because of this power-law growth of the required force.

One can think about other ways of folding a paper which is different than repeated half folding. In the case of Figure 1.5(a) paper folded back and forth(like a paper fan origami) along the same axis (width direction) while not folding orthogonally to this (length direction). Hence a 1D like folding of the sheet. In the case of Figure 1.5(b) the paper is folded in half repeatedly, doubling in thickness on each fold. Again, the lenth direction remains unchanged.Hence a 2D like folding. In the case of Figure 1.5(c) the paper is folded along both length and width direction resulting in increasing thickness, decreasing both length and width. Hence a 3D like folding. Generic power-law functions for the force for these three different types of folding are,

$$\begin{aligned} F_a(N) &= F_0 N \sim F_0 \phi \\ F_b(N) &= F_0 N^2 \sim F_0 \phi^2 \\ F_c(N) &= F_0 N^4 \sim F_0 \phi^4 \end{aligned} \tag{1.3}$$

Where ϕ is the compaction ratio ($\phi = initialsize/finalsize$) and, N is the number of folded layers and the subscripts indicate the different folding configurations shown in figure 1.5.

Deboeuf et al proposed a crumple model based on the hypothesis that the most dominant structural feature in crumpling is a fold. They also conducted experiments on crumples made out of kraft and regular printing papers for their studies (25). They used a power-law function to fit their experimental results.

$$F \sim Et^2 \frac{L}{H}^{\alpha}, 1 \leq \alpha \leq 4 \tag{1.4}$$

Here the new variable alpha is the negative exponent of H which has a range of possible values between one and four in order to account for the different types of folding discussed above.

They took into account that the process of making a fold is irreversible. They also neglect the other possible contributions from the short-range structures. To connect the model of successive folding to the crumpling model, they experimentally show that the crumpling data also follows a power-law function similar to their prediction. In their experiment, they place those crumples inside a rigid cylindrical cell with a piston to apply force. Force applied at a constant speed and the piston to cell bottom distance was measured.

1.1.2.3. Model of D-cones

Crumpling a piece of paper creates plastic damage. The sheet is not the same sheet of paper after uncrumpling due to this damage. However, an elastic sheet can be uncrumpled after crumpling and will return to the same initial state as there is no damage.

Polydimethylsiloxane(PDMS) is a soft elastomer polymer. By examining a PDMS crumple under the confocal microscope, Croll et al. (20) observed that there are no significant amounts of sharp folds inside the elastic crumple. By comparison with the previous ridge and fold models, they concluded that each model was insufficient to quantitatively describe the crumpling process and the most likely dominant feature affecting the rigidity of a crumple was the short-range structures such as the D-cones.

Croll et al. (20) proposed a new emperical power-law function which was assumed to be caused by the D-cones are the most dominant feature affecting the rigidity of a crumple (20). In the proposed function, a negative exponent (α) is a variable but depends on the material used. To be exact, PDMS has a different range of exponent alpha ($\alpha_{PDMS} = 2.8 \pm 0.5$) while the Polycarbonate(PC) a rigid polymer which can plastically deform has another completely different range of alpha values($\alpha_{PC}(compression) = 7.7 \pm 5$ and $\alpha_{PC}(retraction) = 14.0 \pm 13.6$). Explicitly, the function predicted is given as:

$$F = Et^2\left(\frac{2R_0}{H}\right)^{\alpha}, \tag{1.5}$$

Here the new variable R_0 is the spherical radius of the crumple.

1.1.2.4. Basic Compression Test

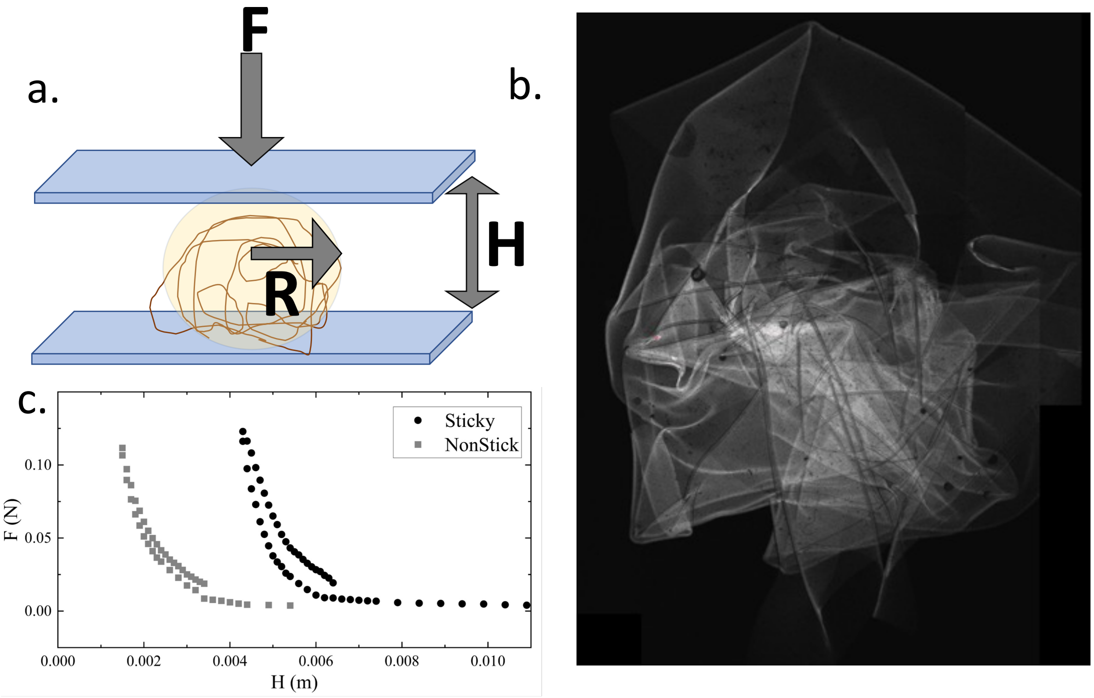

Figure 1.6. a) Experimental setup diagram b) Confocal image of a crumple c) Basic experimental outputs-Force displacement data for one sticky and one non-sticky crumple

To get compression and retraction curves for a crumpled sheet, we first start the experiment following the same procedure as was previously described in (20). A typical experimental setup is shown in Figure 1.6. The sticky crumple shown in this figure is made out of PDMS with a 10 : 1 crosslink ratio and the thickness of the film is between 50 μm to 100 μm. Thin films for this experiment were created by using the spin coating method. This experiment is designed to find the force response of the polymer crumple with compression and retraction cycles. Properly dried square-shaped films are crumpled by hand. There is no exact procedure for crumpling to ensure it is always a random collection of folds and bends. After the crumple arrives at an approximately spherical shape, it is loaded between two parallel plates of glass. Then the glass plates were moved close to each other until some critical force value was reached. The motor then reverses direction and retracts until the force drops to zero.

1.2. Materials

1.2.1. Material Properties

Stress in mechanics goes beyond just external forces. While a chair groaning under weight exemplifies this concept, internal forces can also create stress within a body. Imagine a compressed spring with fused coils; even without external pressure, the coils exert forces on each other, creating internal stress.This phenomenon is fundamental in diverse fields. Internal stress from manufacturing can impact material properties, while techniques like annealing can manipulate it to tailor behavior. Recognizing and analyzing internal stress empowers engineers to design robust structures and materials scientists to optimize material functionalities. Simply the stress(σ) is the internal force(F) acting on a material per unit area (A) is given by,

$$\sigma = \frac{F}{A}, \tag{1.6}$$

Stress is often denoted by a tensor. The stress tensor is typically represented as a second-order tensor, which is a mathematical object that can be thought of as a matrix of values. In three-dimensional space, the stress tensor is a 3x3 symmetric matrix, denoted by σ, with components σ_{ij}, where i and j represent the coordinate axes:(26)

$$\sigma = \begin{bmatrix} \sigma_{xx} & \sigma_{xy} & \sigma_{xz} \\ \sigma_{yx} & \sigma_{yy} & \sigma_{yz} \\ \sigma_{zx} & \sigma_{zy} & \sigma_{zz} \end{bmatrix} \tag{1.7}$$

Each component of the stress tensor represents the force per unit area acting on a plane with a specific orientation within the material or fluid. For example, σ_{xx} represents the force per unit area acting on a plane perpendicular to the x-axis, σ_{xy} represents the force per unit area acting on a plane oriented at an angle to the x-axis and y-axis, and so on.

Deformation, the essence of altering a body's shape and displacing its constituent particles, lies at the heart of understanding mechanical behavior. However, when it comes to quantifying this deformation, we focus solely on position-dependent displacements. This distinction arises because simple rigid-body translations, where all particles move identically, do not involve intrinsic deformation. Strain, therefore, serves as a precise measure of localized distortions within a body subjected to external forces or internal stresses. By meticulously analyzing how particle displacements vary across the body's interior, we gain insight into the nature and extent of its deformation. This paves the way for predicting potential failures, assessing structural integrity, and ultimately engineering materials with desired response characteristics. Strain(ϵ) can be denote by(26),

$$\epsilon = \frac{l-L}{L} = \frac{\Delta l}{L}, \tag{1.8}$$

where, L is tye equilibrium length and l is the deformed length in one dimension. In 3D strain also can be represent by a strain tensor(components ϵ_{ij}) similar to the stress tensor.1.7

If we consider an isotropic linear elastic material, we can interpret the hook's law as follows,

$$\sigma_{ij} = \lambda \delta_{ij} \epsilon_{\alpha\alpha} + 2\mu \epsilon_{ij} \tag{1.9}$$

or,

$$\epsilon_{ij} = \frac{1}{E}[(1-\nu)\sigma_{ij} - \nu \delta_{ij} \sigma_{\alpha\alpha}] \tag{1.10}$$

where, σ_{ij} is elements of the stress tensor, ϵ_{ij} is elements of the strain tensor, $\epsilon_{\alpha\alpha}$ is volumetric strain, $\sigma_{\alpha\alpha}$ is equal to mean stress times 3, $\delta_{ij} = 0(i \neq j), 1(i = j)$ and the constants(λ and μ) in equation1.9 represent Lammé coefficient and shear modulus respectively and constants (E and ν) in equationm1.10 represent Young's modulus and Poisson ratio respectively.

With these relationships, we can define some other useful moduli such as, Bulk Modulus **K:**Ratio between hydrostatic stress σ_0 to the volumetric strain, ($\sigma_0 = \frac{1}{3}\sigma_{\alpha\alpha} = K\epsilon_{\alpha\alpha}$). Compliance **C:** as the reciprocal of the bulk modulus ($C = \frac{1}{K}$). Shear Modulus μ:Ratio between shear stress to the shear strain.($\sigma_{ij} = 2\mu\epsilon_{ij}$, $i \neq j$)(27).

Young's modulus(E) is a measure of a material's stiffness. It is defined as the ratio of stress(σ) to strain(ϵ) in the elastic region of the material's stress-strain curve. The elastic region is the region of the stress-strain curve where the material deforms reversibly, meaning that it will return to its original shape when the stress is removed.(28–30) It is defined as the ratio of extensional stress to the intentional strain in a uniaxial stress($\sigma_{xx} = \sigma_{yy} = \sigma_{xy} = \sigma_{xz} = \sigma_{yz} = 0$) and it is always positive(27).

$$E = \frac{\sigma_{zz}}{\epsilon_{zz}} \tag{1.11}$$

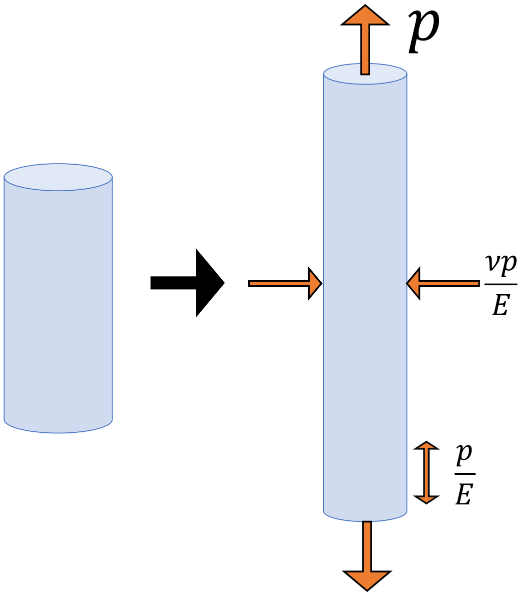

Figure 1.7. Traction(p) of a bar to interpret Young's modulus E and poison ratio ν

Poisson's ratio (ν), also known as the lateral strain ratio, is a measure of the transverse contraction or expansion of a material when it is subjected to a longitudinal stress. Poisson's ratio is a dimensionless quantity and its value ranges from -1 to 1/2. Materials with a Poisson's ratio of 1/2 are said to be incompressible, meaning that their volume does not change when they are subjected to stress. Materials with a negative Poisson's ratio are said to be auxetic, meaning that they expand in the transverse direction when they are subjected to longitudinal stress. Poisson's ratio is an important property of materials for many engineering applications. For example, it is important to consider Poisson's ratio when designing structures that will be subjected to high stresses.(28–30) Poisson ratio for the uniaxial strain state($\epsilon_{xx} = \epsilon_{yy} = \epsilon_{xy} = \epsilon_{xz} = \epsilon_{yz} = 0$) can be simply defined as(27),

$$\nu = -\frac{\epsilon_{xx}}{\epsilon_{zz}} \tag{1.12}$$

Table 1.1. Young's modulus(E) and Poisson Ratio(ν)of some materials

Material	E(GPa)	ν
Steel	200	0.29
Copper	110	0.34
Aluminum	70	0.33
Glass	65	0.23
Concrete	48	0.20
Plastic	1-10	0.3-0.4
Rubber	0.01-0.1	0.5

Plasticity is the property of a material to deform permanently when subjected to stress beyond its yield stress. The yield stress is the stress at which the material begins to deform plastically. Plastic deformation is irreversible, meaning that the material will not return to its original shape when the stress is removed. Plasticity is an important property of many materials, including metals, polymers, and ceramics. It allows these materials to be deformed into different shapes without breaking. Plasticity is also important for many manufacturing processes, such as forging, rolling, and extrusion.(28–30)

1.2.2. Polymers

Polymers are also known as macro-molecules and they are composed of a large number of smaller repeated liked units, monomers, arranged in a long chain similar to a string of beads (31). There are some naturally occurring polymers such as natural rubber, DNA as well as synthetic polymers such as polyethylene. Polymers have unique physical and chemical properties and hence they are used in different kinds of medical and engineering applications as well as commercial products. In this work, mainly two different polymers are used.

Elastomers, boasting remarkable elasticity and resilience, are a class of polymers renowned for their ability to recover their original shape after significant deformation. This unique property, attributed to their long, cross-linked polymer chains, fuels their diverse applications across industries. Polydimethylsiloxane (PDMS) is a silicone polymer with the chemical formula $(CH_3)2SiO$ and commercially known as sylgard 184. Elastomer base is a liquid at room temperature. Cured cross-linked PDMS has some special features such as hydrophobicity, optical transparency, bio-compatibility, adhesion, flexibility, contamination resistance, long-term endurance, and availability for a low price. PDMS is is often used as a protective coating such as in electrical insulation, anti-corrosion, and anti-fouling coatings (32). It is widely used in fabricating microfluidic devices (33–36), microelectromechanical systems(MEMS)(37), as well as soft lithography stamps and molds (38). The curing temperature of the bulk Sylgard 184 is between 25 °C to 200 °C and Young's modulus of the PDMS croslinked 10:1 ratio is in between 1.32 to 2.97 MPa according to the curing temperatures (39; 40).

Polycarbonate (PC) is a thermoplastic material that has some unique properties such as optical transparency, low weight, and some other special electrical and mechanical properties. PC is used in optoelectronic devices as a replacement for inorganic glass substrates, flexible displays, touch panels, etc (41). Glass transition temperature T_g of the PC is $145C$ (42). The curing temperature for the PC is above T_g and it is around 200 C and the Young's modulus of the PC is around $2.0-2.6$ GPa (42–47).

We choose those two materials because of their contrasting material properties especially because of the plasticity of PC and elasticity of PDMS elastomers. The huge difference in modulus allows dependant outcomes to be easily and quickly determined leading to a better understanding of various structures for engineering applications.

1.2.3. Adhesion

Adhesion is the force required to separate two dissimilar surfaces. These forces can originate from different types such as mechanical, physical or chemical. **Mechanical bonding:**This occurs when two surfaces have rough or irregular textures that interlock with each other. For example, Velcro adhesive tapes use these kinds of mechanical interlocking for adhesion. **Physical bonding:**This occurs when two surfaces are held together by intermolecular forces, such as hydrogen bonds, van der Waals forces, and electrostatic forces. For example, water adheres to glass because of hydrogen bonds between the water molecules and the glass surface(48) and insects and geckos climb walls using van dar walls forces(49–63) **Chemical bonding:**This occurs when two surfaces are held together by permanent chemical bonds. For example, epoxy adhesive (64) forms covalent bonds with the surfaces it is applied to, creating a strong bond.

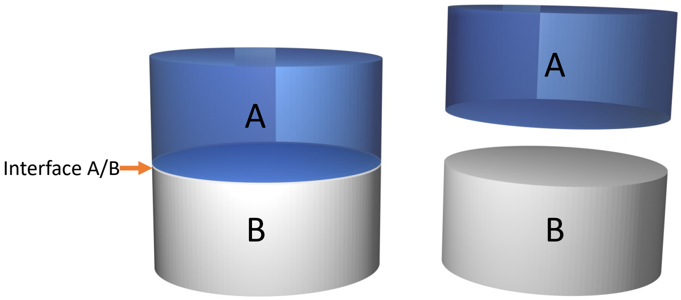

Figure 1.8. Work of adhesion to separate two different surfaces A and B adhered together

When two bodies come into contact with one another, a new interface is created with interfacial energy γ_{AB}. To separate them again will require input of the thermodynamic work of adhesion described by Dupré,

$$w = \gamma_A + \gamma_B - \gamma_{AB}$$

where γ_A and γ_B are the surface energies of two bodies and γ_{AB} is the energy of adhered interface as discussed in (65). Interfacial surface energy is given by,

$$U_S = -wdA = -(\gamma_A + \gamma_B - \gamma_{AB})dA$$

At constant temperature, the variation of Helmholtz free energy $\mathscr{F}$ is equal to the variation of total energy U_T or,

$$d\mathscr{F} = dU_T = dU_E + DU_P + dU_S, \tag{1.13}$$

where U_E is the elastic energy and U_P is the potential energy.

1.2.3.1. Energy Release Rate and Critical Energy Release Rate G_c

We can define the energy release rate as,

$$G = \left(\frac{\partial U_E}{\partial A} + \frac{\partial U_P}{\partial A} \right)$$

Variation of free energy in spontaneous evolution is,

$$d\mathscr{F} = dU_T = (G - w)dA \tag{1.14}$$

Equilibrium occurs at $G = w$, which can be defined as the critical energy release rate G_c.

1.2.3.2. Pull-Off Test (66)

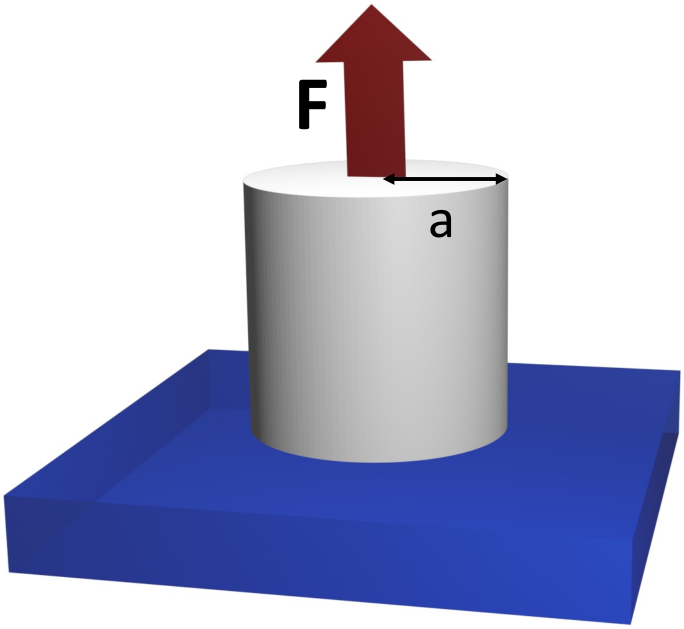

Figure 1.9. Rigid post with radius a pulling off from an adhesive elastic material with modulus E and poison ratio ν with a force F

Consider a rigid post with radius a, pulling off with force F from an elastic substrate while the elastic deformation is $\delta = \frac{F}{2\overline{E}a}$ and with the effective modulus, $\overline{E} = \frac{E}{(1-\nu^2)}$. Then the surface energy of the system is,

$$U_s = -G_c \pi a^2$$

The elastic energy of the system is, $U_E = \int F d\delta$. By substituting $F = 2\overline{E}a\delta$,

$$U_E = \int 2\overline{E}a\delta d\delta$$

Which can easily be integrated to find $U_E = \overline{E} a \delta^2$. Or more simply,

$$U_E = \frac{F^2}{4\overline{E}a},$$

The potential Energy of the system is,

$$U_P = -F\delta$$

Where C is an arbitrary constant or,

$$U_P = \frac{-F^2}{2\overline{E}a}$$

The total energy of the system is given by $U_T = U_S + U_E + U_P$ and equilibrium fracture at constant F, can be determined by setting the areal derivative to zero,

$$\frac{dU_T}{da} = 0 = -2\pi G_c a + \frac{F^2}{4\overline{E}} a^{-2}$$

Simplifying we find $F^2 = 8\pi \overline{E} G_c a^3$. In terms of adhesive force capacity at failure,

$$F = \sqrt{8\pi \overline{E} G_c} a^{\frac{3}{2}} \tag{1.15}$$

1.2.3.3. Peel Test

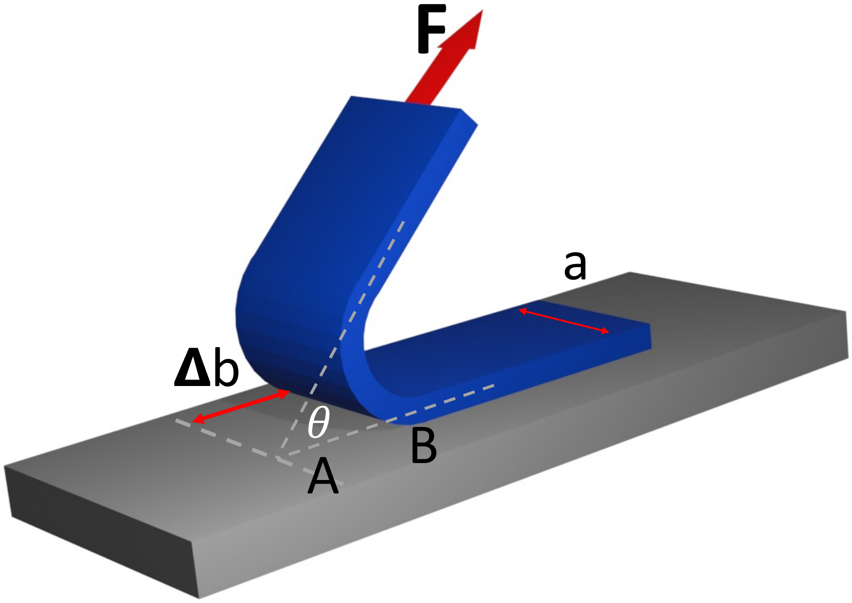

Figure 1.10. A soft rectangular adhesive substrate with thickness t, width a and length b, progressively peeling with force F with an angle θ to the adhered surface

Consider the energy changes of a soft elastic adhesive substrate with length b, width a, and thickness t as it peels a distance Δb between point A and B. Then the change in surface energy for the system will be,

$$U_s = -G_c a \Delta b$$

the elastic energy stored as the strip stretches is given by,

$$U_E = \frac{F^2 \Delta b}{2aEt}$$

the potential energy as the point where the load is attached moves is given as,

$$U_P = F(1 - cos\theta)\Delta b$$

the total energy of the system is given by $U_T = U_S + U_E + U_P$ and in equilibrium total energy $U_T = 0$,

$$0 = \left(\frac{F}{a}\right)^2 \frac{1}{2Et} + \left(\frac{F}{a}\right)(1 - cos\theta) - G_c$$

and the peel force can be found by solving the quadratic. We can simplify by noticing the first term of this quadratic equation goes to zero as stress $\frac{F}{at} \ll E$, and at $\theta = \frac{\pi}{2}$, the middle term becomes $\frac{F}{a}$. Under these assumptions adhesive force capacity at failure given by,

$$F = G_c a \tag{1.16}$$

for the 90° degrees peel test.

1.2.4. Impacts

When one object forcibly comes into contact with another object can be defined as an impact. Impacts can happen on different scales (67–69), but in this thesis, the main focus is to study how macroscopic free fall impacts act on different polymers/ thin film crumples.

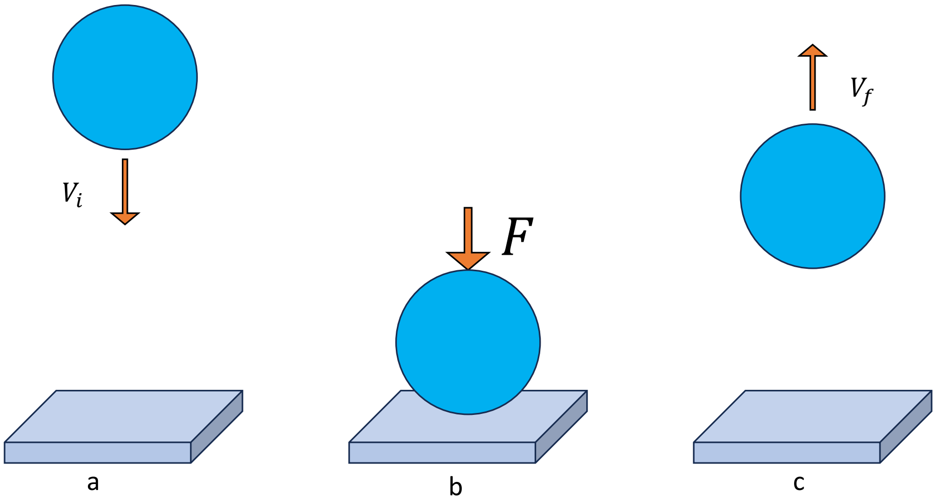

Figure 1.11. Simple example of an impact with a ball dropping on the ground. a) Ball dropping with velocity Vi before impact b) Force F during the impact c) ball bouncing back with Vf velocity after the impact

Consider a ball drop on the ground under gravity with initial velocity V_i just before the impact and bounce back with velocity V_f after the impact as shown in Figure 1.11.The impulse is a crucial parameter in impact mitigation, signifies the total momentum transferred during a collision,

$$impulse = \Delta\vec{p} = m\vec{v}_f - m\vec{v}_i \tag{1.17}$$

By applying Newton's second law F=ma to the impact we can define impulse another way as,

$$\begin{aligned}\vec{F} &= m\vec{a}\\ &= m\frac{\Delta\vec{v}}{\Delta t}\\ &= m\frac{\vec{v}_f - \vec{v}_i}{\Delta t}\end{aligned}$$

$$impulse = \vec{F}\Delta t \tag{1.18}$$

As highlighted in Figure 1.12, real-world impacts frequently take the form of force-time (F vs t) curves that resemble delta functions or Gaussians. These functions mathematically represent forces acting for an infinitesimal or a very short duration. It's calculated as the integral of the force (F) with respect to time (t),

$$Impulse = \int \vec{F} dt$$

In simpler terms, the impulse represents the area under the F vs t curve. While the concept of impulse is essential, it's crucial to acknowledge that peak force also plays a vital role in determining the severity of an impact. As illustrated in Figure 1.12, identical total impulses can manifest in distinct force-time (F vs t) curves. Even though impacts with short durations (delta function-like) may have the same impulse as those with longer durations (Gaussian-like), the high peak force associated with the delta function can cause more significant damage. This observation holds significant implications for impact mitigation strategies.

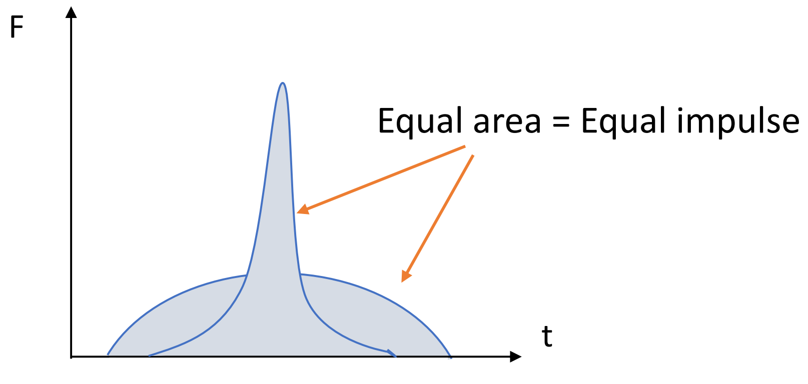

Figure 1.12. Force vs time curve for equal impulses having different curve shapes

Another useful measurement which is the coefficient of restitution of an impact is given by,

$$COR = \frac{\vec{v}_f}{\vec{v}_i} \tag{1.19}$$

1.3. Experimental Methods

1.3.1. Thin Film Preparation Methods

There are several methods to fabricate thin films. Among those, the spin-coating method and drop-casting method are used to create films used in this study. Thicker films can be produced using the drop-casting technique while the thinner ones are made using the spin-coating method.

1.3.1.1. Drop Casting

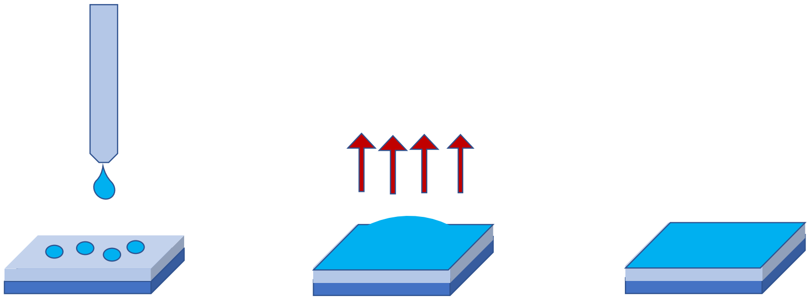

Figure 1.13. Drop Casting Method

In the drop-casting method, the polymer solution was added to a container dropwise until it uniformly spread through the bottom of the whole container to the desired amount of thickness. If the solution is not uniformly spread, holding the container at some angle will allow gravity to spread the solution uniformly throughout the container. The solution is then placed on a flat and leveled surface to achieve further uniform spreading.

1.3.1.2. Spin Coating

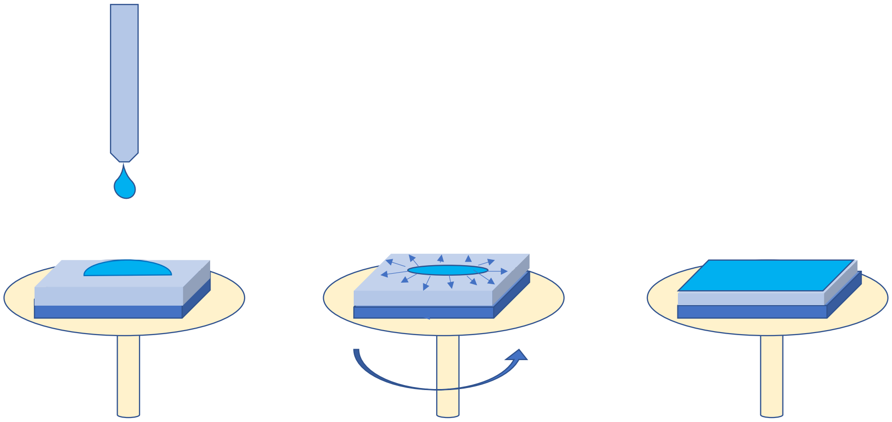

Figure 1.14. Spin Coating Method

As a first step, a clean substrate is placed in the middle of the spin coater. Then the substrate is secured to the spin coater by turning on the vacuum button. Some amount of solution is released on the middle of the substrate by pipet and then the spin coater is turned to the desired speed (these steps might vary with the polymer we are using). After allowing it to further spin for up to 60 seconds a very thin layer of polymer on top of the substrate is created.

1.3.1.3. Annealing

The process of annealing is done by increasing the temperature of the polymer above its glass transition temperature. Some physical and mechanical properties such as thickness, ductility, and plasticity will change during this annealing process (70) (71). The heat treatment supplies energy to the polymer chains allowing them to relax and reorganize their structure to an equilibrium state with lower free energy (72).

1.3.2. Fabricaing PDMS

PDMS elastomer is created from a Sylgard 184 kit by adding the pre-polymer base with the cross-linking curing agent in a 10:1 weight ratio (determined with an electronic balance). The solution is mixed thoroughly for about 10 minutes using a glass stirring rod. De-gassing inside the vacuum oven several times will remove air bubbles trapped inside the mixture. After degassing, the mixture will be ready to either spin coat or drop cast.

Thick PDMS is made using the drop-casting method. In this method, a prepared PDMS mixture will be added to a clean container and further de-gassing is done after adding the mixture to the container. Then the sample will be annealed inside the vacuum oven for 1 hour and 30 minutes at the desired curing temperature.

Thin PDMS films were made using the spin coating method. As the first step, a glass slide is placed on a spin coater and it is cleaned using distilled water to remove any possible dust particles from it. Then a thin layer of water-soluble 1:1 polyacrylic acid/ distilled water solution is added to the glass plate before adding the polymer. The PAA/Water layer is a helpful release layer that enables removing the sticky thin film from the glass plate after curing. PDMS solution is spread on top of the PAA-coated glass plate using a pipet and a fully coated PDMS glass plate should be placed inside the oven for 1 hour and 30 minutes at the desired curing temperature 85 degrees Celsius.

1.3.3. Fabricating PC

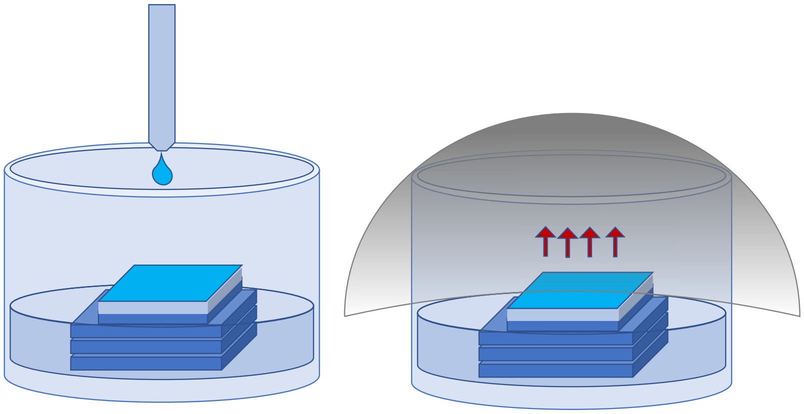

Figure 1.15. PC making process

PC solution was created by adding polycarbonate polymer with the solvent Methylene Chloride in a desired weight ratio using an electronic scale. The solution was kept at room temperature for two to three days to ensure the polymer was completely dissolved in the solvent. A freshly cleaved mica sheet is placed on a clean glass slide with the help of the capillary forces generated by a water droplet. The mica will be used to fabricate spin-coated or drop-cast PC films. Freshly cleaved mica is much cleaner than mica that has been exposed to air or other contaminants. This makes it ideal for use as a substrate for thin film deposition. Also, the fresh mica is chemically inert, meaning that it will not react with the thin film being deposited. This is important for ensuring that the thin film has the desired bulk properties.

Thick PC films are made using the drop-casting method. In this method, solution droplets were added to the top of the mica sheet using a glass pipet until completely spread. Then the mica-glass slide will be placed inside the chamber with a methylene chloride reservoir to slow down the evaporation process. Then the chamber is left for a few days until complete evaporation of the solution. The glass/mica slide is then annealed at 180°C degrees Celsius temperature for 2 hours. Further annealing may be needed if the substrate does not look clear.

Thinner PC films are made by using the spin coating method. A Glass/Mica slide will be placed on the spin-coater and the methylene chloride and PC solution is added using a glass pipet while the substrate spinning. Then the substrate is annealed at 180°C degrees Celsius for two hours.

1.3.4. Seperating Thin Films From Substrate

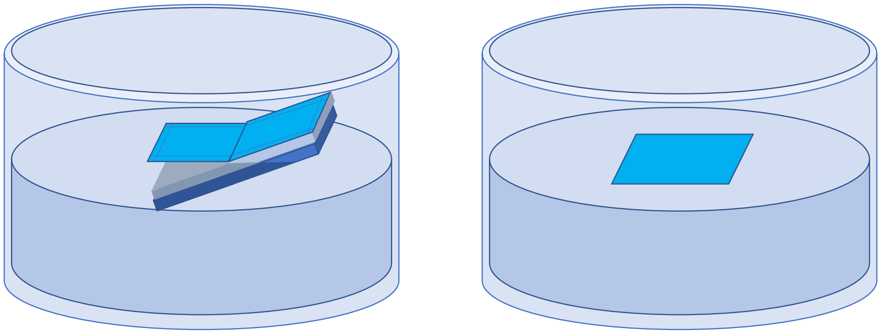

Figure 1.16. Floating thin films in water to release polyacrylic acid layer and separate the film with the help of surface tension of the water

After annealing a sample is cut into approximately 2 to 4-inch square-shaped pieces. For the PDMS samples, the glass slide is dipped inside a water bath so that the film peels off from the glass substrate onto the water surface. Extra care is needed when handling thin PDMS films. Gentle pulling underneath the film using the tip of a tweezer with the help of the surface tension of the water will slowly peel off the film from the glass slide. A similar procedure is used to peel the PC film from the mica surface. There is no extra effort needed for the PC because it will easily float off the mica soon after dipping begins.

After the film is fully separated from the glass or mica, the flat sheet is gently removed from the water surface by floating onto a submerged Kim wipe which is then gently pulled out of the water. Films are allowed to completely dry on Kim wipes for a few days before experiments are performed with them. The remaining pieces on the glass or mica can be used to take thickness measurements of the films using a confocal microscope.

1.4. Instruments, Tools and Software

1.4.1. Confocal Microscope

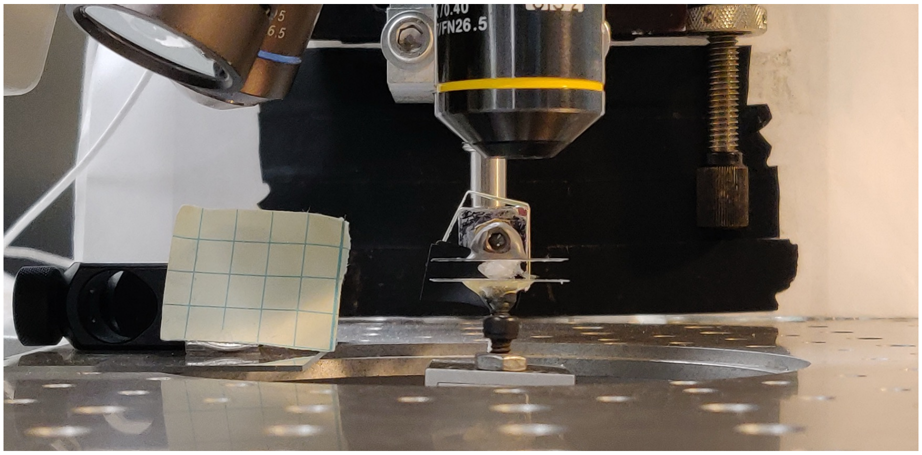

Figure 1.17. Confocal microscope set-up for crumple experiments

The Olympus FLUOVIEW FV1000 is the confocal laser scanning microscope used to take several types of measurements for the experiments described in upcoming chapters such as measuring thin film thicknesses and and performing 3D imaging in this thesis.

1.4.1.1. Measuring Film Thickness

To measure the thickness of the thin films having a few micron thicknesses, first the film adhered to a glass slide and placed under the confocal microscope with a 10x magnification lens. Then by carefully positioning the sample as in 1.17, the confocal microscope was focused on an edge of the sample where film and the glass slide were clearly in focus during the same scan as shown in 1.18 c and d. Then by 3D scanning settings with a start point a little above the top of the film and then an end point a little below the highest intensity observed on the glass surface, and by setting a step-size a 3D scan of the image was taken. To take thickness, positions 1 and 2 were chosen close to each other, one on the film side and 2 located on the glass side as shown in Figure 1.18 c and d. Thickness can be calculated by taking the differences of the highest intensity peaks. For Figure 1.18 c and d, $t_c = 10039.99 \mu m$ and $t_d = 10047.99 \mu m$. Then by subtracting the thickness is $8 \mu m$. For more accurate thickness measurements, it is recommended to average a few such thickness measurements taken around the different positions of the sample.

For samples with known refractive index and also when it is difficult to position an edge, there is another technique to measure thickness. We scanned the sample (shown in the figure 1.19) only through one position to its full thickness, extending a small amount into the glass slide. As a result, there was a noticeable intensity pattern in the reflected light, with a prominent peak matching the sample's top surface (Figure1.19 c) and a smaller, less noticeable peak (Figure1.19 d)matching the glass slide's top surface. For Figure 1.19 c and d, $t_c = 10040.49 \mu m$ and $t_d = 10088.99 \mu m$. Then by subtracting the calculated thickness is $t_{cal} = 485 \mu m$. To get the actual thickness(t) of the sample, this value t_{cal} should be multiplied by the refractive index(n) of the material.

$$t = t_{cal} \times n \tag{1.20}$$

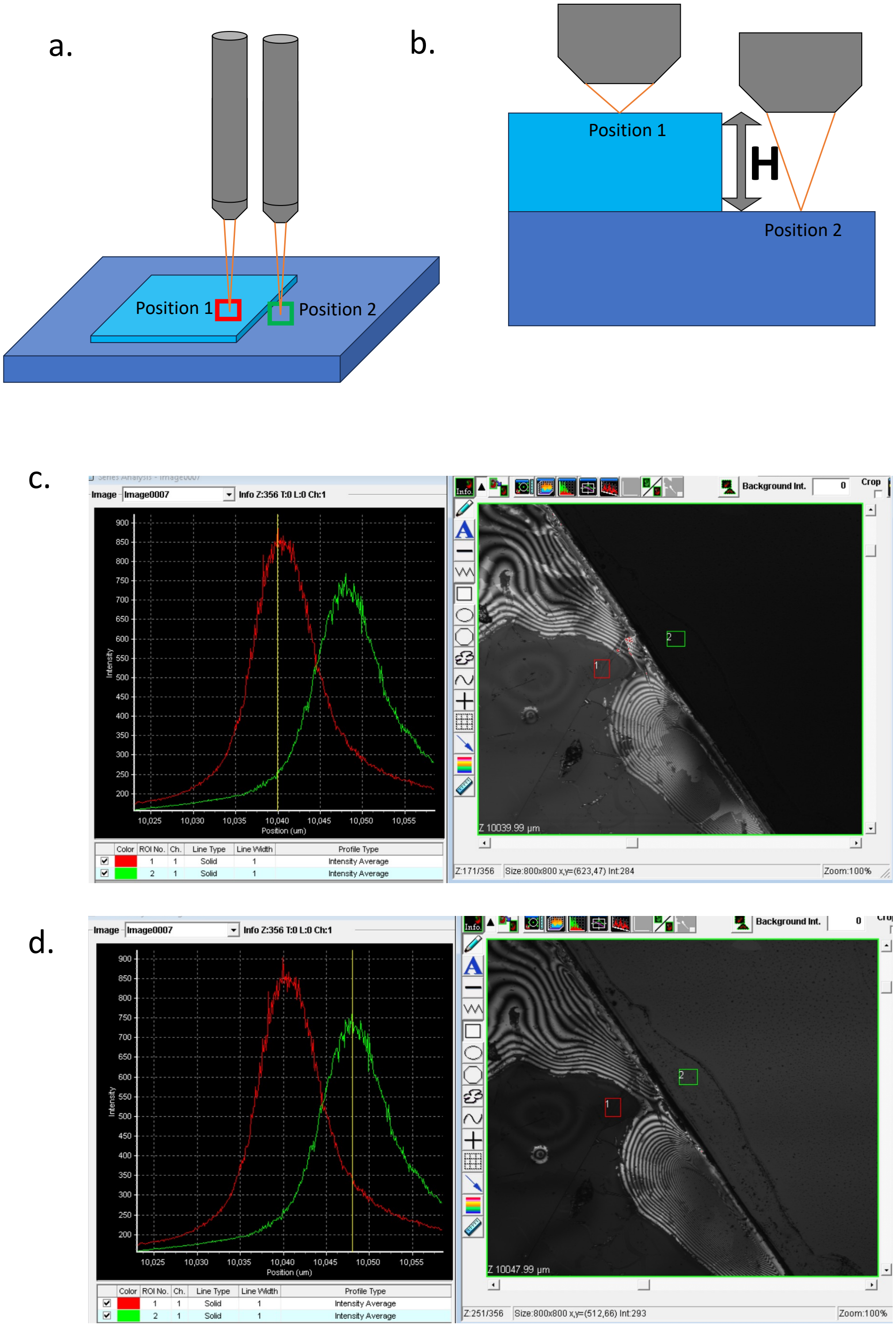

	Color	ROI No.	Ch.	Line Type	Line Width	Profile Type
☑	🟥	1	1	Solid	1	Intensity Average
☑	🟩	2	1	Solid	1	Intensity Average

Z:171/356 Size:800x800 x,y=(623,47) Int:284 Zoom:100%

	Color	ROI No.	Ch.	Line Type	Line Width	Profile Type
☑	🟥	1	1	Solid	1	Intensity Average
☑	🟩	2	1	Solid	1	Intensity Average

Z:251/356 Size:800x800 x,y=(512,66) Int:293 Zoom:100%

Figure 1.18. Thickness measurements from the confocal microscope of a thin polycarbonate film($8\mu m$) :a. Side view of the set-up focused on position 1 2st and then focused on position 2 b. Cross section view of the thin film while thickness measurements. c. Intensity curve and microscope image of position 1 d.Intensity curve and microscope image of position 2.

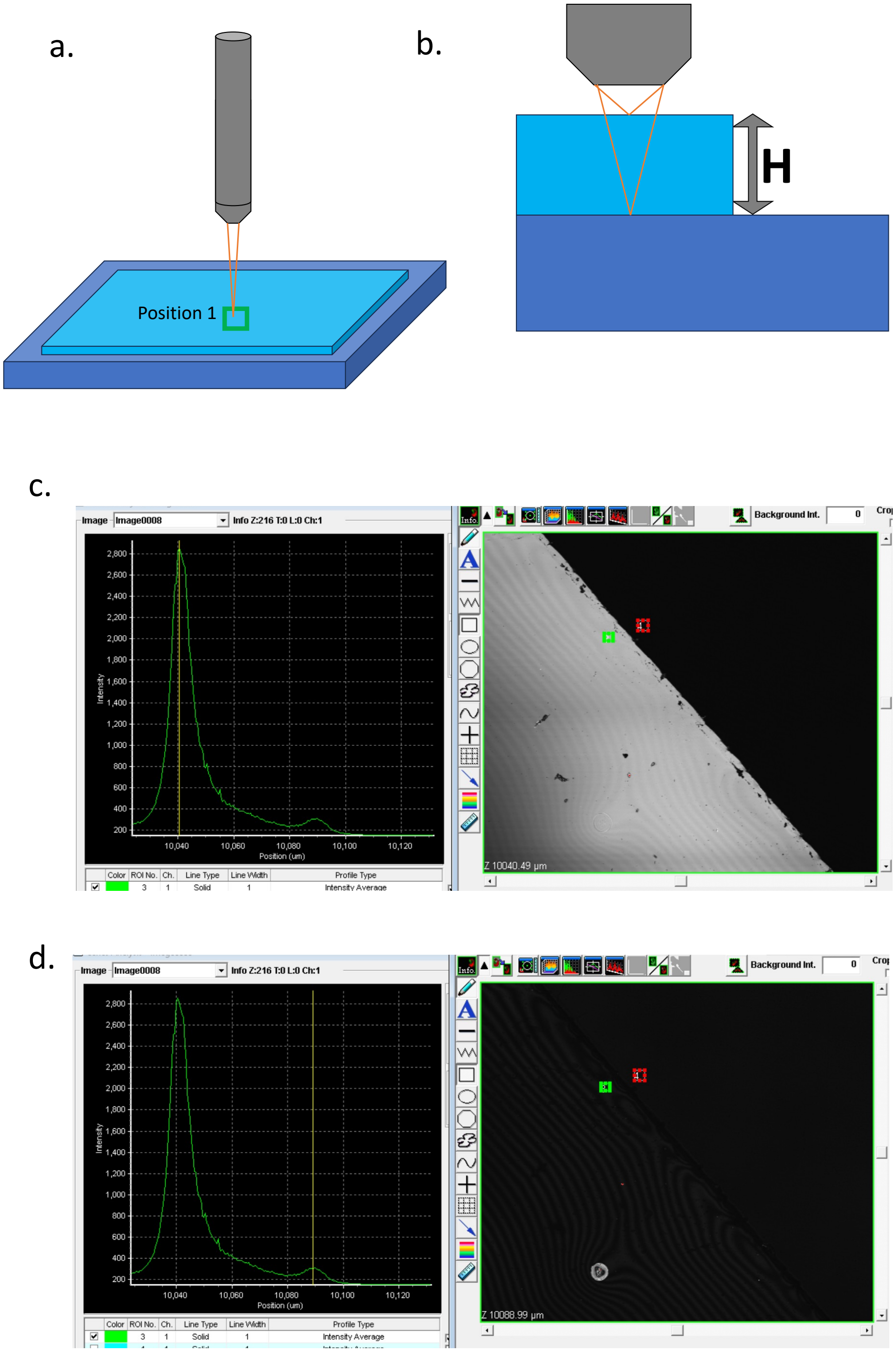

☐	Color	ROI No.	Ch.	Line Type	Line Width	Profile Type
☑	🟩	3	1	Solid	1	Intensity Average

Figure 1.19. Thickness measurements from the confocal microscope of a thin polydimethylsiloxane film : a. Side view of the set-up focused on a position b. Cross section view of the thin film while thickness measurements. c. Intensity curve and microscope image of the position for peak 1 d.Intensity curve and microscope image of the position for peak 2.

1.4.1.2. 3D Imaging Crumples Inside the Fluid

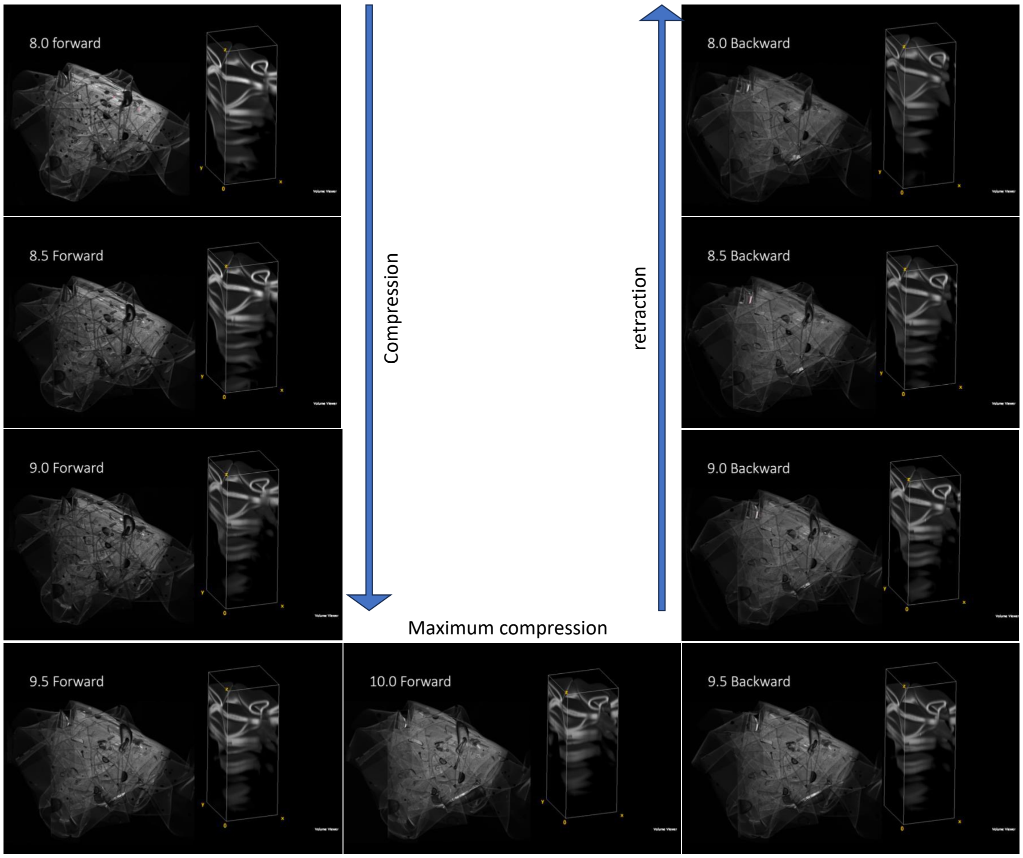

Figure 1.20. 1.25x (left) and 10x(right) imaging of a crumple in glycerin/water solution while quasi static compression and retraction.

When taking 3D images with the confocal microscope, the first step is to crumple a film while it is submerged in glycerin/water solution using tweezers. Creating air bubbles must be avoided as much as possible. We use glycerin/water solution as a mounting medium for the microscope because the refractive index of the glycerin solution is close to the refractive index of PDMS. Hence we can obtain un-distorted images as the microscope focus moves through the volume of the sample.

The glass plates connected to the force sensor and the motor are moved close to each other and a glycerin droplet that is large enough to hold the crumple is placed between the two plates. Then the crumple is carefully loaded inside the droplet and images are taken. It is important to avoid air bubbles inside the droplet because air bubbles can retract the laser beam distorting the image. The confocal image in Figure 1.6 b shows an image taken from a 1.25x lens that often can capture less than half of the full crumple. The final image is created by merging two such images.

A confocal microscope with a 10x objective is used to take images inside the crumple for many layers along its depth in Figure 1.20. For one compression plate separation distance, there are often 100 such slices of images that are used to create a 3D image.

1.4.2. Force Measurements

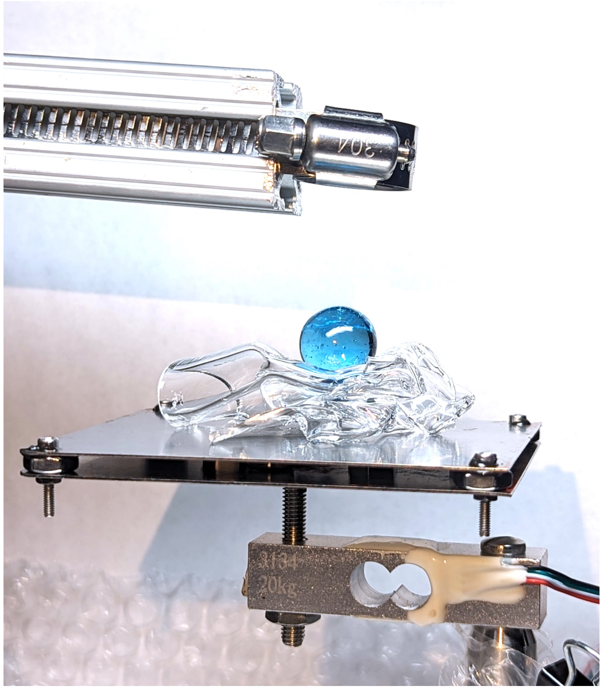

Figure 1.21. Ball drop experiment set-up with strain gauge force sensor connected

Force measurements for each project and each set-up were a little different from each other. For some set-ups, we took force data from built-in sensors of the instruments such as Instron. In crumple experiments discussed in Chapter 1, we use a capacitive force sensor (Micro epsilon DT6110). The bottom glass is connected to the force sensor to measure the forces between two plates and the top glass is connected to a sensitive motor to control distances between plates in this set-up in figure 1.17. For ball drop impact experiments in Figure 1.21, a strain gauge force sensor was used with the INAx126 MicroPower Instrumentation Amplifier circuit given in Figure 1.22. Gain of this instrumentation amplifier can be changed to desired value by changing the R_G resistor value according to the gain equation 1.21 given below,

$$G = 5 + \frac{8k\Omega}{R_G} \tag{1.21}$$

For both of these set-ups, the National Instrument's data acquisition device (NI DAQ) was used to get voltage readings from the sensor with a Matlab program. At the beginning of each experiment, calibration curve generated with a range of some known weights to convert voltage readings to the force measurements.

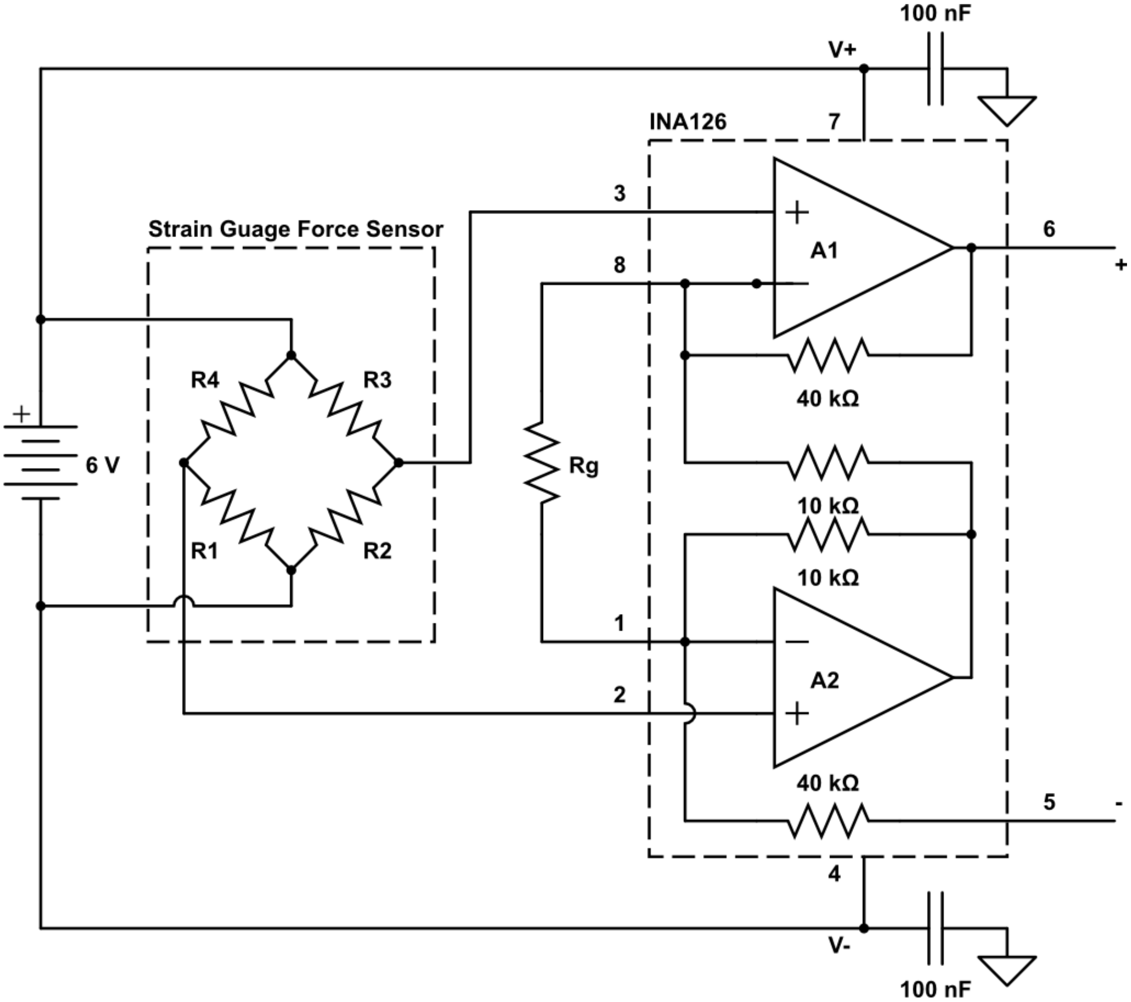

Figure 1.22. Instrumentation Amplifier circuit coupled with strain gauge force sensor to take force measurements for the ball drop experiment set-up

1.4.3. Instron

Instron 3400 universal testing system was used for several types of experiments throughout this thesis. Compression testing for crumpling studies discussed in chapter 1 for some industrially made polycarbonate sheets were done with stainless-steel compression plates attachments. Pull-off tests for the chapter 2 were done with bottom plate attachment and with Instron grips attached directly to the device from the top. Additionally some tensile tests were done to investigate modulus of some materials used in the experiments.

1.4.4. Cricut Cutter

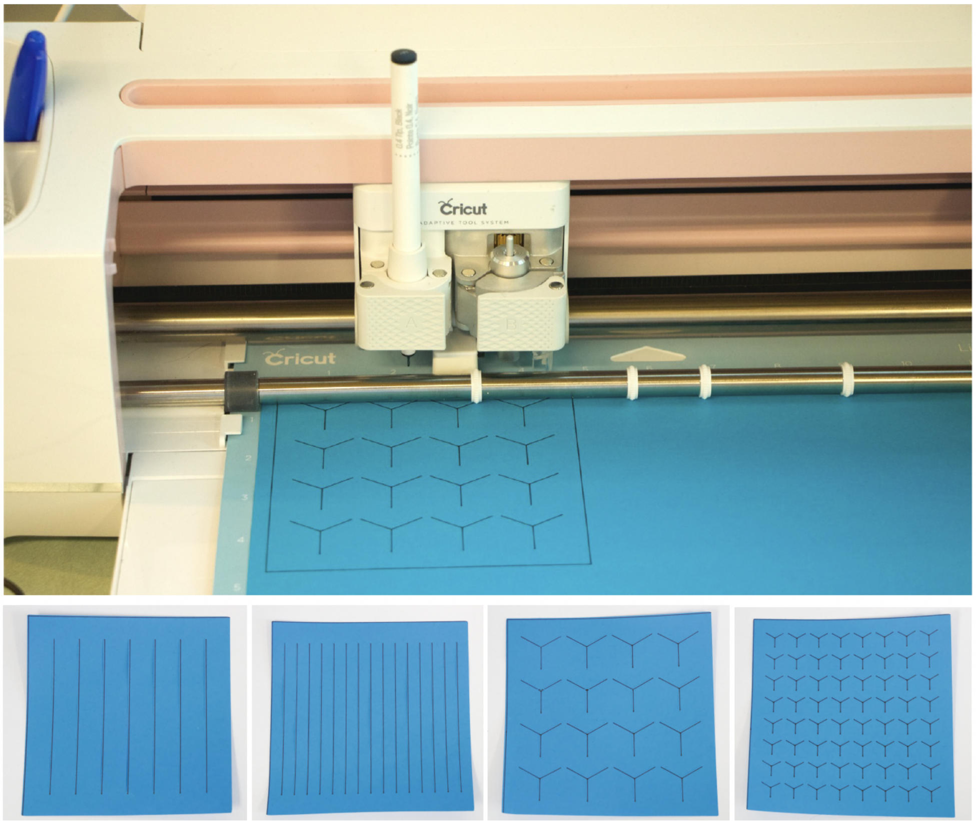

Figure 1.23. Cricut cutter and some cut patterns created for Crumple Kirigami experiments

A Cricut cutter is a smart cutting machine and Cricut maker was used to cut various patterns throughout this work (73). It is easy to operate compared to other industrial laser-based cutting machines. Because of this ease of use, scientist and engineers often use Cricut cutters to achieve simple cutting tasks such as patterned Kirigami. (74; 75) Cricut cutters are available in a variety of models, each with its own set of features and capabilities and the Cricut Maker is the one used in this work and it was used to cut Kirigami patterns for the crumple Kirigami project discussed in chapter two and the origami patterns for the switchable adhesive devises discussed in chapter 3.

1.4.5. CAD

The two computer-aided design (CAD) software SketchUp and Blender are used to create 3D models in this work. SketchUp is a commercial CAD software program that is developed by Trimble Inc and Blender is a free and open-source CAD software program that is developed by the Blender Foundation. Sketch-up was used to create most of the 3D designs used in chapter 3- switchable origami device and most of the other designs were made in the blender.

1.4.6. 3D Printing

Figure 1.24. 3D printing and post-manufacturing process with formlabs 3D printer

Formlabs stereolithography (SLA) 3D printer that uses a laser to cure a liquid resin into a solid object was used to print 3D parts used in this thesis. We used Formlabs' resin 3D printer for this project because of its high resolution, accuracy, and reliability. The first step is to upload the CAD designs to the 3D printer with the desired resolution settings. These 3D-printed parts adhere to the printer base with some additional supporting structures. 3D printed parts were submerged and shaken in propanol solution to remove those additional structures from the original design.

1.4.7. Image Analysis

ImageJ is a Java-powered image processing software crafted under the collaborative efforts of the National Institutes of Health (NIH) and the Laboratory for Optical and Computational Instrumentation (LOCI) at the University of Wisconsin-Madison(76). It is a public domain software that is freely available for download and use(77). ImageJ is a powerful tool that can be used for a wide range of image processing tasks including image acquisition, image processing, image analysis, and image visualization. In this work Imagej was used to measure the radius of crumples, and thickness of some thicker PDMS discussed in chapters 1 and 3 and create 3D visualization of the crumple layers discussed in section 1.4.1.2

1.4.8. FASTEC Fast Camera Video Analysis

FASTEC IL5 high-speed camera coupled with Nova-Pro 300 LED stroboscope was used to record videos for the ball drop impact experiments discussed in chapter 3 of this thesis. Tracker video analysis and modeling tool(version 6.1.6) was used to analyze each video to get the velocity by tracking the moving impactor(1.21).

1.5. Overview

This research explores the mechanics of thin film structures, specifically focusing on crumpled Kirigami(discussed in chapter1), adhesive origami(discussed in chapter2), and the impact mitigation of adhesive crumples(discussed in chapter). By investigating the influence of kirigami cuts and the role of long-range structural features in crumpled sheets, this research aims to contribute to a deeper understanding of crumple mechanics and their potential applications. Additionally, the development of switchable adhesive origami devices and the exploration of crumpled structures for impact mitigation showcase the versatility of thin film mechanics in designing functional materials.

2. CRUMPLED KIRIGAMI *

2.1. Abstract

When a thin sheet is confined to a volume much smaller than its length (or width), it forms a complex state of sharp bends, point-like developable cones (d-cones) and extended ridges known as crumpled matter. One interesting feature of this state, is its high resistance to compression given its light weight. While the origins of this strength still remain a matter of debate, much has been learned through simple experiments and models. Very little work has explored how crumpling is affected by the sheet's topology, which is curious given the close relation between geometry and mechanics. In this work, we couple confocal microscopy with simple force experiments and coarse-grained molecular dynamics (CG-MD) simulations to explore how adding cuts to a sheet alters its behavior in the crumpled state. We find that cutting does not significantly alter the overall compressive behaviour: force scales as a power law irrespective of cuts and magnitudes are only slightly reduced by cutting. Remarkably, when examining regions of high curvature in the crumpled sheets we see evidence of significant changes in the distribution of curvature in cut sheets.

2.2. Introduction

When a nearly two-dimensional (2D) sheet of paper is crushed into a tight ball, it is said to be crumpled. Crumpled materials can be found many places in our day-to-day life serving biological or engineered purposes. Examples include viral capsids (78) (79), delicate pieces of flower petals packed inside a flower bud (80), brain cortex (81) and even on large scales such as

---

* The material in this chapter was co-authored by Wathsala M.A. Jayawardana, Yangchao Liao, Zhaofan Li, Wenjie Xia and Andrew B. Croll. W.J. conceptualized the study, lead the experimental data collection, analysed data and wrote the original draft. Y.L. conceptualized, acquired, and analysed computational data, contributed to the writing the manuscript, reviewed, and edited the manuscript. Z.L. contributed to the computational data acquisition. W.X. conceptualized the study, led the computational effort, supervised Y.L. and Z.L., acquired funding, and reviewed and edited the manuscript. A.B.C. conceptualized the study, led the experimental team, supervised W.J., contributed to data acquisition and analysis, acquired funding, and reviewed and edited the manuscript.This paper is published as a peer-reviewed article and reproduced from Ref.(74) with permission from the Royal Society of Chemistry.

Geological formations(82). Paper crumples are commonly used as protective layers for fragile objects, in part because paper typically comes in sheets and can be more environment friendly than specially engineered polymer foams (83) or bubble wraps (84) which are typically made of non-biodegradable materials. In general, crumpled matter is useful because it has properties such as a high strength to density ratio (the volume of a hand crushed paper crumple can be more than 75% air (19)), high deformability, high energy absorption, and ultimately crumples are very easily fabricated. Scientists and engineers have studied crumpled matter in earnest because of the complexity of these structures and because of their curiosity as to how the useful macroscopic properties arise.

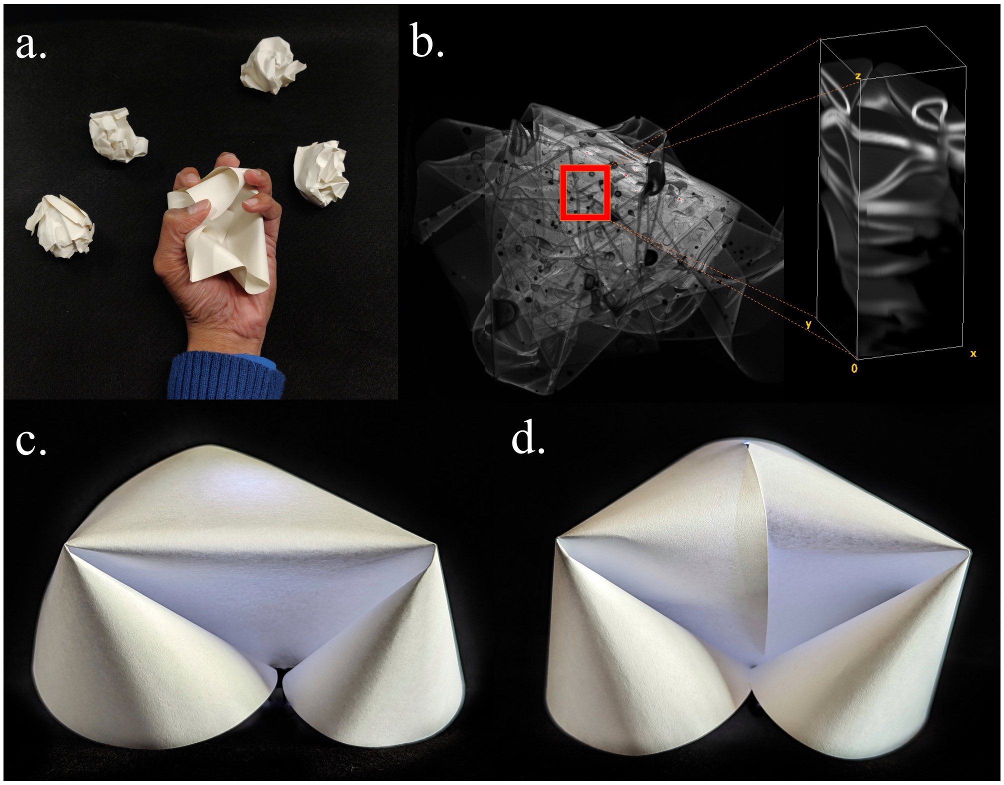

Figure 2.1. Schematic overview of experimental concept. a. The hand crumple. b.2D and 3D Confocal images of a PDMS crumple. c. Top view of a ridge (**Ridge** a bend in-between two d-cones that requires in-plane stretching). d. Top view of a ridge when there is a cut in the middle which releases the stretching stored in the ridge creating two isolated d-cones. (Photographs of c and d taken with extra back light to see the structure properly)

Understanding the cause of the crumple's rigidity has often focused on identifying the basic structural features that occur in a crumpled ball (Fig. 2.1). Studies have thus far identified four structural "building blocks" - bends, folds, ridges, and point-like peaks developable cones (d-cones) that might be important in the overall structure (19; 20; 25). A bend is weakly defined as a region of sheet where the radius of curvature is smaller than other adjacent regions of sheet. A sharper bend, typically where plastic damage has occurred is termed a fold. If present, the plasticity will lead to memory formation in the sheet, which is often a focus of analytic models of crumpling.(6; 85; 86) A point-like peak is called a developable cone or d-cone (Fig. 2.1c and d). More accurately, a d-cone is a conical dislocation in the structure due to focused, localized stretching at the peak of the cone only (the sheet is unstretched elsewhere in the cone). A ridge is a smooth structure which requires in-plane stretching and joins two d-cones (Fig. 2.1c.). Research has still not definitively identified which structural feature dominates the rigidity of the crumple.

In this work, we focus on modifying the sheet topology in order to limit long-range structure formation. The work is motivated by two observations. First, if a ridge forms during confinement, large energies are required due to the in-plane stretching.(19) However, if the sheet between the two d-cones is cut, stretching is no longer necessary or possible (Fig. 2.1c. and d.). Secondly, the observation that few d-cones form near the edges of unaltered crumpled sheets suggests that energy is reduced during compression if d-cones are able to form 'virtually' (that is such that their cores are off the sheet).(87) Therefore, we aim to directly test how vastly increased sheet edge boundaries influence the compressive strength of crumpled matter.

Origami ('ori', fold; 'kami', paper), the paper-folding art form in which a flat sheet of paper is folded into a desired structure, has inspired the design of many useful light-weight structures.(15; 88–90) Such ordered structures differ from random crumples in many ways but are also created from the same four basic building blocks described above. Typically, origami structures are dominated by folds and d-cones, though occasionally they include less focused bending. Researchers have also noted that adding cuts to a sheet, Kirigami ('kiri', cut; 'kami', paper), facilitates a much wider design space. Kirigami can be designed to allow parts of a sheet to rotate, either within the plane of the sheet, or out of the plane of the sheet, creating auxetic or other uncommon global deformation modes.(91) In short, cuts allow new mechanisms of motion and energy storage that typically don't occur in an uncut cut sheet. There has been little exploration of how confinement would affect the unusual deformation mechanisms available in kirigami systems.

Previous crumpling studies have attempted to identify how folds, ridges, and bends affect the rigidity of a crumple. Matan and coworkers created a scaling model based on the assumed dominance of ridges.(19) The model predicted that forces would rise as $F(H) \sim F_0 H^{-\alpha}$, where H is the degree of compression, F_0 is the power-law amplitude, and α is a power-law exponent predicted to be a universal value of 8/3. Early simulations showed some agreement. Vliegenthart and Gompper, for example, found a near 8/3 exponent in simulations of a phantom sheet, but found a larger exponent of approximately 4 for more realistic self-avoiding sheets.(92; 93)

Deboeuf and coworkers developed another theory based on the number of folds in a crumple (25). The model begins with the notion that sheet folding requires a force proportional to modulus and sheet thickness squared. Additionally, they also show how a power law might emerge for a crumpled sheet but note that the exponent would depend on how the sheet is successively folded. They predicted a range of power law exponents is possible (1 to 4).

We have developed a similar model, but assume a more empirical starting point. By exploring the details of the amplitude of the power law, in addition to its exponent, we arrived at the conclusion that bending is the key generator of force (as in Deboeuf), but that long range assemblies of curvature (folds) are not important. Our conceptual point of view is that d-cones (specifically their cores) form the key high energy structure. Extended folds, from this point of view, are simply loci of d-cone cores. Thus, the total length of folds is simply a proxy for how many d-cones were formed during the time the sheet is being confined. A fold's direction or path (or fragmention) is not important to the overall energy.(20). As we don't yet have proof of these features, we consider this model empirical. From this point of view a scaling argument can be made. The force to bend a region of sheet to a curvature of order $1/t$, where t is the sheet thickness, scales as $F \sim Et^2$. The compressing plates only matter when $H < 2R$ where R is the radius of the crumpled sheet so confinement can only add via a unitless factor of $2R/H$. The total structure must then support a load given by,

$$F = Et^2 \left(\frac{2Ro}{H} \right)^{\alpha}, \tag{2.1}$$

where E is the Young's modulus and we assume the power α is related to material properties and the network of high curvature features in the sheet. However, there remains no direct evidence that any one substructure is dominant in crumpling so it is important to narrow down possible causes in order to develop a deeper fundamental understanding of important emergent properties of crumpled matter.

Material properties are also known to affect the rigidity of a crumple. (94) A fold made in plastic material will create memory as curvatures reach high values and plastically deform the sheets. In fact, many schemes exist to analyse these sharp fold patterns after a crumpled sheet is opened.(6; 85; 86) On the other hand, low adhesion elastic sheets retain no memory of high curvatures but still show similar compression behaviour when crumpled. Ensembles of measurements show not only different values for the average exponents but different distributions of exponents for the different materials, which differ again when surface adhesion is changed.(20; 94; 95) It is therefore important to take those material properties into account when examining the effect of structural features inside a crumple.

Remarkably, there have been few attempts to explore how the topology of the sheet affects the crumpling process. In an attempt to create a porous crumpled material, Mirizelli and coworkers explored the mechanical behavior of crumpled sheets with hole patterns cut in them.(96) They found a tiny increase in the exponent of a power-law describing the force as a function of displacement as the crumple was crushed by a mesh approximating a three-dimensional (3D) compression, and some evidence for alignment of folds with the holes.

Additionally, the previous studies explored the crumpling behavior of damaged and defective sheets through molecular dynamics (MD) simulations. It was found that the conformation of graphene sheets at equilibrium was significantly affected by the introduced random vacancies, i.e., the increase in vacancy ratio caused the sheet to transition from a flat conformation to a crumpled morphology and a more amorphous carbon sheet structure (97) (98). Our previous work found that the reconstructed defects caused the graphene sheets to exhibit remarkable wrinkling by distorting and deforming the defect lattice; compared to pristine graphene sheets, reconstructed defect sheets exhibit lower adhesion energy during the crumpling process resulting in hollow spherical crumpled structures, and the crumpled systems have larger bulk modulus and stronger stress heterogeneity levels due to sharper and stiffer crumples (99). These MD simulation-based studies provide insight into the effects of damage and defects on sheet crumpling behaviors at the nanoscale.

In this work we build on this background by creating a set of experiments designed to explore the interplay between the materials and topography of a sheet in the crumpling process. Specifically, we introduce a set of cuts into the sheet aimed at disturbing any long-range features which may be important to the crumpling process, rather than removing area from the sheet. We work experimentally with both elastic and plastic materials, while at the same time using advanced coarse-grained molecular dynamic (CG-MD) simulations to explore observed effects. We note that such topological changes to the sheet have a very minor effect on the overall compressive strength. Remarkably, the cuts do strongly affect the location of high curvature features in the crumple. The two observations indicate that the overall crumple structure is not of primary importance to the compressive behavior.

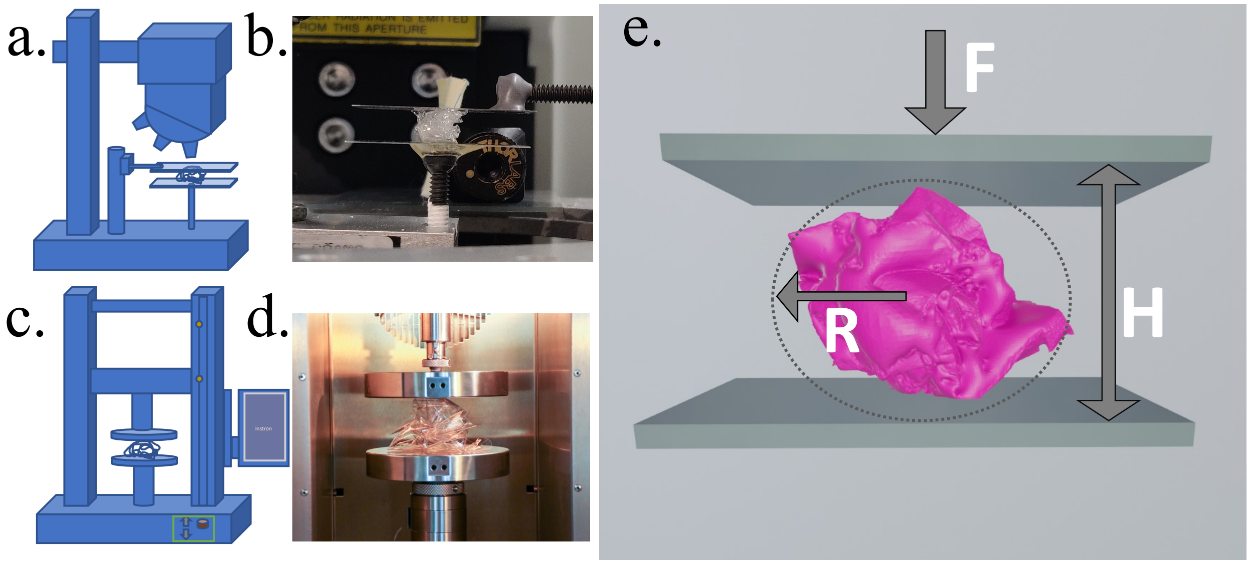

Figure 2.2. Experimental setup. a. Schematic diagram and b. Photograph of a crumple sample placed under confocal microscope. c. Schematic diagram d. Photograph of a crumple sample placed under Instron. e. Schematic diagram of a crumple showing applied force F, plate separation H and the radius R.

2.3.1. Materials

Polydimethylsiloxane (PDMS) is an easily crosslinked polymer with useful features such as hydrophobicity, optical transparency, biocompatibility, adhesion, flexibility, contamination resistance, durability and also a relatively low price. PDMS is often used as a protective layer for electrical insulation, anticorrosion, and antifouling coatings(32). It is widely used in fabricating microfluidic devices (33) (34) (35) (36), microelectromechanical systems(MEMS) (37), as well as soft lithography stamps and molds(38). In this work, we use the Dow-Corning Sylgard 184 system, which we cure at 80 degrees Celsius in a vacuum oven after mixing in a 10 to 1 ratio by weight of prepolymer to crosslinker. We regularly measure the modulus to be 1.69 MPa, which is in line with many other measurements in the literature.(39; 40; 42).

Polycarbonate (PC) is a thermoplastic material which has properties such as optical transparency, low weight, high modulus, and relatively high yield strength. PC can be used in optoelectronic devices as a replacement for inorganic glass substrates in flexible electronic devices.(41) The glass transition temperature, T_g of the PC is 145 °C.(42) Here, we use polycarbonate in chloroform solution to create thin sheets via spin coating, dip coating or drop casting. Additionally, we use some larger polycarbonate sheets purchased and used as received from McMaster-Carr. Cast sheets are cured above the PC T_g at approximately 200 °C. For both lab created and store bought PC we find Young's modulus to be 2.0 - 2.6 GPa. (42–47; 100)

Finally, we also use Quill.com multipurpose printer paper as an alternative high modulus, plastic material. We do so because even though the material is poorly controlled by us, is humidity dependent and is ultimately a tangle of fibers rather than a true continuum sheet, it can be made much more quickly and can increase the statistical power of our measurements. In our case, paper can be cut with a Cricut cutter in a manner of minutes, whereas PDMS and PC may take a day or more to properly cast a sheet. We find the paper to have a tensile modulus of 2×10^7 Pa and a thickness of 0.095 mm.

2.3.2. Sample Preparation

2.3.2.1. PDMS Preparation

PDMS solution is created by adding the Dow Corning Sylgard 184 pre-polymer base to the cross-linking curing agent in a 10:1 weight ratio. The mixture is then mixed thoroughly for about 10 minutes using a glass stirring rod. Degassing takes place inside a vacuum oven where the pressure is decreased and increased several times at room temperature. This removes air bubbles trapped inside the solution. After degassing, the solution is ready to be either spin coated or drop cast. Glass slide coated with a thin polyacrylic acid release layer was used as substrates when casting PDMS sheets. Samples are then placed inside the vacuum oven and annealed for 1 hour and 30 minutes at the curing temperature of 85 °C.

2.3.2.2. PC Preparation

PC solution was created by adding polycarbonate polymer to the solvent Methylene Chloride in a 1 % ratio using an electronic scale. The solution was kept at room temperature for two to three days to ensure the polymer is completely dissolved in the solvent. Freshly cleaved mica sheets are used as substrates for creating PC sheets. Mica is placed on a clean glass slide and held with the help of a water droplet in order to increase rigidity for spin-coating or drop-casting. Thinner PC sheets will be made by using the spin coating method. The glass/mica slide will be placed inside the spin-coater and the methylene chloride and PC solution is added using a glass pipet. The substrate is then annealed at 180 degrees Celsius for several hours.

Additionally, store bought sheets of polycarbonate were used in the large-scale setup. Here, sheets cut from a roll of 128 μm thick PC and were otherwise used as received from McMaster Carr inc. Sheets did not have any residual curvature due to shipping and storage and were found to have a modulus in the same range as that measured with the thinner in-lab cast sheets.

2.3.2.3. Spin Coating

As the first step, a clean substrate that will be covered with a polymer is placed in the middle of the spin coater. Next, the substrate is carefully secured to the spin coater by supplying vacuum to the chuck. Some amount of solution is then released on the middle of the substrate using a pipet. The spin coater is turned on and accelerates to the desired speed (acceleration and angular speed can be adjusted to create different sheet thicknesses). After allowing the coater to operate for a desired time, a very thin layer of polymer is left on top of the substrate.

2.3.2.4. Drop Casting

In the drop-casting method, polymer solution was added to a container drop wise until it uniformly spread over the bottom of the whole container and achieved the desired thickness. If the solution is not uniform, holding the container at some angle will allow the gravity to spread the solution uniformly throughout the container. The solution will be placed on a flat, level surface to achieve further uniform spreading.

2.3.2.5. Sheet Dimensions

The thickness of the sheets are measured using a confocal microscope before crumpling the sheet. The radius of the crumple is typically measured by taking a smartphone picture with a reference scale and using imageJ image processing software. Width and height measurements are also taken by image processing a smartphone image before crumpling. Thicknesses were measured with a confocal microscope, or via smartphone and image analysis software.

2.3.2.6. Minimizing Adhesion

The elastic polymer PDMS involves adhesion that may confound results. Therefore, we remove adhesion by adding a monolayer of corn starch particles to both sides of sheet. There is no appreciable adhesion that needs to be removed from the PC sheets at the thicknesses used in this work.

2.3.2.7. Kirigami Patterns

PDMS sheets were cut by hand with a scalpel blade. In particular, we add a button-hole like cut in the middle of the non-Sticky PDMS square as shown in Fig. 2.4a. This ensures the overall dimensions of the sheet are maintained. Typically, a sheet would first be tested in its native (sticky) state, then carefully uncrumpled. It was then treated to remove adhesion and recrumpled and tested. The process was then repeated while adding one, three or seven cuts before recrumpling. In this way, the exact same sheet can be examined in several different topological states.

On the other hand, plastic sheets were not reused. The paper and polycarbonate sheets could be cut with a cricut cutter controlled by a computer. This allowed more complex patterns to be cut (see Fig. 2.4a.) in addition to the long straight ‘button hole’ cuts. Some sheets were cut by hand to mimic the slight imperfections that would be present in the PDMS sheets. sheets were often photographed after opening.

2.3.3. Mechanical Testing

2.3.3.1. Confocal Microscope

A typical experiment in the confocal setup is shown in Fig. 2.2. The sticky crumple shown in this figure is made out of PDMS with a 10:1 crosslink ratio and the thickness of the crumple is between 50 μm to 100 μm. This simple experiment is designed to find the force response of the polymer crumple when compressed between two plates, while allowing detailed observation via microscopy. In this apparatus the bottom glass plate is connected to the force sensor (Transducer Technologies) and the top glass plate is connected to a sensitive motor (Physik Instrumente N-381.3a). A square shaped sheet is crumpled by hand. There is no exact procedure for crumpling to ensure it is always a random collection of folds and bends. After the crumple arrives at an approximately spherical shape, it is loaded between two parallel plates made of glass. Then the glass plates are moved close to each other until an arbitrary critical force value is reached, while force and distance data is recorded by a transducer and digital camera respectively.

2.3.3.2. Instron

A typical experiment in the Instron universal test machine setup is shown in Fig. 2.2. Here the larger industrially made PC sheet is crumpled and placed between the stainless-steel compression plates of an Instron 3400 universal testing system. The plates were set to move at a velocity of 5 mm/min for all experiments. Once again, force-displacement data is captured by the instrument, and imaging is conducted with a cell-phone camera.

2.4. Overview of Coarse-Grained Modeling

This paper employs CG-MD simulations to investigate the compressive strength of crumpled graphene nanosheets having different cut patterns and to provide an in-depth analysis of the internal structure of the crumpled kirigami sheets. In brief, we obtained square graphene sheet models with 50 nm edge lengths having different cut patterns by removing specific combinations of CG beads on the previously developed graphene CG models (101). That is, for the straight cut pattern (i.e., 7 and 15 straight cuts), all CG beads in a straight line are deleted; for the Y cut pattern (i.e., small and big Y cuts), multiple CG beads that form the Y-shape are deleted. After obtaining stable models that are in equilibrium, we apply a confining sphere that completely encompasses the model to simulate the crumpling behavior of graphene sheets in experiments based on the aerosol evaporation method (102). By decreasing the radius of the confining sphere at a speed of 50 m/s (consistent with previous studies (99) (103) (104), the sheet model is compacted into a crumpled system accordingly and the crumpled system with a cylindrical shape is subsequently obtained by replacing the confining sphere with a confining cylinder. Note that the radius, height, and density of the crumpled cylindrical graphene before the uniaxial compression simulation are 7.1 nm, 14.9 nm, and 0.809 g/cm^3, respectively.

Next, uniaxial compression and unloading are performed by two rigid flat plates with the same material properties as the crumpled graphene sheet. Specifically, both uniaxial compression and unloading in our work are carried out at rates ranging from 40 m/s to 100 m/s, and the height and density of the cylindrical crumpled sheet in the final compressed state are 5 nm and 2.428 g/cm^3, respectively. Moreover, 130 independent simulations of crumpling, uniaxial compression, and unloading were performed for each cut pattern of the crumpled system. A detailed description of the CG graphene model, cut patterns, crumpling and uniaxial compression simulations can be found in ESI†. In our study, all CG-MD simulations are performed with the open-source package Large-scale Atomic/Molecular Massively Parallel Simulator (LAMMPS) (105).

2.5. Results and Discussion

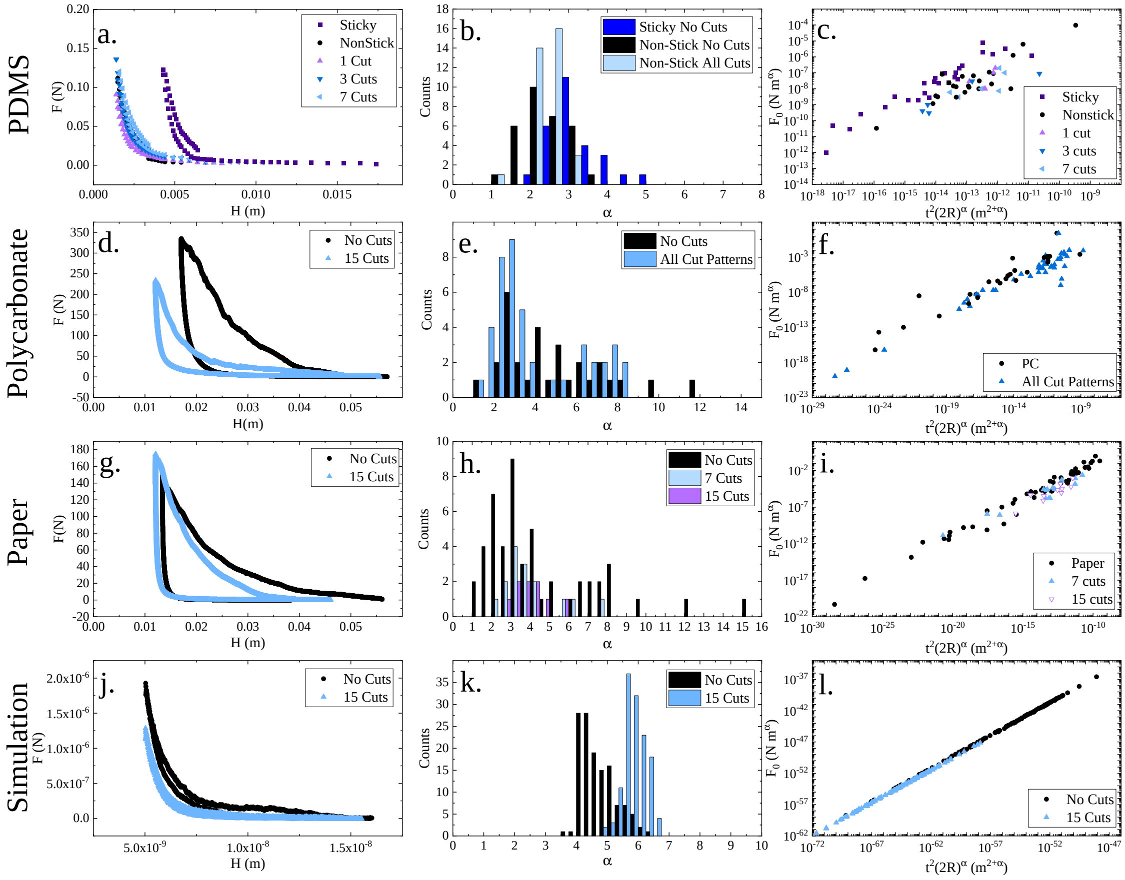

Figure 2.3. Experimental and simulated results. **PDMS Experiments**. a. Representative force displacement curves of crumpled PDMS sheets in several states (sticky, non-sticky, cut non-sticky). b. Histograms of the power law exponent recorded for each class of experiment (again sticky, non-sticky, cut non-sticky). c. Power law amplitude as a function of $t^2(2R)^\alpha$. On this scaling plot, data falls along a linear curve, the height of which represents an effective modulus of the sheet. **PC Experiments**. d. Representative force displacement curves for crumpled PC sheets with no cuts or 15 straight cuts. e. Histograms of the power law exponent recorded for cut and uncut PC sheets. f. Power law amplitude as a function of $t^2(2R)^\alpha$. Cut data might be slightly lower, indicating a reduced effective modulus. **Paper Experiments.** g. Representative force displacement curves for crumpled Paper sheets with no cuts or 15 straight cuts added. h. histograms of the power law exponent recorded for cut and uncut paper sheets. i. Power law amplitude as a function of $t^2(2R)^\alpha$. Cut data is slightly lower, indicating a reduced effective modulus.**CG-MD Graphene Simulations** j. Representative force displacement curves for crumpled graphene sheets with no cuts or 15 straight cuts added. k. Histograms of the power law exponent recorded for cut and uncut crumpled graphene sheets. l. Power law amplitude as a function of $t^2(2R)^\alpha$. Cut data is slightly lower, indicating a reduced effective modulus.

2.5.1. PDMS

Fig. 2.3 shows typical force displacements curves collected during an experiment. In this case a 32 mm by 40 mm sheet of thickness 75 μm was crumpled and tested first in the sticky, as produced state, shown by the black solid circle symbols. The curve is well fit by a power law, as is expected. The sheet was then carefully uncrumpled and treated to remove surface adhesion. The sheet was then recrumpled and retested producing the curve shown by the gray solid square symbols in Fig. 2.3a. Notably, the adhesion free sheet is much more compressible than the sticky sheet, a phenomenon discussed previously in Ref 23.

The uncrumpling/recrumpling process was then repeated with straight cuts added on each subsequent uncrumpling. The data for crumples with 1, 3, and 7 cuts are shown in Fig. 2.3a. We note some small variation in the force curves; however, the variation is not correlated with the number of cuts. The observed differences are typical of repeated crumple measurements even when no topological changes are made to a sheet. Each test involves completely opening and recrumpling the PDMS sheet, so each force curve probes a different crumpled network. In short, the force displacements curves show no sensitivity to the topological changes of the sheet due to the cuts.

To look more carefully at the data, each force-displacement curve was fit with a power law $F = F_0 H^{\alpha}$. Fig. 2.3b shows a histogram of the various α values recorded from the fits. The distribution of the sticky sheet exponents may fall on slightly higher values than does the non-sticky sheets, however, within the statistics we have collected no claim can be made that the distributions are significantly different.

Next, in Fig. 2.3c we plot the fit values for the power law amplitude (F_0) against the expected scaling predicted by Eqn. 2.1, leaving the modulus as a fit parameter. The plot shows the sticky sheet data to lie along a straight line (on a log-log axis) and to have a higher effective modulus (as it is higher along the y axis), than the low adhesion tests. The low adhesion sheets and the cut low adhesion sheets also lie along a straight line, but once again no difference can be reliably observed between the cut and uncut sheets. In summary, the PDMS sheets do not show any statistically significant differences when cuts are added to change the sheet topology.

2.5.2. PC

It is possible that PDMS sheets do not show differences with topological changes because they are elastic and have a relatively low modulus. Polycarbonate, on the other hand, has a much higher modulus and will plastically yield in regions of high stress. It can therefore serve as a good alternative material system to broaden this investigation. Hence, experiments were conducted in a similar manner as was described above with PDMS sheets. Once again, power laws were fit to force-displacement data taken with uncut and cut PC sheets. Note that unlike the PDMS experiments, each PC sheet is used only once due to the memory created by plasticity.

Fig. 2.3d. shows force-displacement curves recorded for a typical uncut and a typical cut PC crumpled sheet. Curves show some small but near instant changes in force, which correspond to stick-slip or buckling events within the crumple. These are not noted in the experiments with very thin sheets, possibly due to their increased adhesion. Regardless, the overall indentation curves are still well fit with a power law, so again an exponent and amplitude could be measured. We also note the much greater hysteresis in the PC sheets, due to the plastic loss occurring during compression. Again, there is very little quantifiable difference between the cut sheets and the uncut sheets.

Histograms of the power law exponents for both cut and uncut polycarbonate sheets are shown in Fig. 2.3e. Both distributions appear to be log-normal (rather than Gaussian as the PDMS sheets), and there again appears to be little difference between the cut and uncut sheets.

Fig. 2.3f. shows the amplitude of the power law fit on the same scaling plot as discussed in Fig. 2.3c. The data for all uncut sheets, straight cut sheets and Y cut sheets appears to fall along straight lines, reinforcing the broad applicability of Eqn 2.1 . Both sets of cut sheets (straight and Y) appear slightly lower on the plot, indicating a possible decrease in effective modulus, but the observation is not outside the scatter in the data and is once again inconclusive.

2.5.3. Paper

In order to more easily increase statistics and add an additional material to this study, experiments were conducted on paper sheets. Sheet size, cut number, and cut pattern were varied. Room relative humidity was typically around 60 % during the experiments. Representative results are shown in Fig. 2.3 taken from experiments following the same protocol as with the other two materials.

Force curves for both pristine sheets and cut sheets show very similar behavior and are well fit by power law curves. Histograms of the power law exponents show a log-normal distribution for both cut and uncut sheets and a slight increase for the peak of the distribution with increasing number of cuts in the sheets (fig. 2.3b). Power law amplitudes also show a slight difference, with the cut sheets being slightly lower in effective modulus than uncut sheets. Average modulus for all three materials calculated by fitting Eqn. 2.1 above are reported in Table 2.1 below for clarity.

Table 2.1. Average plane strain modulus measured via crumpling

	Modulus (Pa)	
Material	Uncut sheets	Cut sheets
PDMS	$1.8 \times 10^5 \pm 3 \times 10^5$	$1.1 \times 10^5 \pm 9 \times 10^4$
PC	$5.7 \times 10^8 \pm 9 \times 10^8$	$6.4 \times 10^7 \pm 9 \times 10^7$
Paper	$2.3 \times 10^9 \pm 3 \times 10^9$	$6.7 \times 10^8 \pm 1 \times 10^9$
Simulations	$1.4 \times 10^{11} \pm 6 \times 10^{10}$	$5.2 \times 10^{10} \pm 3 \times 10^{10}$

2.5.4. Molecular Dynamics Compression Simulation of Coarse-Grained Crumpled Graphene

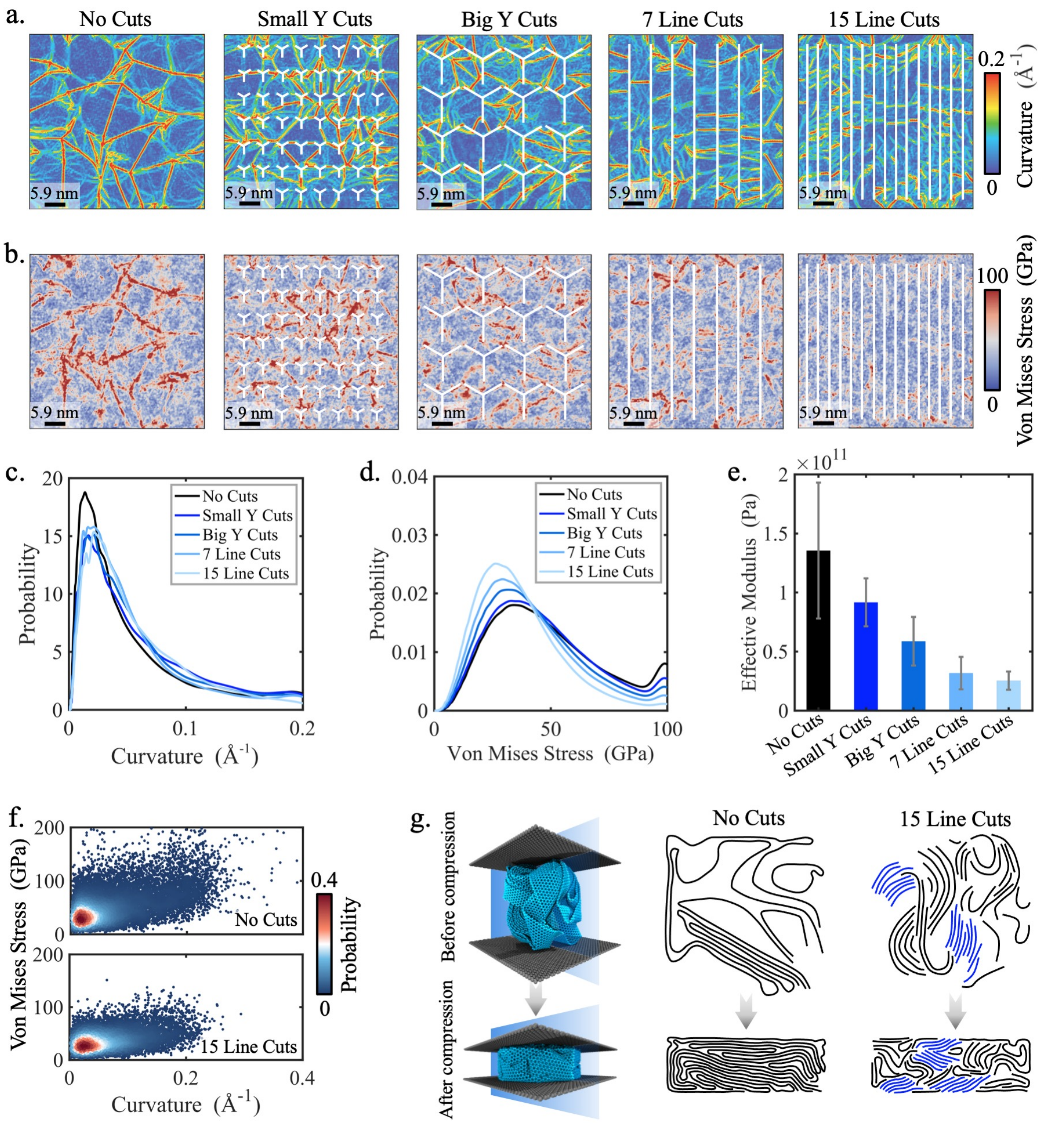

Figure 2.4. Internal structure analyses of crumpled graphene. Local a. curvature and b. von Mises stress distribution maps for crumpled graphene sheets with different cut patterns after uniaxial compression simulation (before unloading). The probability distributions of local c. curvature and d. von Mises stress. e. Effective modulus of crumpled graphene sheets with different cut patterns. f. Distributions of curvature versus von Mises stress crumpled graphene sheets having no cuts and 15 straight cuts, respectively. g. Schematics for analyzing the cross-section patterns of the crumpled model before and after the uniaxial compression simulation, and the corresponding cross-section patterns of the no cuts and 15 straight cuts models. The ordered short-range laminate structure is highlighted in blue in the 15 straight cuts model.

We conducted CG-MD simulations of many different cut patterns (see Fig. S1 in ESI†), but to follow experiments, we only compare and analyze the details of uncut and 15 straight cuts crumpled graphene sheets to explore the effect of topological changes in the sheets on their mechanical properties at the nanoscale. As shown in Fig. 2.3j, the MD simulation validates that the relationship between the compressive force and the plate separation can be well described by Eqn. 2.1 for the crumpled graphene model with two different topologies (i.e., no cuts and 15 straight cuts). In addition, the force-displacement cycle of the uncut sheet shows a slightly larger compliance and hysteresis than that of the 15 straight cuts sheet. We believe that this is because the cut sheet is more mobile during the crumpling process. The cut model forms more short-range laminated bends during crumpling (see Fig. S2a in ESI†), requiring less force during compression.

The histogram of power law exponents in Fig. 2.3k shows that the power law exponents of the 15 straight cuts model increase with respect to the no cuts model and exhibit narrow, possibly log normal distributions. Further, the relationship between F_0 and $t^2(2R)$ indicates that the MD simulation data obey a linear relationship and the fitted line of the 15 straight cuts model lies slightly below the no cuts model, implying that the 15 straight cuts crumpled model has a slightly smaller effective modulus (Fig. 2.3l). Notably, the effects of cuts on the compressive properties of the sheet observed in the simulations are in general consistent with the phenomena observed in the experiments (especially for crumpled PC and paper), suggesting that the influence of cuts on the mechanical properties of the sheet is valid at both the nano- and macro-scale and is again fairly small.

To better understand the effect of topological changes on the internal structure of the crumpled sheet, Fig. 2.4 proceeds to analyze the local curvature, von Mises stress, and typical cross-section patterns of the crumpled graphene sheet after uniaxial compression in simulation. The local von Mises stress (σ_v) is given by $\sigma_v = \sqrt{(3\sigma_{ij}\sigma_{ij} - \sigma_{kk}{}^2)/2}$, where σ_{ij} $(i, j = 1, 2, 3)$ are the components of the Cauchy stress tensor. Note that the von Mises stress considered in this work is normalized with respect to volume of the model and that it is a theoretical value that can be utilized as a yielding criterion (i.e., σ_v is not a real stress); the local curvatures and stresses are mapped to a 2D planar model for better visualization. Figs. 2.4a and 2.4b show the local curvature and stress distribution of the crumpled graphene sheets with different cut patterns (i.e., no cuts, small and big Y cuts, and 7 and 15 straight cuts) after uniaxial compression, respectively. It can be observed that the high curvature regions of all models correspond closely to their high stress regions. High curvature and stress regions of models with cuts exhibit short-range and isolated patterns compared to the long-range and interconnected high curvature and stress regions presented by the no cuts model. This is attributed to the introduction of cuts (especially straight cuts) that make the sheet tend to form laminated bends during the crumpling process, while forming fewer d-cones and ridges, and the cut pattern breaks the internal structure of the crumpled system. Figs. 2.4c and 2.4d present the probability distributions of the local curvatures and stresses of the crumpled model after uniaxial compression, which are observed to be skewed log normal and normal distributions, respectively. In detail, the introduction of the cut causes the peak of the curvature probability distribution to decrease, while the peak of the stress probability distribution increases and shifts to a lower stress, indicating that the cut makes the crumpled system less mechanically heterogeneous, as well as reducing the effective modulus of the system (Fig. 2.4e). Furthermore, the distribution of curvature versus stress (Fig. 2.4f) can be reconfirmed that the stress and curvature of the no cuts model and the cuts model remain highly correlated, i.e., small curvature corresponds to small stress and large curvature corresponds to large stress, only with relatively small curvature and stress of the cuts model.

To provide a better illustration of the influence of cuts on the internal structure of the crumpled system at the nanoscale, Fig. 2.4g shows the cross-section patterns of the no cuts model and the 15 straight cuts model before and after uniaxial compression, repectively, which are obtained by cutting the crumpled system with a cutting plane perpendicular to the compressing plates. It can be found that the no cuts model displays an ordered long-range laminated cross-section pattern both before and after uniaxial compression, while the 15 straight cuts model shows more ordered and short-range laminated cross-sections (highlighted in blue for examples) before and after uniaxial compression. This again indicates that the cuts of the sheet allow the internal structure of the crumpled system to be cut off, which further affects the mechanical properties of the system. In general, the effective modulus decreases sequentially in the order of no cuts, small Y cuts, big Y cuts, 7 straight cuts, and 15 straight cuts (Fig. 2.4e), i.e., from $1.36 \times 10^{11} \pm 0.58 \times 10^{11}$ Pa in the no cuts model to $2.53 \times 10^{10} \pm 0.77 \times 10^{10}$ Pa in the 15 straight cuts model. Although the drop in effective modulus is close to an order of magnitude, it is a relatively small reduction and not as significant as one might expect. As with the experimental findings, the topological change produces a relatively significant effect on the internal structure of the crumpled sheet at the nanoscale, whereas the effect on its compressive strength is relatively small, implying that the ridges and other long-range structures in the crumpled system have a small effect on the overall compressive strength of the system.

2.5.5. Line Detection

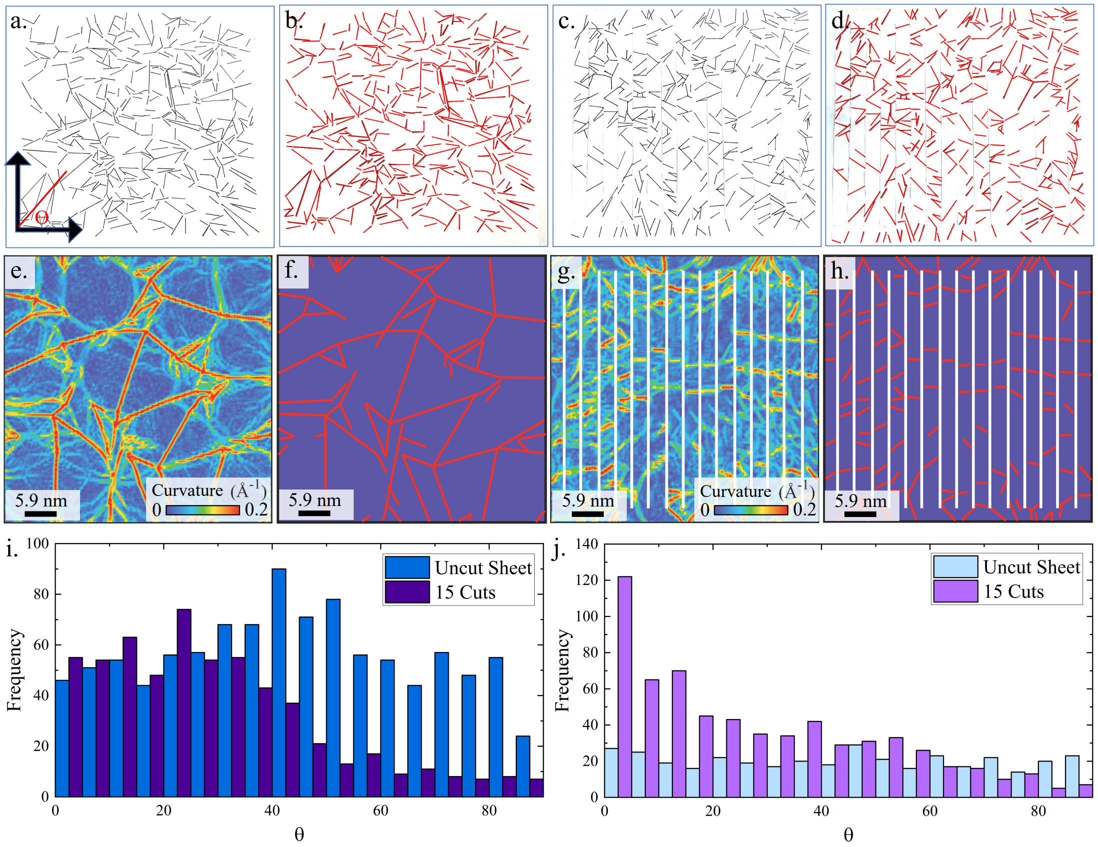

Figure 2.5. Curvature detection in experiments and simulations. a. Photo of a uncut and uncrumpled paper crumple b. Line detected uncut paper crumple c. Photo of 15 cuts uncrumpled paper crumple. d. Line detected 15 cuts paper crumple. Note that at the contrast required for crease detection, the thin cuts are difficult to see in the images. e. Local curvature distribution and f. detected high curvature regions of uncut crumpled graphene simulations. g. Local curvature distribution and h. detected high curvature regions of 15 cuts crumpled graphene simulation. i. Orientation of the ridges in paper crumple. j. Orientation of the ridges in simulated crumpled graphene.Here, both uncut and cut crumpled sheets are obtained from five independent simulations.

In the experimental system, it is difficult to quantify structural features of the crumpled sheets without complex 3D imaging techniques.(20; 106) However, both the PC and the Paper sheets deform plastically during crumpling which means that there is a visible memory of high curvature regions of the internal network of the crumple after a sheet has been carefully uncrumpled. As is common in the literature, we examine this structure via scanning sheets and processing the images (see fig 2.5).(6; 85; 86)

Here we examine paper crumples by first carefully uncrumping a sheet after an experiment and then using a black marker to emphasize all the long-range structures that were visible (i.e. folds in the crumple). Basic line detection of a photo of the flattened crumpled sheet was completed with a code written in python. The line detection method was imperfect, so each data set was additionally screened for any flaws. Any flaws were subsequently corrected by hand using ImageJ software. Ultimately a table of line segments was constructed, where each line represented a crease in the uncrumpled paper sheet.

A similar process could be used to analyze the simulated sheets. In this case regions of high curvature were marked by software during the peak of compression in an experiment. The sheet could the be digitally unfolded into a flat state, and lines could be fit to the high curvature regions by adjusting a curvature threshold. Again, a table of line segments could be prepared and analysed.

The tables of lines could then be studied in several ways. We considered the angle made by a typical fold and the horizontal (Fig. 2.5). Uncut paper sheets have a uniform distribution of angles, which is not surprising; the sheet is homogeneous and there is no strong case for any symmetry breaking. The same result also occurred with the uncut simulated graphene sheets. However, the angular distribution from both cut paper and simulated graphene showed a bias towards folds having an angle of zero. In other words, the high curvature regions preferentially align perpendicularly to the cut edges. The transition angle differed between experiment and simulation, which we believe is related to the plasticity of paper which is not present in the simulations. This is because the elastic simulated sheets are more free to rearrange regions of high curvature as confinement is increased, whereas plasticity will lock in a feature above a threshold curvature in the paper sheets. The mobility in the simulation allows features to further reduce their energy by decreasing their total length.

Analysis could also consider the average length of the lines. We expect this part of the analysis to be less quantitative, and thus defer it to the ESI†. There is some arbitrariness to assigning the beginning and end points for the straight-line segments in both simulations and experiments (we do not attempt to force lines to begin or end on other lines or edges in order to create polygonal facets). This is in part due to the arbitrary threshold for observation (a line occurs only where bending stress is above the yield stress, or some curvature for simulations). In short, we find a reduction in the number of long segments in cut sheets, as was our basic hypothesis. A second interesting observation of this analysis is that crumpled sheets and cut crumpled sheets of similar density tended to have similar overall total line lengths. This is in agreement with the observations of Gottesman et al. (85), in that the total line length correlates with the compression resistance of the crumple.

2.6. Conclusions

In this work we conducted simple compression experiments and simulations on crumpled sheets with and without kirigami-like cut patterns. Experiments examined three different materials (PDMS, PC and Paper). No significant differences between cut and uncut sheets of the elastomeric PDMS samples could be detected in experiments. On the other hand, plastic materials (PC and Paper) show small changes in effective modulus when cut. CG-MD simulations were conducted on a model graphene sheet and results showed that cut graphene behaved similarly to the plastic experimental materials – small changes in the stiffness of the crumpled sheets were noted.

The CG-MD results also allow a detailed look at the internal structure and stress state of the crumples, where few significant changes were noted in the crumpled cut sheets compared to the uncut sheets. Of note, the location and orientation of the highly curved regions of the sheet (creases) were significantly altered by the cut patterns. Both simulated data and experimental data were analyzed by assigning a line segment to each visible crease (or high curvature region). Line segment ensembles showed a distinct perpendicular orientation to cut edges, which was more pronounced in higher density crumples. Because the overall changes in compression behavior were small, while the structural changes in the highly curved parts of a sheet was significant, we conclude that the orientation and patterns formed by the internal network of creases during crumpling are not significant to the macroscopic compressive behavior.

The similarity between cut and uncut crumpled sheets means that long range structures like the ridges shown in Fig. 2.4c. cannot play a significant role in the compression modulus of a crumpled sheet. Similarly, because the total length of the folds remained similar between cut and uncut sheets, while the orientation and length distributions differed, the idea of a fold as a long-range structure cannot be correct. This fits well with the conceptual model of a fold simply being a loci of point-like defects - the number of defects matters, not their orientation.

2.7. Author Contributions

W.J. conceptualized the study, lead the experimental data collection, analysed data and wrote the original draft. Y.L. conceptualized, acquired, and analysed computational data, contributed to the writing the manuscript, reviewed, and edited the manuscript. Z.L. contributed to the computational data acquisition. W.X. conceptualized the study, led the computational effort, supervised Y.L. and Z.L., acquired funding, and reviewed and edited the manuscript. A.B.C. conceptualized the study, led the experimental team, supervised W.J., contributed to data acquisition and analysis, acquired funding, and reviewed and edited the manuscript.

2.8. Conflicts of Interest

There are no conflicts to declare.

2.9. Acknowledgements

The authors acknowledge the support from the Army Research Office, award no.W911NF2010208. The simulations of this work used resources of the Center for Computationally Assisted Science and Technology (CCAST) at North Dakota State University, which were made possible in part by NSF MRI award no. 2019077.

3. ORIGAMI SWITCHABLE ADHESIVES *

3.1. Abstract

Creating a reusable adhesive that can hold objects on a wall and can yet be easily removed without causing damage has been a goal for researchers in the adhesives community for many years. Geckos and other climbing organisms demonstrate just this ability: to hold large loads (on-state) due to specialized digits and microstructures, yet they are also able to quickly peel their feet from a surface while climbing (off-state). Inspired by the simplicity of the gecko's geometric switching mechanism, we have investigated the use of origami design methods to create geometries that can transition from a stiff configuration to a more flexible and easily peeled configuration. Specifically, we examined three different origami designs (Kresling(108–110), Waterbomb(111) and Ron Resch (112)) fabricated in polycarbonate and supplemented with 3D printed structures. Although the polycarbonate could be coated with a commercial adhesive, we investigated the devices in contact with polydimethylsiloxane adhesive pads in order to chemically control interfaces and create a range of differing adhesion levels. We show that the devices are capable of moderate switching ratios (F_{on}/F_{off} up to ~ 50). We give a simple model to aid design and provide many options for scaling design performance through size, adhesive strength or through repetition of the pattern beyond a single unit cell.

3.2. Introduction

Reversible or switchable adhesives are generally useful in day-to-day life.(113) For example, sticky tape is frequently used to temporarily attach an object to a wall. Tape works

---

* The material in this chapter was co-authored by Wathsala M.A. Jayawardana, Theresa Elder, Timothy Twohig, and Andrew B. Croll. W.J. led the experimental data collection, analyzed data, and visualization, wrote the original draft, and reviewed and edited the manuscript. T.E. acquired, and analyzed data, and contributed to the wrote the original draft. T.T. acquired and analyzed data. A.B.C. conceptualized the study, led the experimental team, supervised, and contributed to data acquisition and analysis, acquired funding, and reviewed and edited the manuscript. This paper is published as a peer-reviewed article and reproduced from Ref.(107) with permission from the Royal Society of Chemistry.

well because it is difficult for the object to shear the tape off the wall, but the tape is easily peeled off when there is a desire to remove the object that it is holding.(114) Additionally, tape can be altered through cutting (kirigami) to create differences in peel strength or other mechanical properties depending on which end of the tape is peeled.(115–118) Unfortunately, sticky tape is limited in many situations. Consider hanging a painting on the wall. One could use a large portion of double sided tape between the painting and the wall but removing the painting then requires tremendous force (and will likely damage the wall). The tape cannot simply be peeled off because the solid painting frame confines the geometry. A smaller piece may enable removal without damage but may not have the strength to hold the painting at all. Hence, scaling is difficult. Other strategies aimed at solving this problem choose to decrease the tape's cohesive strength (say with a Velcro™layer). In this case removing the painting does not remove the tape but breaks it into a piece which remains on the wall and a piece that remains on the painting. This strategy typically utilizes a strong viscoelastic adhesive layer on a less flexible foam layer rendering the pieces of tape difficult to remove from the painting or wall without additional removal mechanisms being designed in.

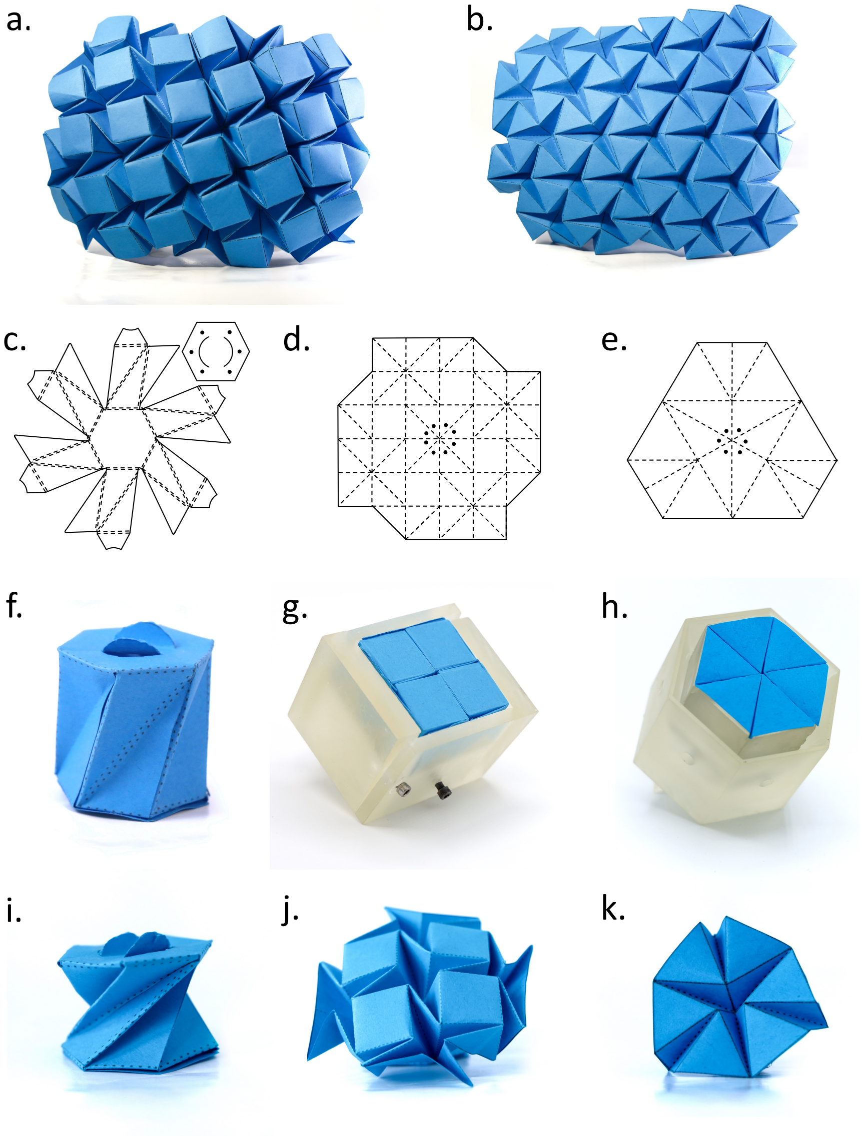

Figure 3.1. Origami adhesive structures. a. Square (waterbomb) origami tessellation pattern folded in paper. b. Triangular (Ron Resch) origami tessellation pattern folded in paper. c. Single cell Kresling origami pattern used for the switchable adhesive device. d. Single cell of the square origami pattern used for the switchable adhesive device. e. Single cell of the Resch origami pattern used for the switchable adhesive device. f. Stiff- on the state of Kresling origami device. g. Stiff- on state of square origami device. h. Stiff- on state of Kresling origami tessellation device. i. Soft- off state of the Kresling origami tessellation device. j. Soft-off(holder-off) state of the square origami device. k. Soft- off state of Resch origami device.

It is now well-known that many climbing insects and lizards demonstrate phenomenally well-controlled adhesive switching which scales with many different body sizes.(119) They can hold relatively large loads on arbitrary surfaces and geometries, and are able to release the adhesion whenever they desire. Careful observation of these animals has identified the importance of tiny structures on their climbing appendages which in turn has spurred the development of many microstructured "mimic" materials. (52–61; 120) While these engineered materials have many impressive performance metrics, they do not play a significant role in the animals adhesion switching abilities. (109; 120–124) In fact, many of the biological systems switch from high to low adhesion states when the animal moves between a low compliance normal or shear loading configuration to a peel configuration, similar to the piece of sticky tape discussed above.However, we note most insects and lizards do not use any viscoelastic material - their adhesion is dry. Essentially, both biology and industry have convergently evolved toward a peel mechanism for removal, rather than specialized materials.

In this work our goal is to develop a new, scalable method of switching between a rigid state capable of holding a large load and a soft state capable of easy peel removal. We exploit origami, the well-known paper folding art, in the design of our switchable adhesive devices. Our motive is to study origami designs that have two stable configurations: mechanically stiff for the load-bearing state and flexible to facilitate peel in the removal state. In this work three origami designs which have two stable mechanical states were studied. Each design can transition between a rigid configuration (on-state) and a soft configuration (off-state). The switch in compliance of the devices between on and off states can lead to changes in peak load held, however, in this case, the switching is driven by a change in interfacial fracture geometry (a post geometry to a peel geometry). While most tapes rely on a lossy adhesive (a pressure sensitive adhesive), we note that this is not necessary for a device to peel. All that is needed for peel is a thin flexible layer which can deform and focus stress at the crack tip and create a progressive failure front. This geometry can be found in many origami designs.

First we consider the traditional Kresling pattern (108–110; 125–128) which is characterized by a linear array of mountain and valley folds, which define triangular facets and can be arranged into a cylinder-like shape. This pattern was observed many years ago in the buckling of cylinders(125), but first discussed as origami by Biruta Kresling (108) by studying microscopic, deployable patterns in natural organisms. Bhovad et al. further developed the pattern into a multi-stabile configuration (110) to use in robotic applications. The pattern used here is shown in Figure 1c, f, and i, and was developed with perforated crease lines similar to that of Hwang.(129) Constructed designs are bistable, having two modes that can be switched through torsion. We consider the twisted state as the soft state and the untwisted state as the stiff state for this pattern. Generating an array of Kresling devices is feasible, although would require the use of more than one sheet.

Next we consider a repeated square pattern, commonly referred to as the “water bomb”, (111) is shown in Fig. 3.1a, d, g, and j. The unit cell of the square pattern consists of four folded squares and showcases a “curved” open configuration (the facets are not coplanar) as well as a closed flat configuration (Fig. 3.1g). Furthermore, we point out that a repeated pattern of unit cells resembles the contact-splitting mechanisms utilized by insects.(121) By possessing numerous small contacts that collectively form a substantial contact area, insect legs effectively partition the contact region. The ability to repeat the square pattern provides another advantage in the form of tunable surface area. By incorporating more squares into the lattice, the overall size of a device can be modularly scaled enabling, for example, the creation of rectangular or other “tetris inspired” configurations. This tunability offers flexibility and adaptability in utilizing the square pattern in various applications.

Finally, we consider a hexagonal design in order to increase functionality. The Ron Resch pattern consists of folded equilateral triangles arranged in a periodic radial formation, as depicted in Figure 1b, e, h. and k. Once again, for simplicity, we focus on a single unit cell of this tessellation (Fig. 3.1h). When the shape is folded, six of the triangles, positioned radially around a central point are compressed together, resulting in the formation of a flat-surfaced hexagon (the triangular facets are coplanar). This flat surface can be pressed flush against another flat surface, establishing a high degree of contact area. Upon removal of the external load that maintains the compressed state the triangles begin to separate due to the energy stored in the pattern's creases. As the shape opens up, the triangles tilt out of the plane, causing a gradual curvature that prevents the structure from laying flat against a surface. Thus, the system also exhibits two distinct modes: an "on" mode characterized by strong adhesion when the triangular facets are coplanar, and an "off" mode characterized by weak adhesion when the triangles separate and develop a non-planar surface shape.

The structure of this paper unfolds as follows: we commence by detailing our materials and methods within the experimental section. Subsequently, in Section 3, we develop a simple scaling argument to describe the adhesive performance of the different states and make predictions of how the switching ratio (adhesive force in the on state to adhesive force in the off state) will scale with increased contact area or changes in overall interfacial strength. Next, in the results and discussion section, the peak adhesion forces for three different origami-based designs in rigid and soft states are reported and discussed. We highlight the most effective mechanism that combines additively manufactured components with the origami shapes can achieve switching ratios of up to approximately 50, though more often show a moderate value of approximately 5. The manuscript ends with a succinct summary and key conclusions.

3.3. Experimental

3.3.1. Device Fabrication

Three origami patterns (Figure 3.1c, d, and e) were printed out on paper and then folded into prototypes. The prototypes were used to refine the area of interest for the unit cell and to test the switching mechanism. Then the selected unit cell patterns were redrawn in PowerPoint software where several minor modifications to the pattern were made, such as replacing regular lines from the design with perforated lines to facilitate more accurate, guided folding(129). Patterns were uploaded to the Cricut designing space and then loaded to the Cricut cutter. Ultimately, the patterns were cut in polycarbonate sheets (thickness 128 microns) used as received from McMaster-Carr company.

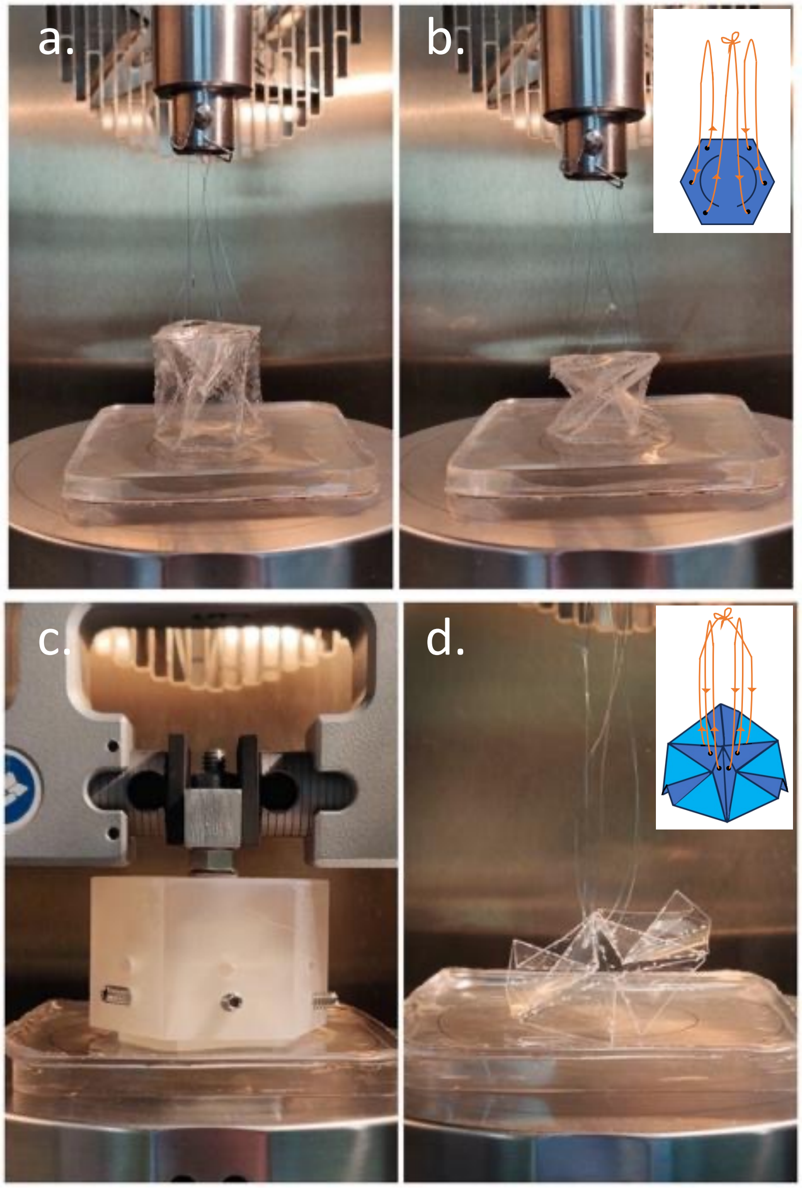

Figure 3.2. Images of the experimental setup. a. a kressling device in the on state. b. A Kressling device in the off state. c. A Resch device in the on state. d. A Resch device in the off state, where the holder body has been removed.

The first pattern, the bi-stable Kressling pattern (Fig. 3.2a and b) used polycarbonate as outlined above but was supplemented with some double-sided tape to adhere overlapping elements of the pattern and form the cylindrical final state. In principle solvent or heating could “weld” the pieces together for one-material construction. The device switches between a rigid state and a soft state through a rotation.(129) We used a thin, rigid string (Zebco Outcast Monofilament Fishing Line) to apply forces to the top of the device in order to reduce the need for complex orientation schemes.

The other two origami switch patterns were more efficient when supplemented with a 3D-printed “holder”. 3D-printed cubes and triangular prisms designed to fit inside the origami patterns were rendered with clear methacrylate resin. Figure 3.2c. shows the assembled device during testing. The soft state (off-state) can be achieved by releasing the “holder” and allowing the patterns to articulate freely. To perform pull-off tests, we used the same technique as the previous design, passing a string through the pattern in order to apply forces.

3.3.2. Substrate Fabrication

To test device performance, it is useful for at least one side of the system (adhesive device or substrate) to have easily controlled adhesion. We have successfully coated polycarbonate sheets with a pressure sensitive adhesive in the past, but the adhesive allows little tuning of the interaction. Here we elect to use a weaker but tunable elastomer layer on the substrate in order to create more experimental control. Specifically, Sylgard 184 polydimethylsiloxane (PDMS) was used in 20:1, 30:1, 35:1, 40:1, 45:1, and 50:1 weight ratio (prepolymer to crosslinker). The polymer mixture was then drop cast into polystyrene dishes to make thick ($\sim$ 1 cm) adhesive pads. We don’t expect the moduli of these materials to have a strong frequency dependence in the range of speeds explored in this work. Typical DMA can be found in reference 130.

3.3.3. Mechanical Testing

Mechanical tests were performed on a universal test frame (Instron 34TM-5) for all three origami devices. Adhesive PDMS pads were placed on a compression platten, and a clamp was used to pull a string attached to each device. With the additional printed holders, Instron grips could be attached directly to the device. Tests began with bringing a device into contact with the adhesive pad using a pressure such that full (macroscopically observed) contact would take place between the device and the PDMS layer. This observation could not be made with the opague, filled devices so the same pressure was used in the on (opague) and off (observable) cases. After this recorded forces would return to approximately zero (no tension in string or clamps open). Clamps were then gently closed on a device, or string tension was increased. Forces and displacements were recorded until a crack between the substrate and device nucleated and propagated across the whole interface.

3.3.4. Alignment

In the device's on state, we loosely secure the holder to the top grip jaw of the Instron, as illustrated in Figure 2c. To ensure proper alignment, the Instron is then manually lowered until the origami holder makes contact with the adhesive pad on the bottom. It is important to note that the setup isn't entirely rigid at this stage. There is some flexibility facilitated by our nuts-and-bolts configuration which allows for slight movement by hand. Once alignment is complete, the grip is tightened.

During the off-state, where origami designs are affixed to strings, we thread all string loops through the Instron's upper connector. Gradually, we lower the setup while applying gentle tension to the strings, aligning the top strings and the bottom of the pattern with the upper connector rod until they touch the adhesive pad. Note that each string is the same length and can slide along the upper Instron connector. Before data collection, we perform a test run and manually adjust the Instron's upper connector to ensure proper alignment.

3.3.5. Adhesion

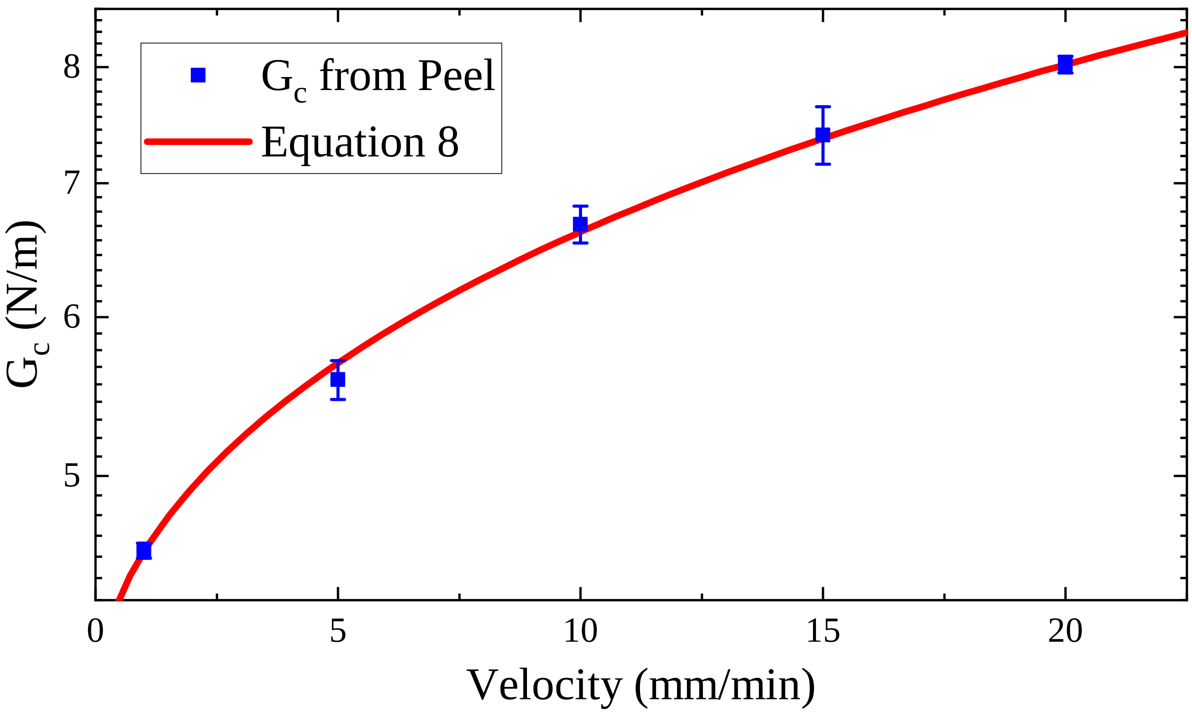

Figure 3.3. Results of peel adhesion tests between a thin PC strip and 40 to 1 PDMS.

While it is not the focus of this manuscript to exhaustively evaluate the strength of adhesion between PDMS and PC, it is useful to have direct measures with which the scaling models can be compared. We therefore conduct standard 90° peel tests with a 50 mm wide strip of 128 μm thick PC and a mat of 40 to 1 PDMS. Each test was repeated 3 times and the average is reported in figure 3.3, with error bars given by the standard deviation of the measurements. We note that the data is well fit by equation 3.8 with $n = 0.6$, $v^* = 18.2$ mm/min and $G_0 = 3.9$ N/m.

3.4. Scaling Model

The failure force, F, of an adhesive often scales as,

$$F \sim \sqrt{\frac{G_c A}{C}}, \tag{3.1}$$

where C is the compliance, A is the contact area and G_c is the critical energy release rate (equivalent at low speeds to a work of adhesion calculated from substrate and adhesive surface energies).(113) While not true for all geometries, Eqn. 3.1, works well for many tests of the probe variety and more importantly identifies the three pillars of adhesion (chemistry, contact area, elasticity). Note that peeling does not directly follow Eqn. 3.1, and must be treated separately.

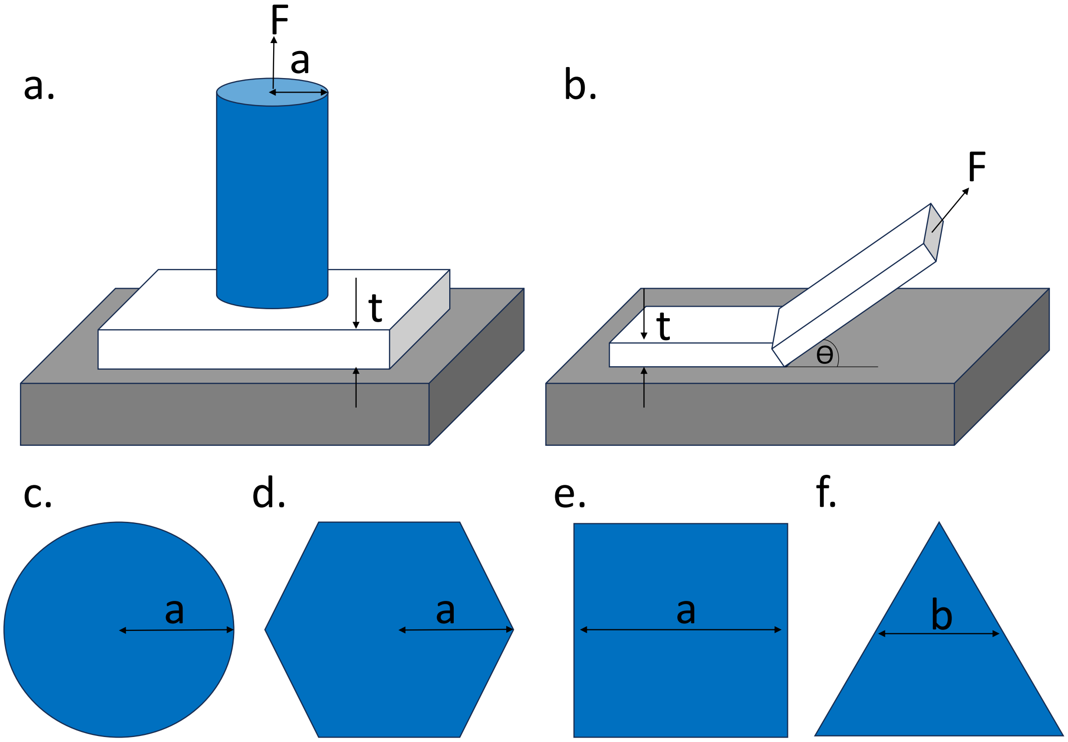

Figure 3.4. Geometric details of the models. a. a post adhesion measurement. b. a peel experiment. c.-f. different post cross-sections.

From our observations of the failure modes during pull-off, we identify all off-state failure as peel type (See †ESI for a movie of the off-state failure). The peel can occur in this state because the polycarbonate can easily flex and bend away from the surface during this stage of operation. In the on-state, we desire high stiffness in the devices and thus hypothesize that the device operates as a solid post. The rigidity of each device changes, so the model may be less accurate for the softer waterbomb and Kressling devices, but seems robust for the Resch (hexagonal) device.

When detaching/debonding an origami device from a substrate, the scenario for the crack will differ depending whether the device is in its stiff (on-state) or soft (off-state) configuration. We hypothesize that the on-state devices resemble a cylindrical post type pull-off test. If this is the case, then an effective radius, a, can be identified and the compliance will scale as:

$$C \sim \frac{1}{2\overline{E}a}. \tag{3.2}$$

Where,

$$\overline{E} = \frac{E}{(1-\nu^2)}, \tag{3.3}$$

E is the Young's modulus, and ν is the Poisson's Ratio. Combining with Eqn. 3.1, the peak force can be identified as:

$$F_c \sim \sqrt{2G_c A\overline{E}a}. \tag{3.4}$$

If area scales as $A \sim \pi a^2$ then Eqn. 3.4 can be further simplified,

$$F_c \sim \sqrt{2\pi\overline{E}G_c a^3}. \tag{3.5}$$

When transitioning to the softer "off" state, we expect the system compliance to change. More important is that the compliance change, due to the thin layer contacting the substrate surface being free of constraint, allows new modes of adhesive failure. In short, peeling is now possible (and observed) during failure, initiated along each face of the perimeter of the contact patch. The change in device geometry, from post-like to peel, means Eqn. 3.5 is no longer useful for predicting the soft state adhesive performance.

To model the soft state, we switch to the peel theory described by Kendall and others.(114; 131) The peel geometry is shown in Fig. 3.4b, where a thin tape with thickness t and width a creates a peeling force F which scales as (or is exact when $\theta = 90$),

$$F_c \sim G_c a. \tag{3.6}$$

We assume this scaling to apply to each facet that peels during separation. Nuance will, of course, add complexity. For example, the peel width for a square facet will remain constant during peeling. However, the hexagonal origami pattern creates triangular facets which means the peeling width will decrease as a crack propagates from the edge towards the center of the device. Fig. 3.4 f visually demonstrates this phenomenon, where the width (b) of a triangle is a variable rather than a constant. Regardless, the peak force of detachment should still scale as the largest dimension, a, meaning that the scaling of Eqn. 3.6 should remain relevant.

Ultimately, the two different regimes allow us to model the switching ratio of a device as:

$$R \sim \sqrt{\frac{2\pi \bar{E} a}{G_c}}. \tag{3.7}$$

Eqn. 3.7 shows that the switching ratio can be increased by larger devices and counter-intuitively is decreased by stronger interfacial interactions. This kind of switching design, which alternates between post and peel, could therefore be useful for rigid, nanoscale devices. For example, the switching ratio for a gecko setae, ($E \sim 10^9$ Pa , $a \sim 10^{-9}$ m) where van der Waals forces dominate ($G_c \sim 10^{-2}$ N/m) would be of order 100.

3.5. Results and Discussion

The force vs displacement data obtained from typical experiments is presented in Figure 3.5. Figure 3.5a shows the performance of the Kressling patterned structure of 1.9 cm dimensions at a speed of 10 mm/min. In the on-state a peak force of ∼ 3 N is reached, and in the off-state a force of ∼ 2 N is reached for a switching ratio of 1.5. We attribute the unimpressive performance of this structure to the small change in compliance between the on and off states. The compliance when directly measured for this experiment is found to be 1.7×10^{-3} m/N in the on-state and 4.4×10^{-3} m/N in the off-state, verifying this claim. In short, the ridged state was not stiff enough, and the soft state was still too ridged to easily peel.

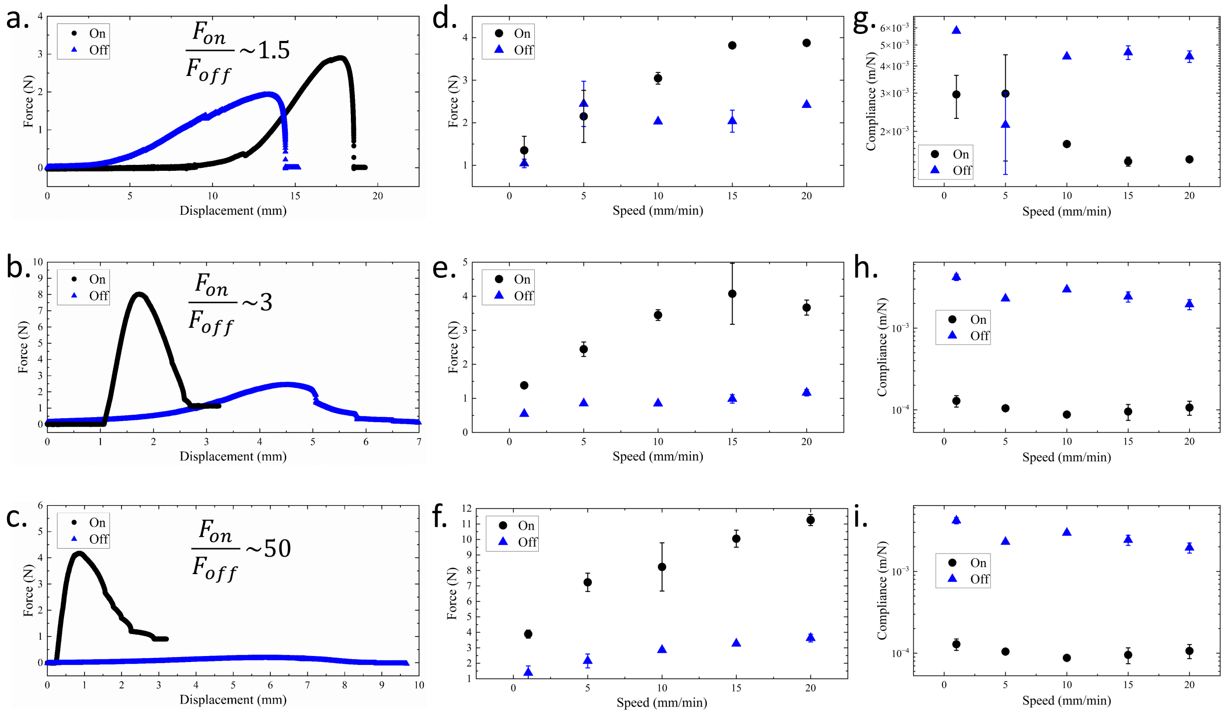

Figure 3.5. Force measurements for origami devices. Force vs Displacement curves for a. Kresling b. Square c. Resch Origami patterns at a speed of 10 mm/min. d., e., and f. Speed dependence of peak force for the corresponding devices. g., h., and i. Compliance as a function of speed for the corresponding devices.

We believe the structure could be improved with different material choices, for example, metal or thick thermoplastic placards with hinges rather than being formed from a single sheet as in pure origami. Another limitation of the Kresling pattern is that its contact remains a solid hexagon for both on and off states, rather than splitting the contact area into an array of smaller squares or triangles.(121) It has also been shown that the adhesion is twice as strong in the center of a contact patch compared to its borders (122), motivating a change in our design.

To alter stress concentration at contact we next used the waterbomb design, which in addition to breaking the contact patch into 4 units remains relatively open after folding. The open structure then allows easy supplementation of the origami folded sheet with additional structure. In this case, solid cubes of material were designed to fit into the folded PDMS sheet and an enclosure which could clamp down on the cubes and ultimately decreasing compliance of the on state. One could envision robotic actuation of the cubes, though this is beyond our current capabilities. With the supplemented structure, the on state is very stiff, and the off state can be reached by removing the outer clamping component. Figure 3.5 b shows the outcome for the on and off states of the waterbomb device. In this case a ratio of 3 is reached, doubling the performance of the Kressling design. The limitations of this device become apparent when observing the adhesive failure in the on state. Here the corners of the square face often bend during failure indicating that the design, while stiffer, was initiating peel in the on state (rather than a behaving as a rigid post).

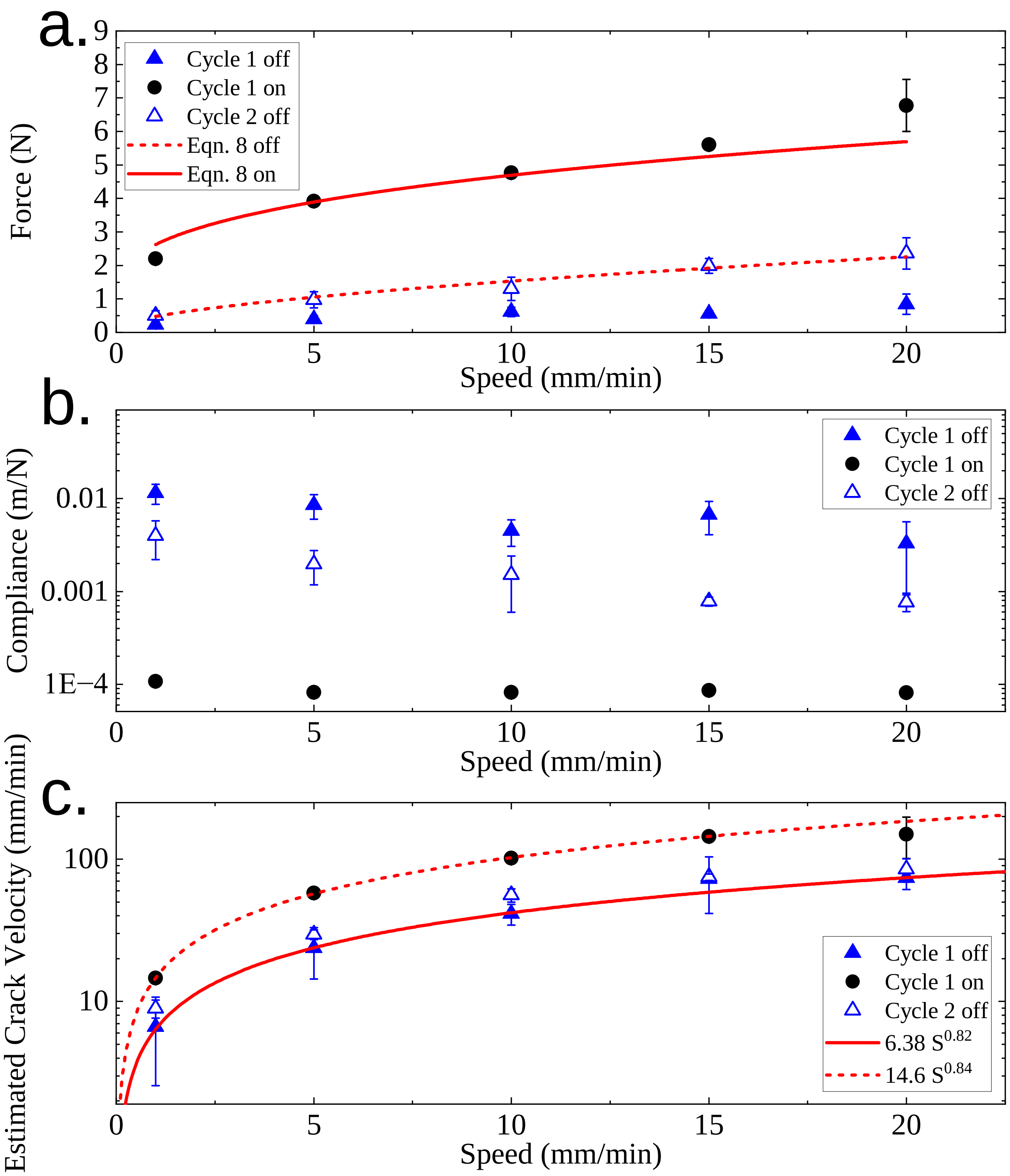

Figure 3.6. The effect of creep. solid blue triangles depict data collected with a 5 cm Resch device at various speeds. The same device was then immediately tested in the on state (solid black circles). When the on-state measurement was complete, the off-state measurement was repeated (open blue triangles). We note a significant increase in the off state forces due to creep in the polycarbonate. Equation 3.8 is fit to the on state data (solid line) and the second cycle of the off data (dashed line). Fit parameters are discussed in the text.

Finally, a hexagonal Ron Resch pattern was developed. In this case a hexagonal unit cell was used, creating a contact face of 6 triangular units. Again, the folding is open and can be supplemented with triangular prisms and a clamping outer shell. Results showed considerable improvement resulting in a switching ratio of up to 50. In this device, stiffness is high in the on state but the peak force of the off state was more noticeably reduced. This is for two reasons, first there are 6 separate units to initiate peel (rather than 4 or 1), and secondly the larger amount of folding results in considerable elastic energy storage. The stored elastic energy aids peeling because unfolding the structure causes the contacting surface to lose its planarity. Occasionally, devices would spontaneously open resulting in a force of zero in the off state, and thus a ratio of infinity. We specifically increased substrate adhesion to the point where this became uncommon in order to be able to systematically investigate the details of the fracture process. We also note that after holding the device in the folded state, creep occurs in the folds reducing their drive to open. Devices that had creeped significantly due to the materials elasto-plasticity, showed a significantly reduced switching ratio (to approximately 6) indicating a clear path towards designs with increased performance (increasing the sheet elasticity). Finally, we note that the changes in compliance (Fig. 3.5i) mirrors the increased switching ratios of this device.

Additionally, as one would expect for a plastic material such as polycarbonate, repeated opening and closing cycles reduced the “spring” of the fold and thus the switching ratio.(132) Figure 3.6 shows a set of experiments with a 5 cm Resch device to illustrate the effect. In this experiment, the device is tested in the off state with a new PC sheet, then the on state, then the off state is repeated. As is typical, the initial off-state measurement shows a much lower release force than does the repeated measurement (the ratio for the fastest speed drops from 30 to about 3). In what we report below, we ensure to used “worked” polycarbonate as this is a more realistic state for the device and more replicable measurement.

The speed a test is performed at is well known to affect adhesion of soft materials due to viscoelastic losses at the crack tip.(133–136) Figures 3.5 d, e, and f, depict the variation in peak on and off forces as a function of Instron speed. It is evident that both the peak on and off forces increase with speed, and the difference between the peak on and peak off forces also increases with speed. The trends of Fig. 3.5 could, in principal, be related to the predictions of equation 3.5 and 3.6 through the commonly used empirical formula describing the speed dependence of the energy release rate ($G_c(v) = G_0(1 + (v/v^*)^n)$, where G_0 is the work of adhesion, v^* is an intrinsic molecular speed and n is an empirically determined exponent). However, since we do not directly track the speed of the interfacial crack itself, it is unlikely that this would be meaningful as it is likely that the change in geometry between the on and off states will also affect the crack speed. Direct measurements of the crack speed were not possible due to the opaque nature of the devices.

$$G_c(v) = G_0(1 + (v/v^*)^n) \tag{3.8}$$

where G_0 is the work of adhesion, v^* is an intrinsic molecular speed and n is an empirically determined exponent. However, this empirical relation requires several fit parameters, meaning that the accuracy of any unknown fit with it will be somewhat inaccurate. Fitting with n fixed at 0.6 (which is common for silicones), for example, to the off-state data in Fig. 3.6 yields $v^* = 0.18$ mm/min and $G_0 = 6.9$ N/m. On-state data, which is complicated by the additional power law in Eqn. 3.5, can be fit if we additionally hold $v^* = 0.18$ mm/min. Here we find $G_0 = 7.8$ N/m. The v^* values are a bit higher than expected, and the two states lead to slightly different G_0. However, both values of G_0 are close to what is found via peel. The precise variation on G_0 is likely caused by differences in crack speed between the two geometries, differences in compliance between the two measures, and to the imprecise nature of the scaling models used.

The compliance of the device for each cycle is plotted in Fig. 3.6b. Here we see the largest compliance (softest device) is the pre-fatigue origami. In this case there appears to be a weak decrease in compliance as the test speed is increased. On the other hand, the stiffer off-state device shows much less compliance (one or two orders of magnitude) and very little speed dependence. In general, increased compliance leads to decreases in peak force (i.e. Eqn. 3.1). While this is explicit in the scaling argument for the peak force of a post type sample (Eqn. 3.5), it is more complex in the case of peel and beyond the simple scaling argument used here (Eqn. 3.6). Recent theoretical work does verify that the same concept applies to peel, so we should expect some of the speed dependence of the force in the off-state to be related to the changing compliance.(137)

Direct measurements of the crack speed were not possible due to the opaque nature of the devices. However, estimates can be made from the device size (a) and the time it takes for the force to drop from its peak value to zero. Fig. 3.6c shows that the estimated speed is approximately linearly related to the machine speed and that the on-state device has cracks that move about twice as fast as in the off-state. Using the peel data (Fig. 3.3) as reference, this would imply that the on-state device is probing a larger G_c than the off state, though the magnitude of the difference would be less than an order of magnitude. The combination of the two effects, changing compliance and crack speed likely contribute to the differences in G_0 noted above.

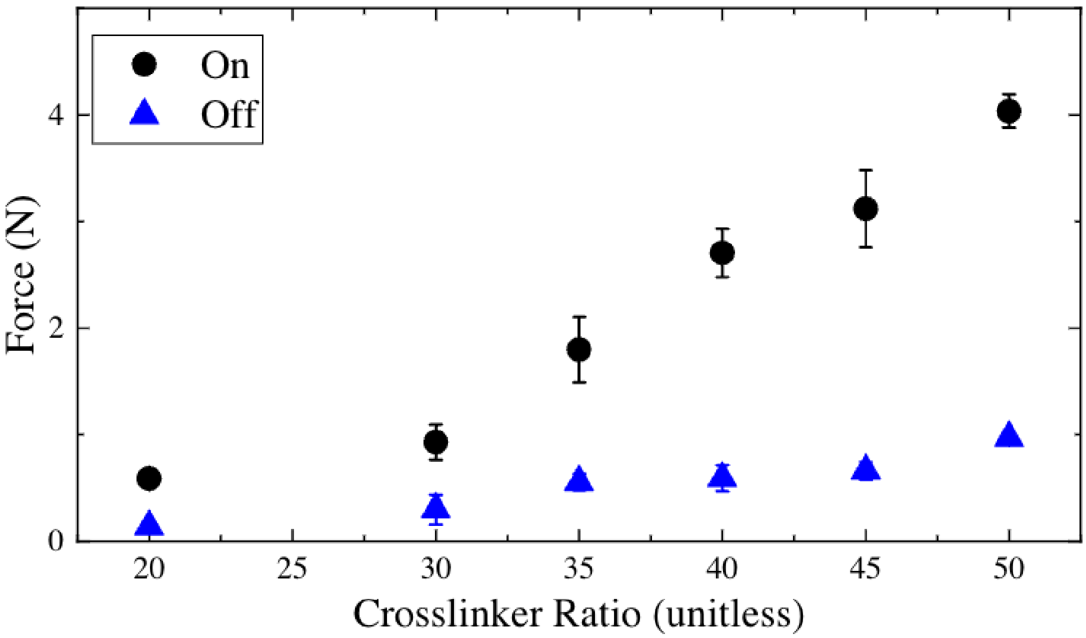

Figure 3.7. The effect of G_c. Peak force measured in the on state and in the off state plotted as a function of cross-linker density. a. As discussed in the text, both on-state and off-state forces increase with decreasing cross-link density. b. Each curve in a. can be normalized by the lowest cross-link density measurement (20 to 1). Both curves collapse to a master curve showing how both modulus and G_c change identically for both modes of operation of the devices. Error in a is a standard deviation from repeated measurement. In b. error is calculated from the error in a. using standard methods

Our experiments did permit us to directly alter G_c through changes in the adhesive substrate. Because we found the best behaviour with the hexagonal device, we proceed to explore G_c with this particular geometry. Figure 3.7 shows how the peak force for both the on state and off state increases as crosslinker density decreases for the 5 cm diameter device. In both cases a monotonic increase in force is noted. This again agrees qualitatively with Eqn. 3.5 and 3.6 because G_c will increase as the crosslinker density drops.(138–148) We also note that the modulus will drop as the crosslinker density decreases, which does not necessarily agree with the trend shown for the on-state forces.(138–148) Once again, without knowledge of the exact crack speed, it is not possible to make a direct quantitative comparison (E will not appreciably depend on crack speed, but G_c will). However, if we assume the accuracy of the relation, $G_c = 200E^{0.49}$, developed in 138 then both on and off-state data will scale linearly with G_c. If this is true, then normalizing each set of data by the peak force measured on a 20 to 1 sample would remove any dependence on other variables and we would expect data from both the on and off state to fall on a single master curve. Figure 3.7b shows the data normalised in this way, and indeed shows a collapse to a master curve as expected. This plot can be considered a quantitative measure of the relative difference in G_c for these materials and again an indication of the accuracy of the scaling models we use in this work. For example, we expect the 50 to 1 material to have a G_c of about 2.6 times that of the 30 to 1 sample. The data of reference 138 shows a ratio of about 3 (note the work in the reference is for G_c between glass and PDMS, not polycarbonate and PDMS as is the case here).

If we make the assumption that the crack between the device and the adhesive interface will propagate at the same speed if the driving speed and the material are fixed, then a semi-quantitative evaluation of Eqn. 3.5 and 3.6 is possible if the focus is on geometry. To do so, several different sizes of hexagonal device were constructed and on and off-state forces were measured against a slab of 40:1 Sylgard. Figure 3.8a. shows a plot of the triangle dimension (a) against subsequent detachment forces for experiments run at 5 mm/min. For the on state a represents the post diameter, whereas in the off state a represents the width of the peeling region. The agreement between the scaling predictions is noteworthy - on state data is well fit with a power law of $F \sim C_{on} a^{3/2}$, and off state data is consistent with an $F \sim C_{off} a^1$ power law fit. We find $C_{on} = 1330$ N/m$^{3/2}$, which would be consistent with a G_c of approximately 51 N/m (given the modulus of 40:1 Sylgard is about 50 kPa). On the other hand, we find $C_{off} = 42$ N/m, which would imply $G_c \sim 42$ N/m, which is not far from the on-state result.

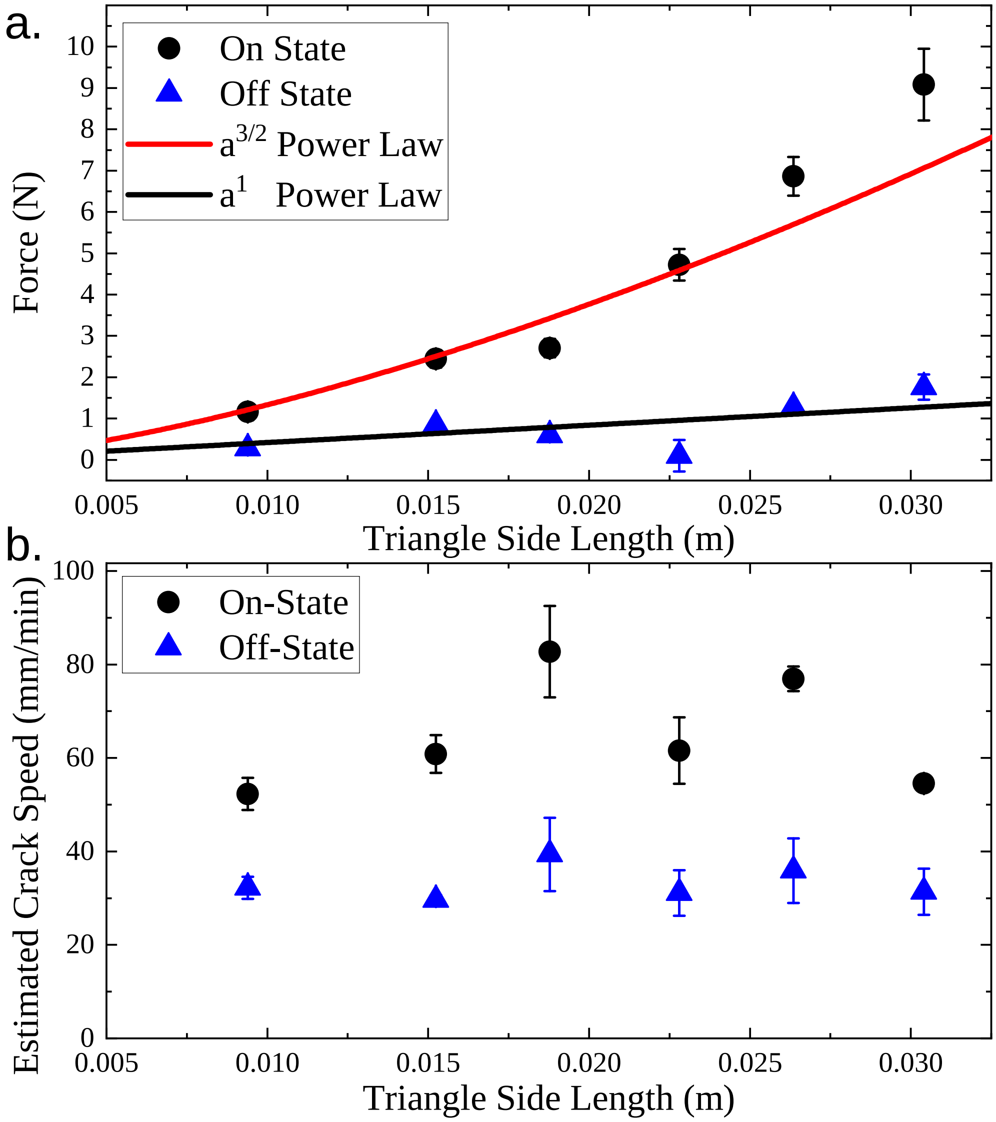

Figure 3.8. Size dependence of adhesive force. a. Plot shows force data for various sized devices in the on (black circles) and off (blue triangles) states. Fits to the model described in the text are shown. b. Estimated crack speed for each device and state. While some noise is evident, both on and off states show relatively constant crack speeds. The on-state has a higher crack speed than the off-state.

To verify the assumption of constant crack speed, we once again estimate the speed of the crack from the force-displacement data. Figure 3.8 b. shows that crack speed does not vary with the device size (though the data is noisy) and that the on-state device has a higher crack speed of approximately 65 mm/min when compared to the off-state cracks (speed approximately 33 mm/min). Once again the difference is approximately a factor of 2 as noted earlier. At these speeds the peel data of figure 3.3 would suggest $G_c = 12$ N/m for the on-state and 9.5 for the off-state. The ratio between the accepted peel G_c values and those obtained via scaling indicates that a constant of order 4.4 to 4.2 is needed to make the scaling models quantitative.

3.6. Conclusions

In conclusion, the exploration of reversible or switchable adhesives holds great promise in addressing challenges related to temporary attachment and detachment of various applications. In this work we found that origami devices with two stable states could be used to create mechanically switchable adhesive devices. We found a Kresling pattern allowed a switching ratio of 1.5, a waterbomb pattern a ratio of 3, but a Ron Resch patterned device could attain a ratio of 50, but more typically showed a ratio of about 6. The difference in the latter ratios being attributed to the degree of plasticity in the creases of the origmai shape. Increased working of the creases reduced the switching ratio.

Switching ratios typically increased with increasing motor speed, and showed a predictable size dependence. Further, compliance is found to change dramatically between the on and off states and cracks are found to propagate approximately twice as fast in the on-state as in the off-state. Ultimately, the function of our devices have proven the utility of origami based design for switchable adhesive development. We believe that further investigation of supplemented origami devices could lead to devices with improved performance and that could be easily integrated into soft robotic gripping systems. In this case, origami grippers would be ideal for repetitive pick and place operations which don't require huge switching ratios for function but do require low power consumption. Finally, other modern techniques in adhesive design could be combined with the basic idea behind our mechanical switching scheme. For example, origami schemes could be combined with directional peel through kirigami for increased control over the adhesive performance or with modern post-style adhesives for increased roughness and dirt tolerance.

3.7. Author Contributions

Conceptualization – ABC, formal analysis – ABC, TE, WJ funding acquisition – ABC, investigation – TE, WJ, TT, methodology – TE,WJ, ABC, supervision – ABC, visualization – WJ, ABC, writing – original draft – WJ, TE, writing – review & editing – WJ, ABC.

3.8. Conflicts of Interest

There are no conflicts to declare.

3.9. Acknowledgments

The authors gratefully acknowledge the support of the National Science Foundation through grant number CMMI-2011681.

4. IMPACT AND ENERGY ABSORPTION WITH STICKY CRUMPLED MATTER

4.1. Abstract

A simple two-dimensional sheet can turn into a complex disordered spherical structure consisting of basic structural features (bends, folds, ridges and D-cones) when the sheet is confined by a shrinking sphere (or your hands). Such a crumpled state will have dramatically different mechanical properties than just a sheet of paper. Crumples, for example, are quite rigid even though there are often more than 75% air. Crumples have also been shown to be good absorbers of energy from an impact. In our study, we experimentally observe impacts from simple ball drop experiments on sticky crumpled matter using high-speed photography with a FASTEC IL5 camera. We show how these sticky crumples can be useful as a replacement of highly engineered form structures for protective layers.

4.2. Introduction

Impacts resulting from sudden collisions between objects cause significant changes in momentum and kinetic energy, often resulting in damage due to the high forces and short durations. Mitigating impact is crucial in diverse areas, including vehicle engineering, sports equipment design, and transportation of goods. Often, the goal is the protection of delicate body organs through specialized gear such as helmets, knee guards, and sports-specific footwear(149). Traditionally, engineers have relied on foams but recent optimized designs have moved towards complex and costly engineered materials and structures(150–152). Surprisingly, a simple crumpled sheet has been commonly used for centuries in packaging fragile objects for transportation And yet, has received little attention from scientists and engineers.

The transformation of a two-dimensional sheet into a disordered spherical structure involves the creation of repeated structural sub-features like bends, folds, ridges, and D-cones. This results in a network of air pockets and structure, conferring rigidity to the crumpled sheet.

(24). The concept of creating 3D structures from a 2D sheet draws inspiration from the art of origami, where folding and shaping paper yield intricate patterns. Crumples, however, represent a form of origami with a complex disordered folding pattern. (15) While origami impact mitigation applications using polymers such as extruded acrylic (150), carbon fiber reinforced polymer (151) and metals such as brass (153), stainless steel (154) have been explored, studies on the impact absorption of sticky polymer crumpled sheets remain relatively unexplored, likely due to their complexity.

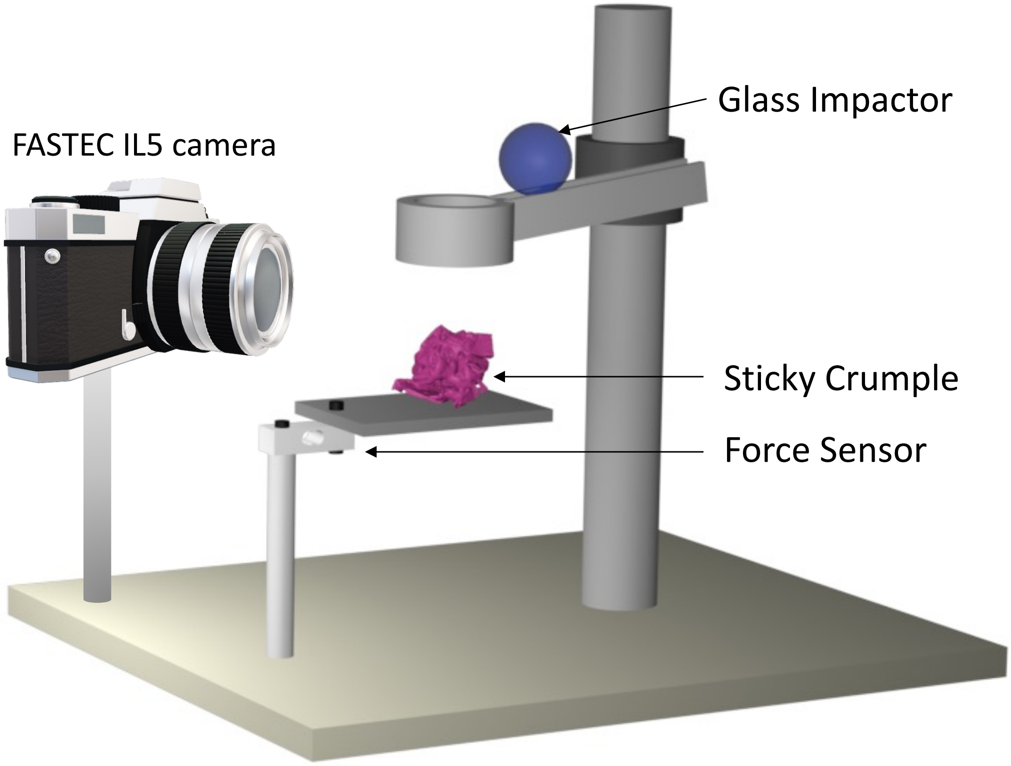

Figure 4.1. Fast camera photographs of before during and after impact of the ball drop experiment of a,b,c)Metal plate d,e,f)40:1 40:1 PDMS block g,h,i) 40:1 PDMS block with cornstarch layer on top to remove adhesion j k l)PDMS crumple

In this work, the impact absorption capabilities of sticky, crumpled sheets were investigated. We hypothesize that the sticky material will effectively dissipate impact energy, as well as preventing the crumple from unfolding or prematurely compacting. We build on previous work exploring the low-speed compaction of sticky crumpled matter by experimentally observing impacts from a simple ball drop experiment. We use high-speed photography and vary sheet thickness, material properties, impact momentum (0.0015 kg m/s to 0.0075 kg m/s) and adhesion. We observe the peak forces for the crumples greatly reduces with increased impact time compared to our control experiments which allows us to conclude that sticky crumpled sheets could be used as efficient energy absorption materials that are simple and inexpensive to produce.

4.3. Experimental

Polymers have unique, easily varied properties and are used extensively in medical and engineering applications. Elastomers made of polydimethylsiloxane (PDMS) have special features such as hydrophobicity, optical transparency, biocompatibility, adhesion, flexibility, contamination resistance, long term endurance and availability for low price. PDMS can be used as a protective coating for electrical insulation, anticorrosion, and antifouling applications (155). Sylgard 184 is a simple to use commercial PDMS system that has the advantage of easy modification of its modulus and adhesiveness through a varied crosslink ratio. In this study, we use Sylgard crumples as a model protective layer material and a glass ball as the impactor due to the wealth of knowledge of glass/PDMS interactions.(156)

Sylgard films were created with a drop-casting method. In the drop-casting method, the polymer solution was added to a container dropwise until it uniformly spread through the bottom of the whole container to the desired thickness. If the solution was not uniform, holding the container at an angle will allow the gravity to spread the solution uniformly throughout the container. The solution was then placed on a flat, level surface to achieve further uniform spreading before it was placed in a vacuum oven and degassed. When no bubbles are left, the PDMS solution is heated at 80 degrees for 1 hour, before being cooled to room temperature.

Our basic experimental set up consists of a rail and a "director" tube to aim the dropping ball towards the crumple. Glass impactors used are decorative marbles about 3g to 5g weight with the width of 14mm to 15mm range. Glass impactors were cleaned using acetone before starting the experiment. During the experiment, glass impactor was carefully placed stationary about the same position on the rail to free fall along the rail and directed on top of the crumple by the director tube. Then experiments were repeated with the different height levels between bottom of the rail to bare cantilever plate (2.5 inches to 12.5 inches) to achieve different initial momentia.

High-resolution videos of the impact using FASTEC IL5 camera with a strobe light were recorded together with force measurements by a strain gauge force sensor attached to a metal cantilever. The strain gauge was connected toan instrumentational amplifier (INA126) coupled with National Instrument's data acquisition device (NI-daq). By analyzing each frame of the slow-motion video using tracker software, we analyze the velocities before and after impact. Amplified force sensor data were collected through MATLAB. We repeat this experiment for various initial impact speeds by adjusting the heights of the rail-tube system and changing the adhesion properties of the base crumple materials, and the impactor weight and size.

We primarily focus on 4 different experimental systems. We create crumples as the main focus of this work and use as control experiments a bare cantilever plate, bulk sticky PDMS, and bulk non-stick PDMS. Non-stick PDMS was created by applying a monolayer of cornstarch on its surface. Only crumples with adhesion are used because if we remove the adhesion the elastic sheet will spontaneously open long before impact.

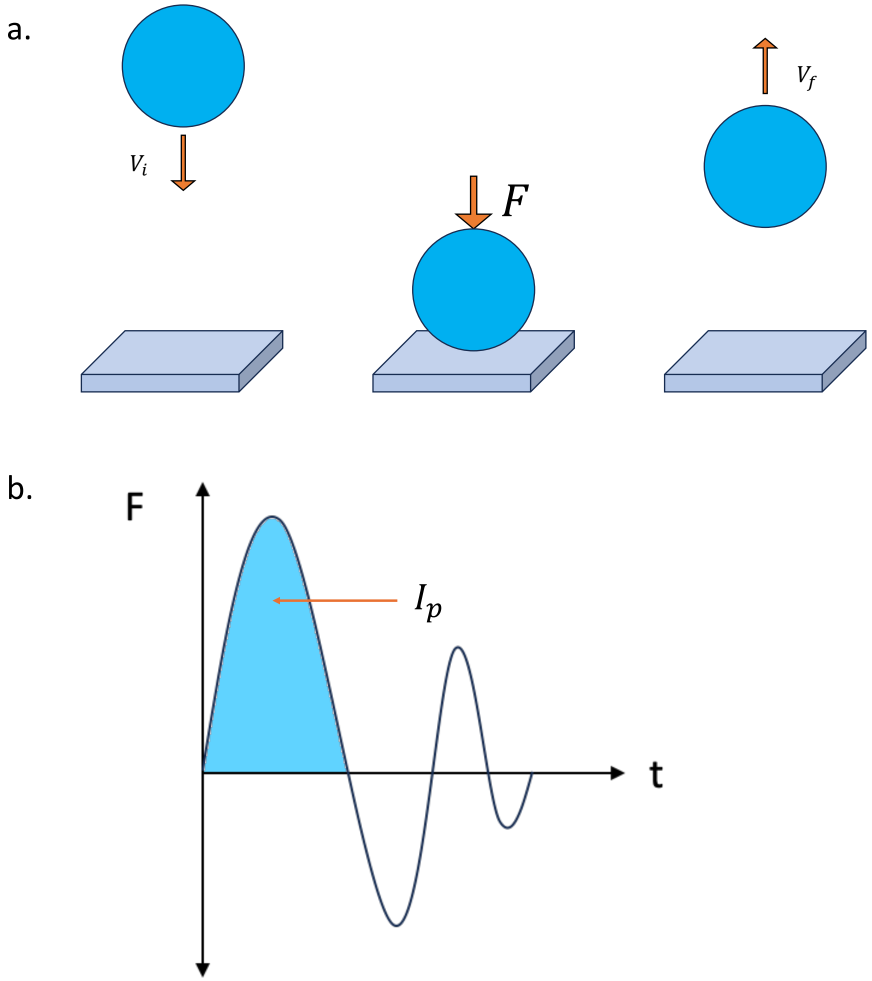

Figure 4.2. a. Diagram of impact of a ball dropping of the ground with initial velocity V_i before impact and velocity V_f after the impact. b. Impulse associated with impact represented by the area under the F vs t curve of the impact.

Force and time are inversely proportional during a collision if momentum is held constant. This means that increases in the time of impact (t), will cause the force (F) experienced to decrease proportionally. This concept is usually quantified through the impulse delivered during the impact. In our experiments the impulse can be calculated in two different ways.

Consider a ball with mass m falling with V_i velocity before impact and V_f after the impact. Impulse can be defined as,

$$I_v = \Delta P = mV_f - mV_i \tag{4.1}$$

Alternatively, in the same impact situation, the force(F) vs time(t) curve also allows impulse to be calculated:

$$I_p = \int \vec{F} dt \tag{4.2}$$

In principle, I_v=I_p, though the values may differ slightly due to different types of error influencing each calculation. I_p, for example, could suffer error with data that is not taken with small enough time steps to justify integration. Likewise, Iv may suffer from the determination of the points before and after collision being imprecise.

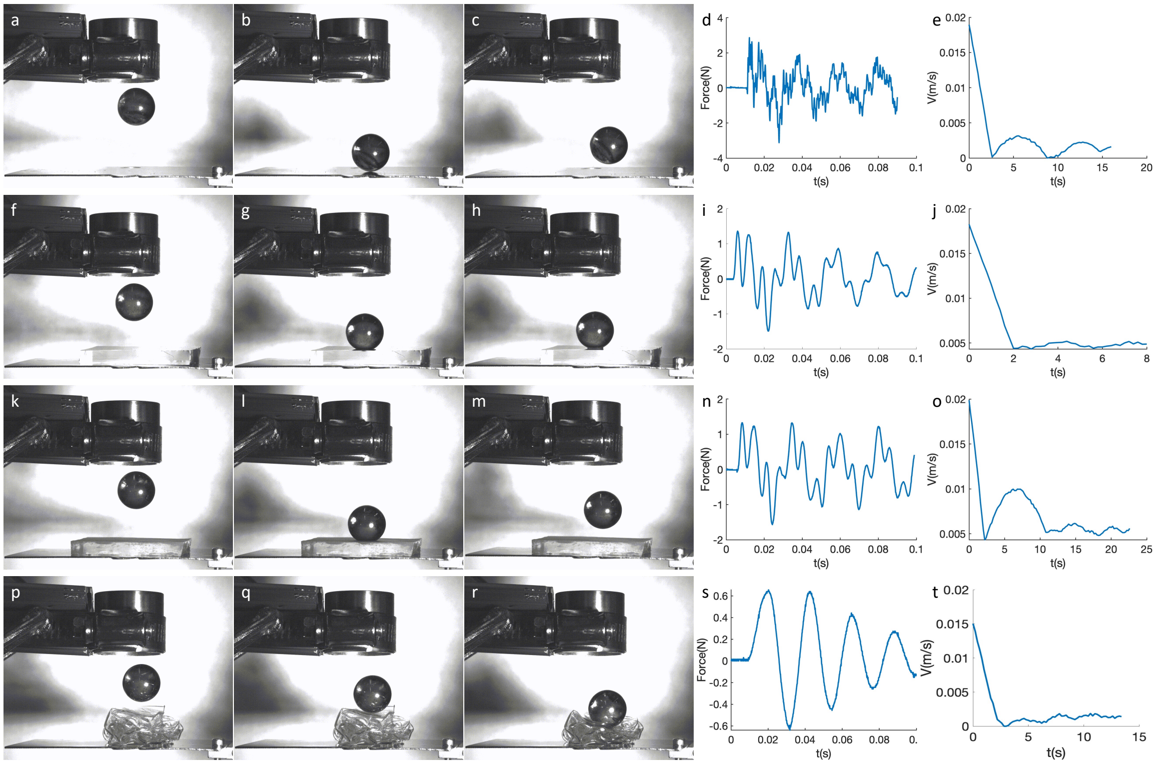

Figure 4.3. Experimental results. a,b, and c Representative of glass ball positions before , during and after impacts with metal cantilever where d and e are force vs time and velocity vs time curves. Other three rows are similar data for PDMS chunk, PDMS chunk with cornstarch and PDMS crumple

Figure 4.3 provides illustrative images captured by the high-speed camera before, during, and after impact events. The images reveal distinct post-impact behaviors, where in the glass ball impactor disengages from the metal cantilever and a cantilever bearing a polydimethylsiloxane (PDMS) chunk coated with cornstarch to remove the surface adhesion. Conversely, during impact with a sticky PDMS chunk and a sticky crumple, the glass ball impactor remains in contact with the material. Notably, the Force versus time (F vs t) plots exhibit varied energy absorption levels for these impact scenarios. The bare plate manifests diverse modes of vibrations and a relatively high peak force. In contrast, both sticky and non-sticky PDMS data exhibit fewer modes of vibration, resulting in much smoother curves, and show a reduced peak force compared with the bare plate. The force versus time curve for the crumple is much simpler, exciting only a single mode of oscillation and a much-diminished peak force value.

Figure 4.3e, j, o, and t depict displacement versus time graphs corresponding to impacts involving the bare plate, a 40:1 sticky PDMS chunk, a non-sticky PDMS chunk, and a 40:1 crumple, respectively. In the case of the bare plate, the ball exhibits a rebounding contrast with the scenario involving the sticky PDMS where the ball sinks into the soft PDMS and then becomes bound by adhesion. The non-sticky PDMS scenario reveals a higher rebound velocity, aligning with expectations for a typical elastic material. The impact with the sticky crumple also absorbs a substantial amount of energy. The direct observations of Figure 4.3 underscore the distinct energy absorption characteristics demonstrated by the various materials and configurations studied in this work. Surface adhesion clearly leads to increased energy absorption and complex geometry and internal adhesion leads to lower impact forces.

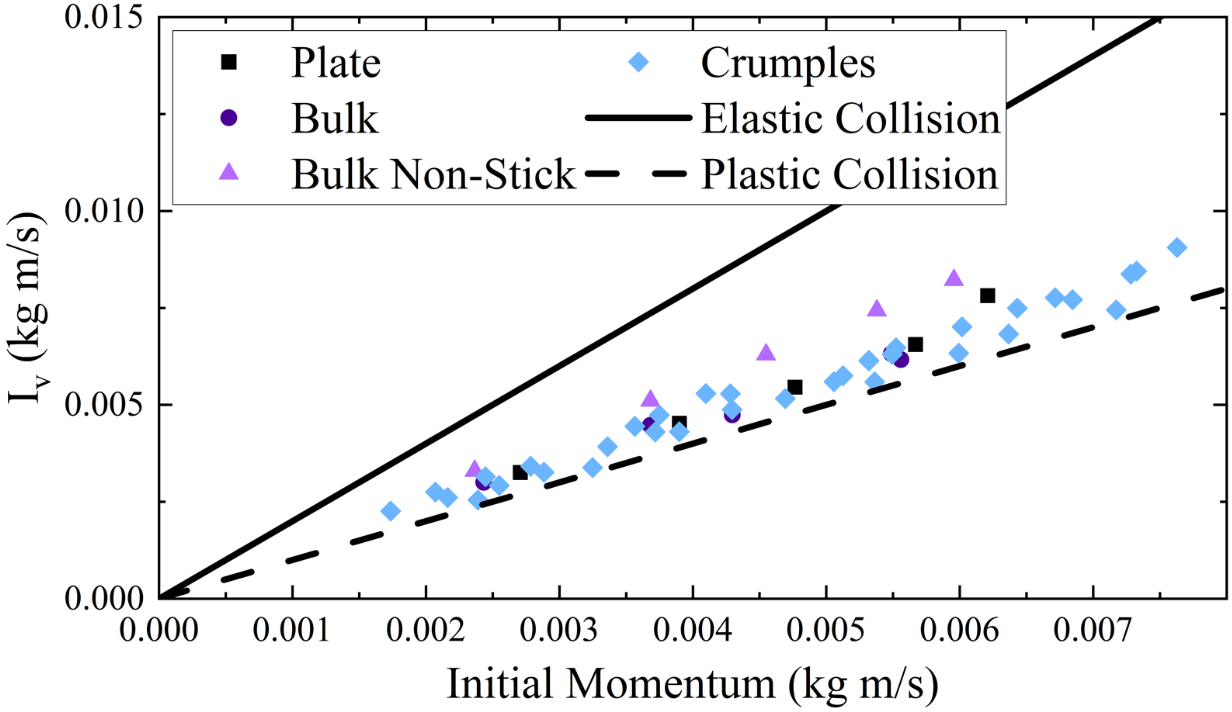

Figure 4.4. Impulse calculated by momentum change vs initial impactor momentum calculated from the slow-motion video analysis using the tracker software.

Collisions can be divided into two idealized situations. First, the impact may be purely elastic. In this case, $V_f = -V_i$ and thus IE=2mV. On the other hand, a perfectly plastic collision would see the complete absorption of momentum, thus $I_p = mV_i$. All data must lie between these two limits. Figure 4.4 shows the impulse calculated from the momentum change plotted against the initial momentum. The plot shows that all impulse data lie nearer to the plastic limit, though the crumples are the closest of the 4 experimental groups. The bulk non-stick elastomer sample shows the highest values of impulse, as one might expect given it lacks adhesion and is a highly elastic material.

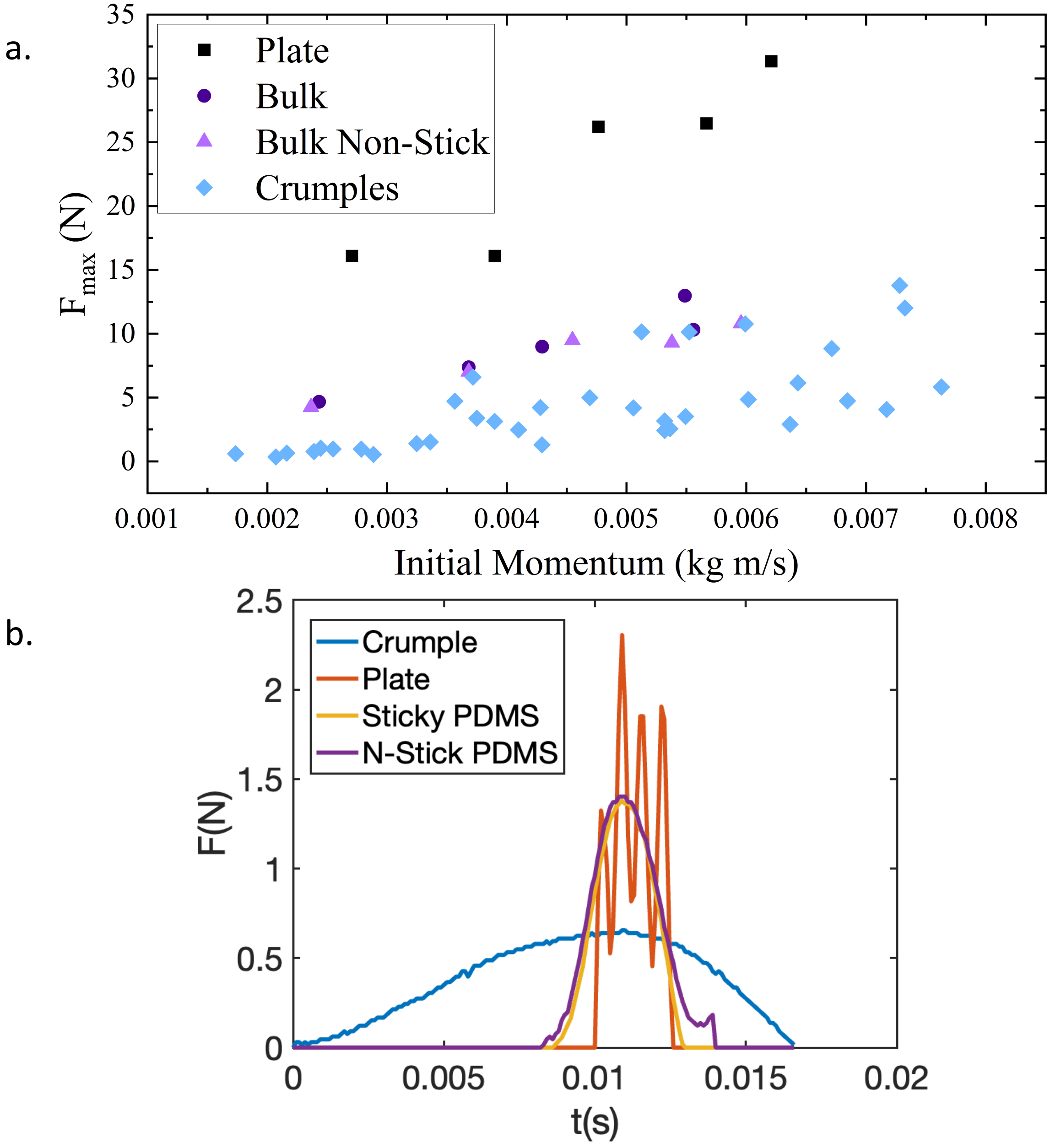

Figure 4.5. a.Peak forces of the data for plate, chunk, non-stick chunk and crumple. b.First peak of F vs t curves for plate, chunk, non-stick chunk and crumple plotted in same graph.

The peak force is one of the most important measures in terms of protection of a cargo, as peak force is most directly relatable to material failure. Figure 4.5 shows the peak force of impacts over a range of initial momentia. The plate exhibits the highest peak force values, while crumples demonstrate the lowest values. The peak force values for both bulk sticky and non-sticky PDMS samples are positioned intermediate to the plate and crumple data and fall within the same range. Notably, the full force curves presented in Figure 3 , show that both sticky and non-stick bulk PDMS samples show similar vibrational patterns, implying that the adhesive properties do not significantly contribute to internal processes after the delivery of energy. Figure 6b unequivocally illustrates that crumples effectively absorb impacts by mitigating peak intensities, reducing additional vibrational components and elongate the temporal extent of the peak.

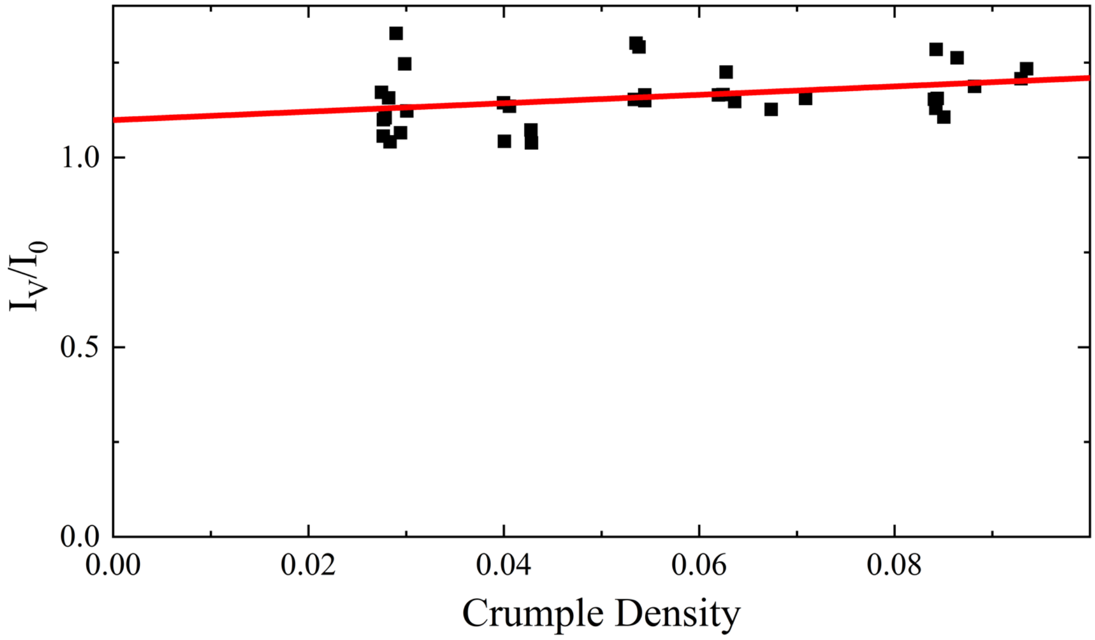

Figure 4.6. Density of crumples with a liner fit

The density of a crumple material will likely influence its performance(20; 157).A solid material will have a higher effective speed of sound compared to a lower density structure created from the same material. On the other hand, a low density structure will be much more easily deformed during impact which might lead to situations in which an impactor completely collapses the material ultimately transmits a higher impulse to the underlying layer. Figure 4.6 shows the change in impulse normalized by initial impulse as a function of crumple density. The plot shows a linear increase in normalized change in impulse as a function of crumple density (solid line is a fit with a slope of 1.1 ± 0.5 and an intercept of 1.1 ± .03). This is as one might expect, denser crumpled materials have less internal interfaces and less ability to absorb energy at the adhesive interfaces. It is interesting to note that extremely low density crumples show no signs of reduced impulse change, suggesting that lower density crumpled mater is desirable for impulse reducing applications.

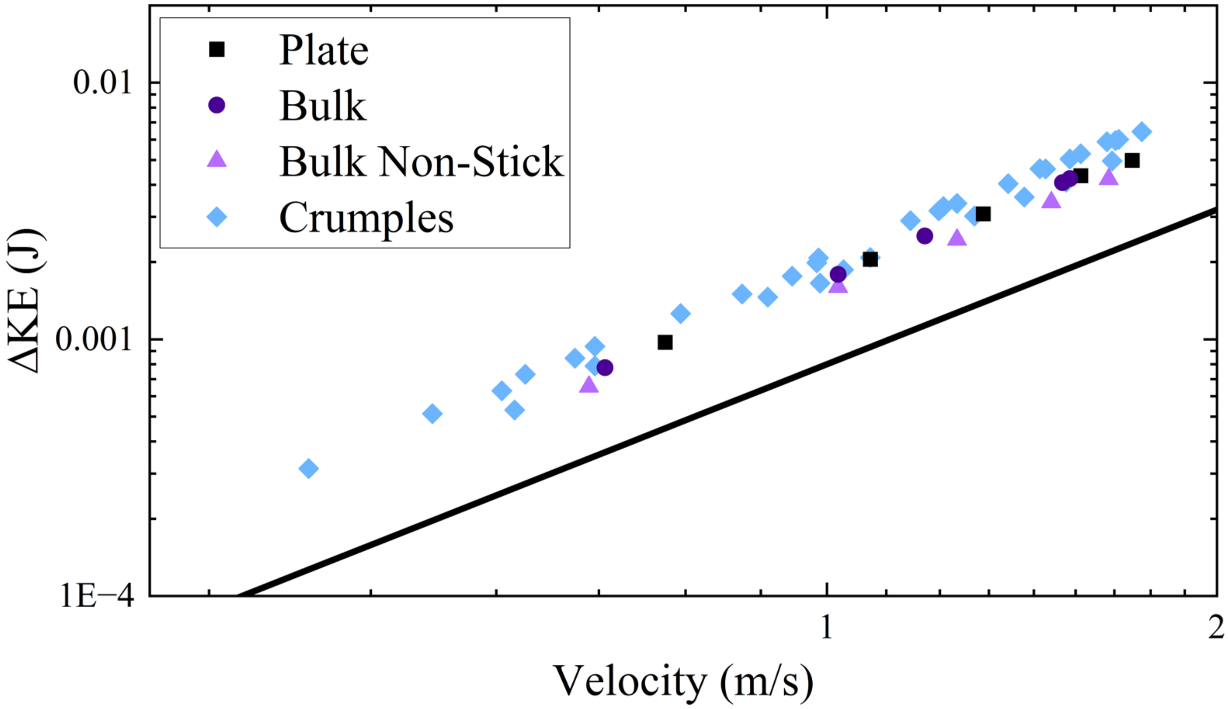

Figure 4.7. A graph of change in kinetic energy vs initial impactor velocity

Finally, we examine the energy absorbed by each material. Figure 4.7 shows the change in kinetic energy of the impactor as a function of initial velocity. Once again, we see better performance of the crumpled samples, as they absorb more energy than the other tested samples.

Similarly, the worst energy absorbing material is the non-stick bulk sample as it consistently shows the most elastic response. Notably, the energy absorption for all materials scales as a quadratic with initial velocity, hinting that the processes are dominated by viscous loss in the materials.

4.6. Conclusions

It is important to find alternative, inexpensive ways of packaging and protective layers to prevent damage due to impact. Widely available, inexpensive sticky crumple structures are a good substitute for some applications. Our results show that the impact absorption properties of crumples can be easily tuned to achieve this and other goals.

5. CONCLUSION

Thin films, characterized by their thickness being significantly smaller than their length and width, undergo transformations into 3D structures through phenomena like buckling and folding. Origami intertwines mathematics and ordered folding patterns, in contrast, crumples exhibit complex origami-like structures with disordered folding patterns, offering different mechanical behavior. Structural analysis reveals interesting basic features like bends, folds, D-cones, and ridges, is essential for understanding the rigidity of crumples and the mechanisms of origami.

In the first chapter of this dissertation, compression experiments and simulations were conducted on crumpled sheets with and without kirigami-like cut patterns. Different materials including PDMS, PC, and Paper were investigated. While PDMS samples showed no significant differences between cut and uncut sheets, plastic materials exhibited small changes in effective modulus when cut. CG-MD simulations of graphene sheets revealed similar behavior to plastic materials, with minor stiffness changes noted. Analysis of internal structure and stress state showed few significant changes in crumpled cut sheets compared to uncut ones. However notable alterations in the location and orientation of highly curved regions (creases) was noted. Line segment analysis indicated a distinct perpendicular orientation to cut edges, particularly in denser crumples. Overall, despite significant changes in crease patterns, the macroscopic compressive behavior remained largely unaffected, suggesting that long-range structures like ridges and folds do not significantly impact compression modulus, aligning with the idea of folds as loci of point-like defects where the number of defects matters more than their orientation.

Chapter two delves into the exploration of reversible adhesives through origami-based design, aiming to address challenges in temporary attachment and detachment across various applications. By employing origami devices with two stable states, the study investigates mechanically switchable adhesive devices, revealing varying switching ratios among different origami patterns. Notably, while the Kresling pattern achieved a ratio of 1.5 and the waterbomb pattern 3, the Ron Resch pattern exhibited a remarkable maximum ratio of 50, though was marked typically around 6 due to plasticity in origami creases. increased crease aging reduced the switching ratio, and ratios generally increased with motor speed and larger contact areas. The functional success of these devices underscores the efficacy of origami-based design for switchable adhesive development, with the potential for integration into soft robotic systems. Future research may explore augmented origami devices and the combination of modern adhesive design techniques with origami principles for further innovation, offering increased control and adaptability in adhesive performance across a wide range of applications.

The third chapter explores the impact mitigation properties of the sticky crumpled matter. It is important to find alternative, inexpensive ways of packaging and protective layers to prevent damage due to impact. Widely available, inexpensive sticky crumple structures are a good substitute for some applications. Our results show that the impact absorption properties of crumples falls closer to plastic limits and can be easily tuned to achieve biomedical and other packaging goals.

In conclusion, this thesis has investigated 3D structures made out of 2D polymer thin films and how these structures mechanically respond to compression, pull-off, and impacts with several other properties involving adhesion and kirigami patterns. We investigated complex crumple 3D structures as well as origami structures. Through compression tests, pull-off tests, and impact tests we found that long-range structural features, such as ridges, folds, and bends, play a minimal role in the compressibility of crumpled sheets, challenging previous assumptions. This finding has significant implications for applications like packaging. In the second study, origami shapes were investigated to develop switchable adhesive devices, inspired by nature's adhesion mechanisms. Through origami design methods, geometries transitioning between stiff and easily peeled configurations were created, showcasing moderate switching ratios and potential applications in temporary adhesive attachments. The final study focused on utilizing sticky crumpled matter for impact mitigation, leveraging the rigidity and energy-absorbing properties of crumples. Experimental observations demonstrated the effectiveness of sticky crumpled matter as a protective layer, highlighting its potential as a replacement for engineered form structures. Overall, this research advances our understanding of thin film mechanics and offers novel insights into the development of versatile, functional materials with applications across various domains, from packaging to impact mitigation.

REFERENCES

[1] W. D. Nix, "Mechanical properties of thin films," *Metallurgical transactions A*, vol. 20, pp. 2217–2245, 1989.

[2] Z. Huang, W. Hong, and Z. Suo, "Evolution of wrinkles in hard films on soft substrates," *Physical Review E*, vol. 70, no. 3, p. 030601, 2004.

[3] Z. Bai, Y. Su, and B. Ji, "Buckling behaviors of staggered nanostructure of biological materials," *Journal of Applied Mechanics*, vol. 83, no. 3, p. 031011, 2016.

[4] S. Dutta and S. K. Pati, "Novel properties of graphene nanoribbons: a review," *Journal of Materials Chemistry*, vol. 20, no. 38, pp. 8207–8223, 2010.

[5] R. L. Antoniou Kourounioti, L. R. Band, J. A. Fozard, A. Hampstead, A. Lovrics, E. Moyroud, S. Vignolini, J. R. King, O. E. Jensen, and B. J. Glover, "Buckling as an origin of ordered cuticular patterns in flower petals," *Journal of the Royal Society Interface*, vol. 10, no. 80, p. 20120847, 2013.

[6] D. L. Blair and A. Kudrolli, "Geometry of crumpled paper," *Phys. Rev. Lett.*, vol. 94, p. 166107, 2005.

[7] A. K. Schulz, M. Boyle, C. Boyle, S. Sordilla, C. Rincon, S. Hooper, C. Aubuchon, J. S. Reidenberg, C. Higgins, and D. L. Hu, "Skin wrinkles and folds enable asymmetric stretch in the elephant trunk," *Proceedings of the National Academy of Sciences*, vol. 119, no. 31, p. e2122563119, 2022.

[8] N. Bowden, S. Brittain, A. G. Evans, J. W. Hutchinson, and G. M. Whitesides, "Spontaneous formation of ordered structures in thin films of metals supported on an elastomeric polymer," *nature*, vol. 393, no. 6681, pp. 146–149, 1998.

[9] E. A. Peraza-Hernandez, D. J. Hartl, R. J. Malak Jr, and D. C. Lagoudas, “Origami-inspired active structures: a synthesis and review,” *Smart Materials and Structures*, vol. 23, no. 9, p. 094001, 2014.

[10] C. Wang, Y. Liu, L. Lan, and H. Tan, “Graphene wrinkling: formation, evolution and collapse,” *Nanoscale*, vol. 5, no. 10, pp. 4454–4461, 2013.

[11] H. Shima, “Buckling of carbon nanotubes: a state of the art review,” *Materials*, vol. 5, no. 1, pp. 47–84, 2011.

[12] F. Haas and R. J. Wootton, “Two basic mechanisms in insect wing folding,” *Proceedings of the Royal Society of London. Series B: Biological Sciences*, vol. 263, no. 1377, pp. 1651–1658, 1996.

[13] V. V. Beloussov, “The origin of folding in the earth’s crust,” *Journal of Geophysical Research*, vol. 66, no. 7, pp. 2241–2254, 1961.

[14] G. Newkirk Jr and D. G. Wentzel, “Rigidity-independent propagation of cosmic rays in the solar corona,” *Journal of Geophysical Research: Space Physics*, vol. 83, no. A5, pp. 2009–2015, 1978.

[15] M. K. Blees, A. W. Barnard, P. A. Rose, S. P. Roberts, K. L. McGill, P. Y. Huang, A. R. Ruyack, J. W. Kevek, B. Kobrin, D. A. Muller, *et al.*, “Graphene kirigami,” *Nature*, vol. 524, no. 7564, pp. 204–207, 2015.

[16] S. Li, J. J. Stampfli, H. J. Xu, E. Malkin, E. V. Diaz, D. Rus, and R. J. Wood, “A vacuum-driven origami “magic-ball” soft gripper,” in *2019 International Conference on Robotics and Automation (ICRA)*, pp. 7401–7408, IEEE, 2019.

[17] J. P. Gardner, J. C. Mather, M. Clampin, R. Doyon, M. A. Greenhouse, H. B. Hammel, J. B. Hutchings, P. Jakobsen, S. J. Lilly, K. S. Long, *et al.*, “The james webb space telescope,” *Space Science Reviews*, vol. 123, pp. 485–606, 2006.

[18] K. Kuribayashi, K. Tsuchiya, Z. You, D. Tomus, M. Umemoto, T. Ito, and M. Sasaki, "Self-deployable origami stent grafts as a biomedical application of ni-rich tini shape memory alloy foil," *Materials Science and Engineering: A*, vol. 419, no. 1-2, pp. 131–137, 2006.

[19] K. Matan, R. B. Williams, T. A. Witten, and S. R. Nagel, "Crumpling a thin sheet," *Phys. Rev. Lett.*, vol. 88, p. 076101, 2002.

[20] A. B. Croll, T. Twohig, and T. Elder, "The compressive strength of crumpled matter," *Nature communications*, vol. 10, no. 1, pp. 1–8, 2019.

[21] A. Lobkovsky, S. Gentges, H. Li, D. Morse, and T. A. Witten, "Scaling properties of stretching ridges in a crumpled elastic sheet," *Science*, vol. 270, no. 5241, pp. 1482–1485, 1995.

[22] T. Witten and H. Li, "Asymptotic shape of a fullerene ball," *Europhysics Letters*, vol. 23, no. 1, p. 51, 1993.

[23] A. E. Lobkovsky and T. Witten, "Properties of ridges in elastic membranes," *Physical Review E*, vol. 55, no. 2, p. 1577, 1997.

[24] K. Matan and R. B. Williams, "Thomas a. witten, and sidney r. nagel. crumpling a thin sheet," *Physical Review Letters*, vol. 88, pp. 7–10, 2002.

[25] S. Deboeuf, E. Katzav, A. Boudaoud, D. Bonn, and M. Adda-Bedia, "Comparative study of crumpling and folding of thin sheets," *Physical review letters*, vol. 110, no. 10, p. 104301, 2013.

[26] C. Reid and W. Owen, *Deformation Geometry for Materials Scientists: International Series on Materials Science and Technology*. International series on materials science and technology, Elsevier Science, 2016.

[27] G. Mavko, T. Mukerji, and J. Dvorkin, *The rock physics handbook*. Cambridge university press, 2020.

[28] D. Askeland, F. Haddleton, P. Green, and H. Robertson, *The Science and Engineering of Materials*. Springer US, 2013.

[29] W. Callister and D. Rethwisch, *Fundamentals of Materials Science and Engineering: An Integrated Approach*. Wiley, 2012.

[30] P. William F. Smith and P. Javad Hashemi, *Foundations of Materials Science and Engineering*. McGraw-Hill series in materials science, McGraw-Hill Education, 2010.

[31] G. Scott, *Polymers and the Environment*. RSC paperbacks, Royal Society of Chemistry, 1999.

[32] K. Efimenko, W. E. Wallace, and J. Genzer, "Surface modification of sylgard-184 poly(dimethyl siloxane) networks by ultraviolet and ultraviolet/ozone treatment," *Journal of Colloid and Interface Science*, vol. 254, no. 2, pp. 306–315, 2002.

[33] E. Sollier, C. Murray, P. Maoddi, and D. Di Carlo, "Rapid prototyping polymers for microfluidic devices and high pressure injections," *Lab on a chip*, vol. 11, p. 3752—3765, November 2011.

[34] J. C. McDonald and G. M. Whitesides, "Poly(dimethylsiloxane) as a material for fabricating microfluidic devices," *Accounts of Chemical Research*, vol. 35, no. 7, pp. 491–499, 2002. PMID: 12118988.

[35] G. M. Whitesides, "The origins and the future of microfluidics," *Nature*, vol. 442, pp. 368–373, Jul 2006.

[36] D. Armani, C. Liu, and N. Aluru, "Re-configurable fluid circuits by pdms elastomer micromachining," in *Technical Digest. IEEE International MEMS 99 Conference. Twelfth IEEE International Conference on Micro Electro Mechanical Systems (Cat. No.99CH36291)*, pp. 222–227, 1999.

[37] F. Schneider, J. Draheim, R. Kamberger, and U. Wallrabe, “Process and material properties of polydimethylsiloxane (pdms) for optical mems,” *Sensors and Actuators A: Physical*, vol. 151, no. 2, pp. 95–99, 2009.

[38] Y. Xia and G. M. Whitesides, “Soft lithography,” *Annual Review of Materials Science*, vol. 28, no. 1, pp. 153–184, 1998.

[39] I. D. Johnston, D. K. McCluskey, C. K. L. Tan, and M. C. Tracey, “Mechanical characterization of bulk sylgard 184 for microfluidics and microengineering,” *Journal of Micromechanics and Microengineering*, vol. 24, p. 035017, feb 2014.

[40] T. K. Kim, J. K. Kim, and O. C. Jeong, “Measurement of nonlinear mechanical properties of pdms elastomer,” *Microelectronic Engineering*, vol. 88, no. 8, pp. 1982–1985, 2011. Proceedings of the 36th International Conference on Micro- and Nano-Engineering (MNE).

[41] T. Hanada, T. Negishi, I. Shiroishi, and T. Shiro, “Plastic substrate with gas barrier layer and transparent conductive oxide thin film for flexible displays,” *Thin Solid Films*, vol. 518, no. 11, pp. 3089–3092, 2010. Transparent Oxides for Electronics and Optiocs (TOEO-6).

[42] T. Elder, D. Rozairo, and A. B. Croll, “Origami inspired mechanics: Measuring modulus and force recovery with bent polymer films,” *Macromolecules*, vol. 52, pp. 690–699, Jan 2019.

[43] A. Flory and G. B. McKenna, “Physical aging behavior of the normal force and torque in polymer glasses,” *Mechanics of Time-Dependent Materials*, vol. 14, pp. 347–357, Nov 2010.

[44] J. M. Hutchinson, S. Smith, B. Horne, and G. M. Gourlay, "Physical aging of polycarbonate: Enthalpy relaxation, creep response, and yielding behavior," *Macromolecules*, vol. 32, pp. 5046–5061, Jul 1999.

[45] J. M. Hutchinson, A. B. Tong, and Z. Jiang, "Aging of polycarbonate studied by temperature modulated differential scanning calorimetry," *Thermochimica Acta*, vol. 335, no. 1, pp. 27–42, 1999.

[46] M. J. Mindel and N. Brown, "Creep and recovery of polycarbonate," *Journal of Materials Science*, vol. 8, pp. 863–870, Jun 1973.

[47] V. A. Soloukhin, J. C. M. Brokken-Zijp, O. L. J. van Asselen, and G. de With, "Physical aging of polycarbonate: elastic modulus, hardness, creep, endothermic peak, molecular weight distribution, and infrared data," *Macromolecules*, vol. 36, pp. 7585–7597, Oct 2003.

[48] A. J. Meuler, J. D. Smith, K. K. Varanasi, J. M. Mabry, G. H. McKinley, and R. E. Cohen, "Relationships between water wettability and ice adhesion," *ACS applied materials & interfaces*, vol. 2, no. 11, pp. 3100–3110, 2010.

[49] K. Autumn and N. Gravish, "Gecko adhesion: evolutionary nanotechnology," *Philosophical Transactions of the Royal Society A: Mathematical, Physical and Engineering Sciences*, vol. 366, no. 1870, pp. 1575–1590, 2008.

[50] K. Autumn, Y. A. Liang, S. T. Hsieh, W. Zesch, W. P. Chan, T. W. Kenny, R. Fearing, and R. J. Full, "Adhesive force of a single gecko foot-hair," *Nature*, vol. 405, no. 6787, pp. 681–685, 2000.

[51] K. Autumn, P. H. Niewiarowski, and J. B. Puthoff, "Gecko adhesion as a model system for integrative biology, interdisciplinary science, and bioinspired engineering," *Annual Review of Ecology, Evolution, and Systematics*, vol. 45, pp. 445–470, 2014.

[52] B. Chen, P. Wu, and H. Gao, "Hierarchical modelling of attachment and detachment mechanisms of gecko toe adhesion," *Proceedings of the Royal Society A: Mathematical, Physical and Engineering Sciences*, vol. 464, no. 2094, pp. 1639–1652, 2008.

[53] H. E. Jeong, J.-K. Lee, H. N. Kim, S. H. Moon, and K. Y. Suh, "A nontransferring dry adhesive with hierarchical polymer nanohairs," *Proceedings of the National Academy of Sciences*, vol. 106, no. 14, pp. 5639–5644, 2009.

[54] L. Qu, L. Dai, M. Stone, Z. Xia, and Z. L. Wang, "Carbon nanotube arrays with strong shear binding-on and easy normal lifting-off," *Science*, vol. 322, no. 5899, pp. 238–242, 2008.

[55] C. Greiner, E. Arzt, and A. Del Campo, "Hierarchical gecko-like adhesives," *Advanced Materials*, vol. 21, no. 4, pp. 479–482, 2009.

[56] M. P. Murphy, S. Kim, and M. Sitti, "Enhanced adhesion by gecko-inspired hierarchical fibrillar adhesives," *ACS applied materials & interfaces*, vol. 1, no. 4, pp. 849–855, 2009.

[57] H. Lee, B. P. Lee, and P. B. Messersmith, "A reversible wet/dry adhesive inspired by mussels and geckos," *Nature*, vol. 448, no. 7151, pp. 338–341, 2007.

[58] J. M. Bullock, P. Drechsler, and W. Federle, "Comparison of smooth and hairy attachment pads in insects: friction, adhesion and mechanisms for direction-dependence," *Journal of Experimental Biology*, vol. 211, no. 20, pp. 3333–3343, 2008.

[59] G. Huber, S. N. Gorb, R. Spolenak, and E. Arzt, "Resolving the nanoscale adhesion of individual gecko spatulae by atomic force microscopy," *Biology letters*, vol. 1, no. 1, pp. 2–4, 2005.

[60] M. D. Bartlett, A. B. Croll, D. R. King, B. M. Paret, D. J. Irschick, and A. J. Crosby, "Looking beyond fibrillar features to scale gecko-like adhesion," *Advanced Materials*, vol. 24, no. 8, pp. 1078–1083, 2012.

[61] M. D. Bartlett, A. B. Croll, and A. J. Crosby, “Designing bio-inspired adhesives for shear loading: from simple structures to complex patterns,” *Advanced Functional Materials*, vol. 22, no. 23, pp. 4985–4992, 2012.

[62] J. O. Wolff and S. N. Gorb, “Radial arrangement of janus-like setae permits friction control in spiders,” *Scientific reports*, vol. 3, no. 1, p. 1101, 2013.

[63] D. R. King, M. D. Bartlett, C. A. Gilman, D. J. Irschick, and A. J. Crosby, “Creating gecko-like adhesives for “real world” surfaces,” *Advanced Materials*, vol. 26, no. 25, pp. 4345–4351, 2014.

[64] A. De Morais, A. Pereira, J. Teixeira, and N. Cavaleiro, “Strength of epoxy adhesive-bonded stainless-steel joints,” *International journal of adhesion and adhesives*, vol. 27, no. 8, pp. 679–686, 2007.

[65] D. Maugis and M. Barquins, “Fracture mechanics and adherence of viscoelastic solids,” in *Adhesion and adsorption of polymers*, pp. 203–277, Springer, 1980.

[66] K. Kendall, “The adhesion and surface energy of elastic solids,” *Journal of Physics D: Applied Physics*, vol. 4, no. 8, p. 1186, 1971.

[67] E. V. Quintana, T. Barclay, W. J. Borucki, J. F. Rowe, and J. E. Chambers, “The frequency of giant impacts on earth-like worlds,” *The Astrophysical Journal*, vol. 821, no. 2, p. 126, 2016.

[68] J. Knaster, A. Moeslang, and T. Muroga, “Materials research for fusion,” *Nature Physics*, vol. 12, no. 5, pp. 424–434, 2016.

[69] K. Joszko, W. Wolański, W. Burkacki, S. Suchoń, K. Zielonka, A. Muszyński, and M. Gzik, “Biomechanical analysis of injuries of rally driver with head supporting device,” *Acta of bioengineering and biomechanics*, vol. 18, no. 4, pp. 159–169, 2016.

[70] G. Yeh, R. Hosemann, J. Loboda-Čačković, and H. Čačković, "Annealing effects of polymers and their underlying molecular mechanisms," *Polymer*, vol. 17, no. 4, pp. 309–318, 1976.

[71] Y. Tanabe, G. Strobl, and E. Fischer, "Surface melting in melt-crystallized linear polyethylene," *Polymer*, vol. 27, no. 8, pp. 1147–1153, 1986.

[72] E. W. Fischer, "Effect of annealing and temperature on the morphological structure of polymers," *Pure and Applied Chemistry*, vol. 31, no. 1-2, pp. 113–132, 1972.

[73] "Cricut." https://cricut.com/en/. Accessed: 2023-10-31.

[74] W. M. Jayawardana, Y. Liao, Z. Li, W. Xia, and A. B. Croll, "Crumpled kirigami," *Soft Matter*, vol. 19, no. 6, pp. 1081–1091, 2023.

[75] M. D. Bartlett, S. W. Case, A. J. Kinloch, and D. A. Dillard, "Peel tests for quantifying adhesion and toughness: A review," *Progress in Materials Science*, p. 101086, 2023.

[76] C. A. Schneider, W. S. Rasband, and K. W. Eliceiri, "Nih image to imagej: 25 years of image analysis," *Nature methods*, vol. 9, no. 7, pp. 671–675, 2012.

[77] "Imagej." https://imagej.net/. Accessed: 2023-10-31.

[78] P. K. Purohit, J. Kondev, and R. Phillips, "Mechanics of dna packaging in viruses," *Proceedings of the National Academy of Sciences*, vol. 100, no. 6, pp. 3173–3178, 2003.

[79] E. Katzav, M. Adda-Bedia, and A. Boudaoud, "A statistical approach to close packing of elastic rods and to dna packaging in viral capsids," *Proceedings of the National Academy of Sciences*, vol. 103, no. 50, pp. 18900–18904, 2006.

[80] H. Kobayashi, B. Kresling, and J. F. V. Vincent, "The geometry of unfolding tree leaves," *Proc. R. Soc. Lond*, vol. B, no. 256, pp. 147–154, 1998.

[81] B. Mota and S. Herculano-Houzel, "Cortical folding scales universally with surface area and thickness, not number of neurons," *Science*, vol. 349, no. 6243, pp. 74–77, 2015.

[82] J. Plescia and M. Golombek, "Origin of planetary wrinkle ridges based on the study of terrestrial analogs," *Geological Society of America Bulletin*, vol. 97, no. 11, pp. 1289–1299, 1986.

[83] M. F. Ashby, "The properties of foams and lattices," *Philosophical Transactions of the Royal Society A: Mathematical, Physical and Engineering Sciences*, vol. 364, no. 1838, pp. 15–30, 2006.

[84] N. P. D. Luca, O. M. Reyes, and P. M. Jacques, "Inflatable, cushioning, bubble wrap product having multiple, interconnected, bubble structures," 2000. US Patent US6410119B1.

[85] O. Gottesman, J. Andrejevic, C. H. Rycroft, and S. M. Rubinstein, "A state variable for crumpled thin sheets," *Comm. Phys.*, vol. 1, p. 70, 2018.

[86] J. Andrejevic, L. M. Lee, S. M. Rubinstein, and C. H. Rycroft, "A model for the fragmentation kinetics of crumpled thin sheets," *Nat. Commun.*, vol. 12, p. 1470, 2021.

[87] T. Mora and A. Boudaoud, "Thin elastic plates: On the core of developable cones," *Europhysics Letters (EPL)*, vol. 59, pp. 41–47, jul 2002.

[88] P. Wang-Iverson, R. J. Lang, and Y. Mark, *Origami 5: Fifth International Meeting of Origami Science, Mathematics, and Education*. CRC Press, 2011.

[89] Y. Liu, J. Genzer, and M. D. Dickey, "“2d or not 2d”: Shape-programming polymer sheets," *Progress in Polymer Science*, vol. 52, pp. 79–106, 2016.

[90] Y. Liu, B. Shaw, M. D. Dickey, and J. Genzer, "Sequential self-folding of polymer sheets," *Science Advances*, vol. 3, no. 3, p. e1602417, 2017.

[91] J. Tao, H. Khosravi, V. Deshpande, and S. Li, "Engineering by cuts: How kirigami principle enables unique mechanical properties and functionalities," *Advanced Science*, vol. n/a, no. n/a, p. 2204733, 2022.

[92] G. A. Vliegenthart and G. Gompper, "Forced crumpling of self-avoiding elastic sheets," *Nat. Mater.*, vol. 5, pp. 216–221, 2006.

[93] T. Tallinen, J. Åström, and J. Timonen, "The effect of plasticity in crumpling of thin sheets," *Nat. Mater.*, vol. 8, pp. 25–29, 2009.

[94] M. Habibi, M. Adda-Bedia, and D. Bonn, "Effect of the material properties on the crumpling of a thin sheet," *Soft matter*, vol. 13, no. 22, pp. 4029–4034, 2017.

[95] A. B. Croll, Y. Liao, Z. Li, W. M. Jayawardana, T. Elder, and W. Xia, "Sticky crumpled matter," *Matter*, pp. 1792–1805, 2022.

[96] M. J. Mirzaali, M. Habibi, S. Janbaz, L. Vergani, and A. A. Zadpoor, "Crumpling-based soft metamaterials: the effects of sheet pore size and porosity," *Scientific Reports*, vol. 7, p. 13028, 2017.

[97] I. Giordanelli, M. Mendoza, J. S. Andrade Jr, M. Gomes, and H. J. Herrmann, "Crumpling damaged graphene," *Scientific reports*, vol. 6, no. 1, pp. 1–6, 2016.

[98] S. W. Cranford and M. J. Buehler, "Packing efficiency and accessible surface area of crumpled graphene," *Physical Review B*, vol. 84, no. 20, p. 205451, 2011.

[99] Y. Liao, Z. Li, W. Nie, and W. Xia, "Effect of reconstructed vacancy defects on the crumpling behavior of graphene sheets," *Forces in Mechanics*, vol. 6, p. 100057, 2022.

[100] C. Bauwens-Crowet, J. C. Bauwens, and G. Homès, "Tensile yield-stress behavior of glassy polymers," *Journal of Polymer Science Part A-2: Polymer Physics*, vol. 7, no. 4, pp. 735–742, 1969.

[101] L. Ruiz, W. Xia, Z. Meng, and S. Keten, "A coarse-grained model for the mechanical behavior of multi-layer graphene," *Carbon*, vol. 82, pp. 103–115, 2015.

[102] X. Ma, M. R. Zachariah, and C. D. Zangmeister, "Crumpled nanopaper from graphene oxide," *Nano letters*, vol. 12, no. 1, pp. 486–489, 2012.

[103] Y. Liao, Z. Li, W. Xia, *et al.*, "Size-dependent structural behaviors of crumpled graphene sheets," *Carbon*, vol. 174, pp. 148–157, 2021.

[104] Y. Liao, Z. Li, S. Ghazanfari, Fatima, A. B. Croll, and W. Xia, "Understanding the role of self-adhesion in crumpling behaviors of sheet macromolecules," *Langmuir*, vol. 37, no. 28, pp. 8627–8637, 2021.

[105] S. Plimpton, "Fast parallel algorithms for short-range molecular dynamics," *Journal of computational physics*, vol. 117, no. 1, pp. 1–19, 1995.

[106] A. Cambou and N. Menon, "Three-dimensional structure of a sheet crumpled into a ball," *Proc. Nat. Acad. Sci.*, vol. 108, pp. 14741–14745, 2011.

[107] W. M. A. Jayawardana, T. Elder, T. Twohig, and A. B. Croll, "Switchable origami adhesives," *Soft Matter*, 2024.

[108] B. KRESLING, "Natural twist buckling in shells: from the hawkmoth's bellows to the deployable kresling-pattern and cylindrical miura-ori," *Proceedings of the 6th International Conference on Computation of Shell and Spatial Structures-IASS-IACM 2008:"Spanning Nano to Mega"*, pp. 1–4, 2008.

[109] N. Kidambi and K. Wang, "Dynamics of kresling origami deployment," *Physical Review E*, vol. 101, no. 6, p. 063003, 2020.

[110] P. Bhovad, J. Kaufmann, and S. Li, “Peristaltic locomotion without digital controllers: Exploiting multi-stability in origami to coordinate robotic motion,” *Extreme Mechanics Letters*, vol. 32, p. 100552, 2019.

[111] Y. Chen, H. Feng, J. Ma, R. Peng, and Z. You, “Symmetric waterbomb origami,” *Proceedings of the Royal Society A: Mathematical, Physical and Engineering Sciences*, vol. 472, no. 2190, p. 20150846, 2016.

[112] R. D. Resch, “The topological design of sculptural and architectural systems,” in *Proceedings of the June 4-8, 1973, national computer conference and exposition*, pp. 643–650, 1973.

[113] A. B. Croll, N. Hosseini, and M. D. Bartlett, “Switchable adhesives for multifunctional interfaces,” *Advanced Materials Technologies*, vol. 4, no. 8, p. 1900193, 2019.

[114] M. D. Bartlett, S. W. Case, A. J. Kinloch, and D. A. Dillard, “Peel tests for quantifying adhesion and toughness: A review,” *Progress in Materials Science*, vol. 137, p. 101086, 2023.

[115] D.-G. Hwang, K. Trent, and M. D. Bartlett, “Kirigami-inspired structures for smart adhesion,” *ACS Appl. Mater. Interfaces*, vol. 10, pp. 6747–6754, 2018.

[116] A. B. M. T. Haque, D. Hwang, and M. D. Bartlett, “Graded kirigami composites for programmed strain distributions,” *Advanced Materials Technologies*, vol. 7, no. 7, p. 2101241, 2022.

[117] A. Rafsanjani, Y. Zhang, B. Liu, S. M. Rubinstein, and K. Bertoldi, “Kirigami skins make a simple soft actuator crawl,” *Science Robotics*, vol. 3, no. 15, p. eaar7555, 2018.

[118] D.-G. Hwang, C. Lee, X. Yang, J. M. Pérez-González, J. Finnegan, B. Lee, E. J. Markvicka, R. Long, and M. D. Bartlett, “Metamaterial adhesives for programmable adhesion through reverse crack propagation,” *Nature Materials*, vol. 22, pp. 1030–1038, 2023.

[119] R. Spolenak, S. Gorb, H. Gao, and E. Arzt, “Effects of contact shape on the scaling of biological attachments,” *Proceedings of the Royal Society A: Mathematical, Physical and Engineering Sciences*, vol. 461, no. 2054, pp. 305–319, 2005.

[120] G. Wan, Y. Tang, K. T. Turner, T. Zhang, and W. Shan, “Tunable dry adhesion of soft hollow pillars through sidewall buckling under low pressure,” *Advanced Functional Materials*, vol. 33, no. 2, p. 2209905, 2023.

[121] E. Arzt, S. Gorb, and R. Spolenak, “From micro to nano contacts in biological attachment devices,” *Proceedings of the National Academy of Sciences*, vol. 100, no. 19, pp. 10603–10606, 2003.

[122] S. N. Gorb, “Uncovering insect stickiness: structure and properties of hairy attachment devices,” *American Entomologist*, vol. 51, no. 1, pp. 31–35, 2005.

[123] T. Jules, A. Reid, K. E. Daniels, M. Mungan, and F. Lechenault, “Delicate memory structure of origami switches,” *Physical Review Research*, vol. 4, no. 1, p. 013128, 2022.

[124] H. Tian, H. Liu, J. Shao, S. Li, X. Li, and X. Chen, “An electrically active gecko-effect soft gripper under a low voltage by mimicking gecko’s adhesive structures and toe muscles,” *Soft Matter*, vol. 16, pp. 5599–5608, 2020.

[125] L. H. Donnell, “Stability of thin-walled tubes under torsion,” tech. rep., National Advisory Committee for Aeronotics, 1935.

[126] S. Guest and S. Pellegrino, “The folding of triangulated cylinders, part i: Geometric considerations,” *J. Appl. Mech.*, vol. 61, pp. 773–777, 1994.

[127] S. Guest and S. Pellegrino, “The folding of triangulated cylinders, part ii: The folding process,” *J. Appl. Mech.*, vol. 61, pp. 778–783, 1994.

[128] S. Guest and S. Pellegrino, “The folding of triangulated cylinders, part iii: Experiments,” *J. Appl. Mech.*, vol. 63, pp. 77–83, 1996.

[129] H.-Y. Hwang, “Effects of perforated crease line design on mechanical behaviors of origami structures,” *International Journal of Solids and Structures*, vol. 230, p. 111158, 2021.

[130] K. R. VanDonselaar, D. A. Bellido-Aguilar, M. Safaripour, H. Kim, J. J. Watkins, A. J. Crosby, D. C. Webster, and A. B. Croll, “Silicone elastomers and the Persson-Brener adhesion model,” *The Journal of Chemical Physics*, vol. 159, p. 184708, 11 2023.

[131] K. Kendall, “Thin-film peeling-the elastic term,” *Journal of Physics D: Applied Physics*, vol. 8, p. 1449, 1975.

[132] T. Jules, F. Lechenault, and M. Adda-Bedia, “Plasticity and aging of folded elastic sheets,” *Phys. Rev. E*, vol. 102, p. 033005, Sep 2020.

[133] D. H. Kaelble, “Theory and analysis of peel adhesion: Rate-temperature dependence of viscoelastic interlayers,” *J. Colloid Sci.*, vol. 19, pp. 413–424, 1964.

[134] A. N. Gent and J. Schultz, “Effect of wetting liquids on the strength of adhesion of viscoelastic materials,” *Journal of Adhesion*, vol. 3, pp. 281–294, 1972.

[135] E. H. Andrews, A. J. Kinloch, and H. W. Melville, “Mechanics of adhesive failure. i,” *Proceedings of the Royal Society of London. A. Mathematical and Physical Sciences*, vol. 332, no. 1590, pp. 385–399, 1973.

[136] Q. Han, L. Zhang, and Y. Wu, “Relationship between dynamic fatigue crack propagation properties and viscoelasticity of natural rubber/silicone rubber composites,” *RSC advances*, vol. 9, no. 51, pp. 29813–29820, 2019.

[137] L. Brely, F. Bosia, and N. M. Pugno, "The influence of substrate roughness, patterning, curvature, and compliance in peeling problems," *Bioinspir. Biomim.*, vol. 13, p. 26004, 2018.

[138] T. Elder, T. Twohig, H. Singh, and A. B. Croll, "Adhesion of a tape loop," *Soft Matter*, vol. 16, pp. 10611–10619, 2020.

[139] E. Kroner, R. Maboudian, and E. Arzt, "Adhesion characteristics of pdms surfaces during repeated pull-off force measurements," *Adv. Eng. Mater.*, vol. 12, pp. 398–404, 2010.

[140] E. Kroner, D. R. Paretkar, R. M. McMeeking, and E. Arzt, "Adhesion of flat and structured pdms samples to spherical and flat probes: A comparative study," *J. Adhesion*, vol. 87, pp. 447–465, 2011.

[141] A. Galliano, S. Bistac, and J. Schultz, "Adhesion and friction of pdms networks: molecular weight effects.," *J. Colloid interf. Sci.*, vol. 265, pp. 372–379, 2003.

[142] S. Vlassov, S. Oras, M. Antsov, I. Sosnin, B. Polyakov, A. Shutka, M. Y. Krauchanka, and L. Dorogin, "Adhesion and mechanical properties of pdms-based materials probed with afm: A review," *Rev. Adv. Mater. Sci.*, vol. 56, pp. 62–78, 2018.

[143] S. Perutz, E. Kramer, J. Baney, C.-Y. Hui, and C. Cohen, "Investigation of adhesion hysteresis in poly(dimethylsiloxane) networks using the jkr technique," *J. Poly. Sci. B: Poly. Phys.*, vol. 36, pp. 2129–2139, 1998.

[144] F. Carrillo, S. Gupta, M. Balooch, S. J. Marshall, G. W. Marshall, L. Pruitt, and C. M. Puttlitz, "Nanoindentation of polydimethylsiloxane elastomers: Effect of crosslinking, work of adhesion, and fluid environment on elastic modulus," *J. Mater. Res.*, vol. 20, pp. 2820–2830, 2005.

[145] Y. Cao, D. Yang, and W. Soboyejoy, “Nanoindentation method for determining the initial contact and adhesion characteristics of soft polydimethylsiloxane,” *Journal of Materials Research*, vol. 20, no. 8, p. 2004–2011, 2005.

[146] F. Schneider, T. Fellner, J. Wilde, and U. Wallrabe, “Mechanical properties of silicones for MEMS,” *Journal of Micromechanics and Microengineering*, vol. 18, p. 065008, apr 2008.

[147] I. D. Johnston, D. K. McCluskey, C. K. L. Tan, and M. C. Tracey, “Mechanical characterization of bulk sylgard 184 for microfluidics and microengineering,” *J. Micromech. Microeng.*, vol. 24, p. 035017, 2014.

[148] T. K. Kim, J. K. Kim, and O. C. Jeong, “Measurement of nonlinear mechanical properties of pdms elastomer,” *Microelectronic Engineering*, vol. 88, no. 8, pp. 1982 – 1985, 2011. Proceedings of the 36th International Conference on Micro- and Nano-Engineering (MNE).

[149] T. Rahimzadeh, E. M. Arruda, and M. Thouless, “Design of armor for protection against blast and impact,” *Journal of the Mechanics and Physics of Solids*, vol. 85, pp. 98–111, 2015.

[150] H. Yasuda, Y. Miyazawa, E. G. Charalampidis, C. Chong, P. G. Kevrekidis, and J. Yang, “Origami-based impact mitigation via rarefaction solitary wave creation,” *Science advances*, vol. 5, no. 5, p. eaau2835, 2019.

[151] A. Ciampaglia, D. Fiumarella, C. B. Niutta, R. Ciardiello, and G. Belingardi, “Impact response of an origami-shaped composite crash box: Experimental analysis and numerical optimization,” *Composite Structures*, vol. 256, p. 113093, 2021.

[152] M. A. Reyes-Martinez, E. P. Chan, C. L. Soles, E. Han, K. A. Murphy, H. M. Jaeger, D. R. Reid, and J. J. de Pablo, “Tuning the mechanical impedance of disordered networks for impact mitigation,” *Soft Matter*, vol. 18, no. 10, pp. 2039–2045, 2022.

[153] L. Yuan, H. Shi, J. Ma, and Z. You, “Quasi-static impact of origami crash boxes with various profiles,” *Thin-Walled Structures*, vol. 141, pp. 435–446, 2019.

[154] J. Harris and G. McShane, “Impact response of metallic stacked origami cellular materials,” *International Journal of Impact Engineering*, vol. 147, p. 103730, 2021.

[155] K. Efimenko, W. E. Wallace, and J. Genzer, “Surface modification of sylgard-184 poly (dimethyl siloxane) networks by ultraviolet and ultraviolet/ozone treatment,” *Journal of colloid and interface science*, vol. 254, no. 2, pp. 306–315, 2002.

[156] M. K. Chaudhury and G. M. Whitesides, “Direct measurement of interfacial interactions between semispherical lenses and flat sheets of poly (dimethylsiloxane) and their chemical derivatives,” *Langmuir*, vol. 7, no. 5, pp. 1013–1025, 1991.

[157] D. A. Hanaor, E. F. Johnson, S. Wang, S. Quach, K. Dela-Torre, Y. Gan, and L. Shen, “Mechanical properties in crumple-formed paper derived materials subjected to compression,” *Heliyon*, vol. 3, no. 6, 2017.

[158] W. Humphrey, A. Dalke, and K. Schulten, “Vmd: visual molecular dynamics,” *Journal of molecular graphics*, vol. 14, no. 1, pp. 33–38, 1996.

[159] M. C. Payne, M. P. Teter, D. C. Allan, T. Arias, and a. J. Joannopoulos, “Iterative minimization techniques for ab initio total-energy calculations: molecular dynamics and conjugate gradients,” *Reviews of modern physics*, vol. 64, no. 4, p. 1045, 1992.

APPENDIX

Supplemental Information for Crumpled Kirigami[1]

A.1. Overview of Sheet Model Being Cut and Molecular Dynamics Simulations

Based on our previously developed CG graphene model,(101) we performed coarse-grained molecular dynamics (CG-MD) simulations to explore the crumpling and uniaxial compression behaviors of graphene sheets with cuts. Informed from the underlying atomic graphene model, as shown in Figure S1a, the employed CG model of graphene is derived based on a 4-to-1 mapping scheme to preserve the hexagonal lattice geometry, where each CG bead with a mass of 48 g/mol represents four carbon atoms. As listed in Table S1, the CG force field of the CG model includes bonded interactions, i.e., bonds V_b (d), angles $V_a(\theta)$, dihedrals $V_d(\phi)$, and pairwise non-bonded interactions $V_n b$ (r). Specifically, the bond, angle, and dihedral interactions are used to describe the elastic modulus and fracture strength, shear modulus, and bending rigidity of the graphene sheet respectively; the adhesion energy of the sheet is captured by the pair-wise non-boned interaction. Further details on the development of the CG model can be found in the earlier study.(101)

---

[1] This is published as a peer-reviewed article and reproduced from Ref.(74) with permission from the Royal Society of Chemistry.

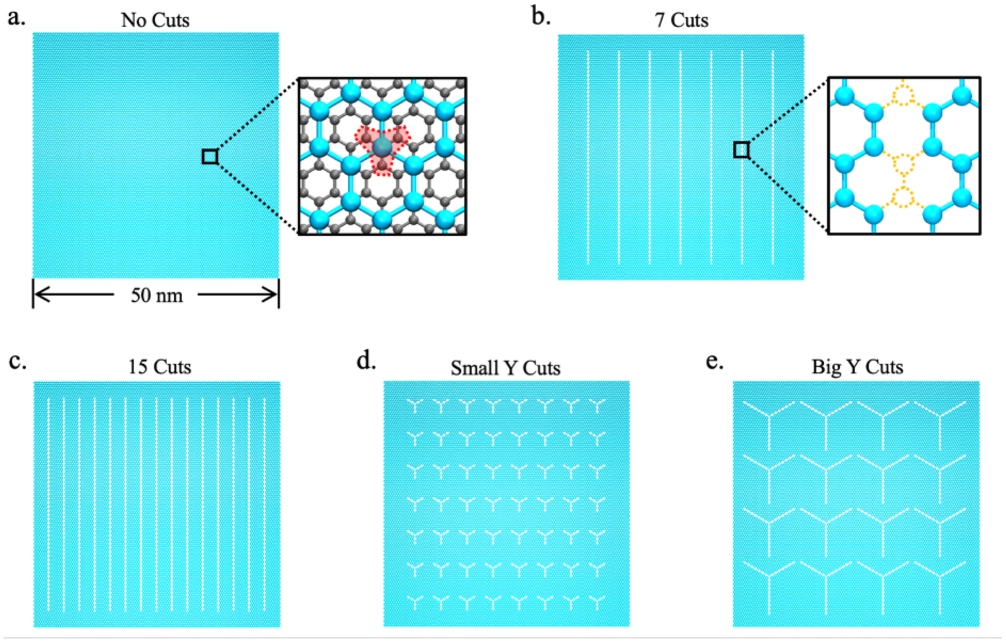

Figure A1. Representation of CG models of graphene sheets with different cutting patterns (kirigami patterns), i.e., a.) no cuts, b.) 7 cuts, c.) 15 cuts, d.) small Y cuts, and e.) big Y cuts, respectively. The zoom-in in a.) shows the 4-to- 1 mapping scheme of the CG graphene model, where the four connected carbon atoms (black atoms) are grouped into a CG bead (cyan bead) as highlighted in the red region. The zoom-in in b.) shows the cut pattern created by deleting the specific CG beads (orange dashed open circles)

Table A1. Functional forms and interaction parameters of the CG graphene model.

Interaction	Function form	Parameters
Bond	$V_b(d) = D_0[1 - e^{-\alpha(d-d_0)}]^2$for $d < d_{cut}$	$D_0 = 196.38$ kcal/mol $\alpha = 1.55$ Å $d_0 = 2.8$ Å $d_cut = 3.25$ Å
Angle	$V_a(\theta) = k_\theta(\theta - \theta_0)^2$	$k_\theta = 409.4$ kcal/mol $\theta_0 = 120°$
Dihedral	$V_d(\phi) = k_\phi[1 - \cos 2\phi]^2$	$k_\phi = 4.15$ kcal/mol
Non-Dihedral	$V_{nb}(r) = 4\epsilon[(\frac{\sigma}{r})^{12} - (\frac{\sigma}{r})^6]$ for $r < r_{cut}$	$\epsilon = 0.82$ kcal/mol $\sigma = 3.46$ Å $r_{cut} = 12$ Å

In this study, we investigated the internal structure and compressive strength of crumpled graphene sheets without cutting (no cuts) and with 7 cuts, 15 cuts, small Y cuts and big Y cuts patterns (fig. A1). All the MD simulations are carried out using an open-source software package Large-scale Atomic/Molecular Massively Parallel Simulator (LAMMPS),(105) and the visualization of the MD simulation is achieved by Visual Molecular Dynamics (VMD).(158) Specifically, the energy minimization, equilibrium simulation, and crumpling simulation of the sheet are carried out sequentially before uni-axial compression and unloading simulations. First, the square graphene sheet with an edge length of 50 nm is placed horizontally (xy-plane) in the center of the simulation box, which has dimensions of 500 nm×500 nm×500 nm; the periodic boundary conditions are applied to the system in all directions, with time step and simulated temperature of 6 fs and 300 K, respectively. The iterative conjugate gradient algorithm is utilized for the energy minimization,(159) and 2 ns of NVT ensemble is simulated for the equilibrium of the system, which results in the final convergence of the total potential energy of the system to a nearly constant value.

a. No Cuts

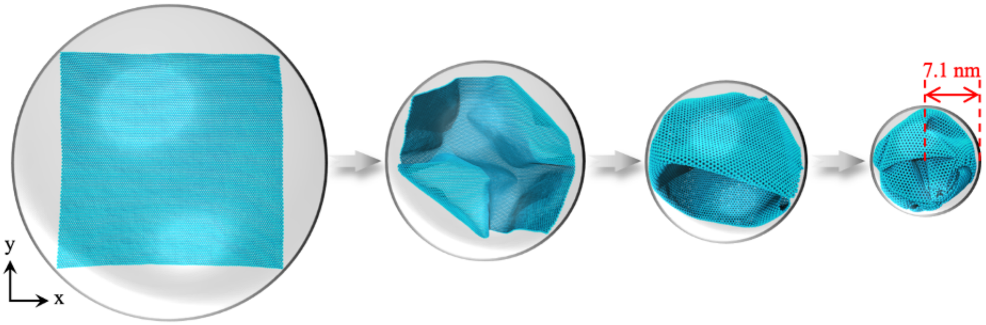

b. 15 Cuts

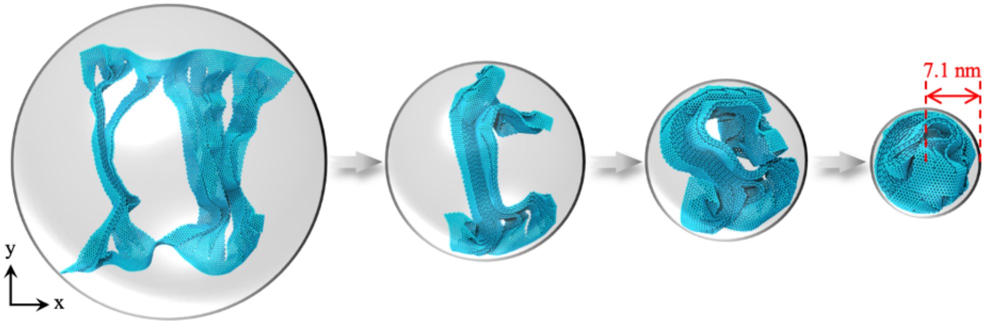

Figure A2. Schematic of the MD simulation of the crumpling process for CG graphene sheet with a.) no cuts and b.) 15 cuts. Here, a confining sphere containing the sheet model is used to compress the sheet. As the radius of the confining sphere continuously decreases, the sheet gradually gets crumpled to the final sphere-like structure with a radius of 7.1 nm.

Then, as shown in Figure A2 , the crumpling process is achieved by crumpling the sheet with a confining sphere containing the model. That is, a repulsive force $F_c(r_i)$ from the boundary of confining sphere is applied to the sheet within a certain cutoff distance when the sheet is inside the confining sphere. The confining force $F_c(r_i)$ can be written as:

$$F_c(r_i) = \begin{cases} -Kc(r_i - R_c)^2 & \text{for} \quad r_i \geq R_c \\ 0 & \text{for} \quad r_i < R_c \end{cases} \tag{A.1}$$

where R_c, r_i, K_c are the radius of the confining sphere, radial distance from the i^{th} bead to the center of the confining sphere, spring force constant ($K_c = 2.31 \times 10^5$ kcal/mol/nm^3), respectively. The crumpling process of the sheet is achieved by decreasing the radius of the confining sphere R_c at a certain speed (i.e., $50m/s$). More details on the sheet crumpling simulations can be found in earlier studies.(99; 103; 104)

It can be observed from Figure A2 that the pristine graphene sheet (no cuts) basically maintains a flat configuration in the initial equilibrium state, and it shows significant edge bending and self-folding behaviors during the crumpling process, which can also be learned from our previous studies.(99; 103) Interestingly, for the graphene sheet with 15 cuts, it develops a stacked lamellar structure due to adhesion in the initial equilibrium state, and the stacking behavior intensifies and finally compresses into a crumpled sphere upon crumpling. It is evident that at the molecular level, the cutting controls the final crumpled structure of the graphene sheet by affecting its initial configuration and crumpling behavior.

Upon obtaining the final crumpled spherical structure, we further conduct uniaxial compression and unloading simulations. To simulate the compression and unloading tests in the experiment, we replace the confining sphere with a confining cylinder of equal radius, whose height is equal to the diameter of the confining sphere. As shown in Figure A3, while maintaining the crumpled state (cyan) in the confining cylinder, two parallel rigid plates (gray) are added at the two ends of the z-axis at a distance 3.46 Åfrom the crumpled model, both of which are 20 nm×20 nm in size and the same material properties as the crumpled model. Afterward, the compression and unloading simulation of the crumpled model is achieved by defining a specific moving speed for the two plates with opposite or opposing directions, respectively. We specify the minimum separation between the two plates to be roughly 5 nm, which is to disregard the non-bonded interactions between the plates. When applying equation $F = Et^2(2R_0/H)^{\alpha}$, we choose parameter σ of the non-boned interaction as the thickness t of the model, where σ=3.46Åis a length scale parameter related to the equilibrium distance of two nonbonded beads. In our study, thirteen different compression speeds ranging from 40 m/s to 100 m/s are employed and ten independent simulations are performed for each compression speed, to obtain the average value of the target properties of the crumpled model with different cutting patterns.

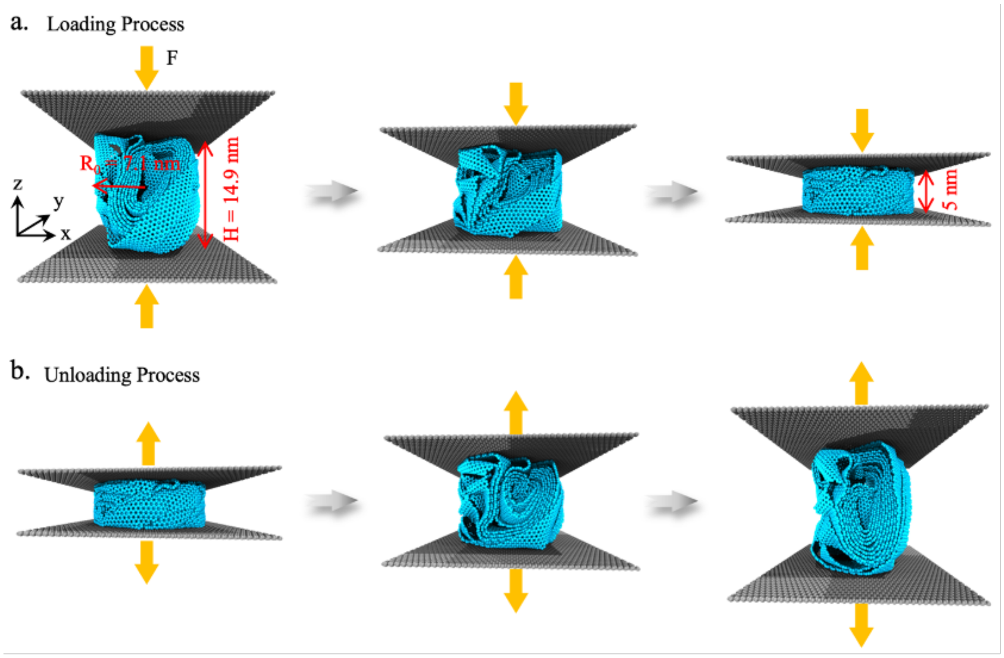

Figure A3. Schematics of the MD simulations for a.) uniaxial compression and b.) unloading simulations. Here, the crumpled sheet with a radius of $R_0(R_0 = 7.1nm)$ is disposed between two rigid and parallel plates; the separation between the two plates is H. The compression and unloading simulations of the crumpled model is achieved by defining a specific moving speed for the two plates with opposite or opposing directions, respectively.

A.2. Discussion of Line Statistics

In our manuscript we discuss mainly the angular distribution of highly curved features fit by straight line segments. We do so because our analysis of both the experimental and simulated lines contain unavoidable error, and the angular distribution is the least affected by these errors. Error occurs because all high curvature structures may not form straight lines (though we fit with line segments), may not abruptly start or stop (they may taper beyond where our line segments fit), and may fluctuate in curvature from one end to the other (i.e. is it one long line or two short line segments oriented in the same direction?). Both programs used in analysis would thus have to make choices deal with these issues that will always be, in some view, imperfect. This said, data generated by these two separate analysis programs (one for simulations, one for experiments) is still meaningful, though in a more qualitative sense. Therefore, we present some additional detail of the distributions here for the interested reader.

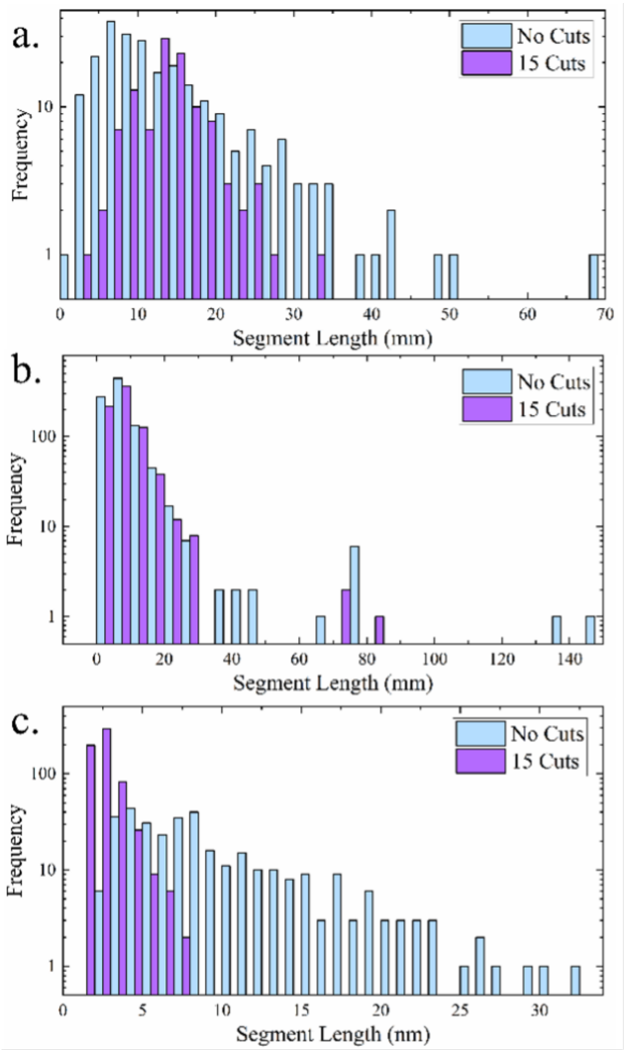

Figure A4. Histograms of high curvature segment lengths. a. A low density crumpled paper sheet, both uncut and cut 15 times. The cut sample shows a reduced 'tail' of longer length structures. b. A high density paper crumple. Again, a reduction in long segments is evident. c. Segments from a typical MD simulations. Simulations also show a large reduction in long segments when cuts are present.

Figure A4 shows typical distributions of lengths of high curvature structures for low density, high density and simulated crumples. For all data we see a similar loss of long structures in cut sheets, directly vindicating the main goal of our study. Interestingly, the distributions are fairly similar between cut and uncut films at smaller line lengths. The higher density data of the simulations, however, shows a peak at lower line lengths for cut sheets than uncut sheets. We believe that the difference is likely related to the plasticity of the paper sheets. In short, they are much less free to re-arrange as additional stress is added to the system.

Additionally, both the number of segments and the total length of high curvature segments is larger in uncut sheets when compared to cut sheets at similar densities. Given that there is some evidence that the total length of high curvature features correlates with the effective stiffness of crumpled matter, this observation can explain the small differences in effective modulus observed in our study (85). In summary, cuts affect the structure of the high-curvature network within a crumple by changing the angular distribution and removing long range structure, but does not significantly change the overall mechanics of the crumpled sheet.

A.3. Discussion of Total Line Length

Gottesman et. al (85) have noted that the total line length (of creases measured in uncrumpled sheets similar to what is presented in this manuscript) correlates well with the compressive behaviour of a crumple. Unsurprisingly we also find that the total length of lines is proportional to the peak density of the crumple (note: density for us is more reasonable than a scaled gap as in (85) because we do not fix radius as they do). While Gottesman et al. only examined pristine sheets, we find very little difference with the cut sheets, save that the lengths at comparable densities are slightly smaller. As the simulations define “lines” differently than the experiment, the trends are slightly different as one would expect. Figure A5 shows the basic result.

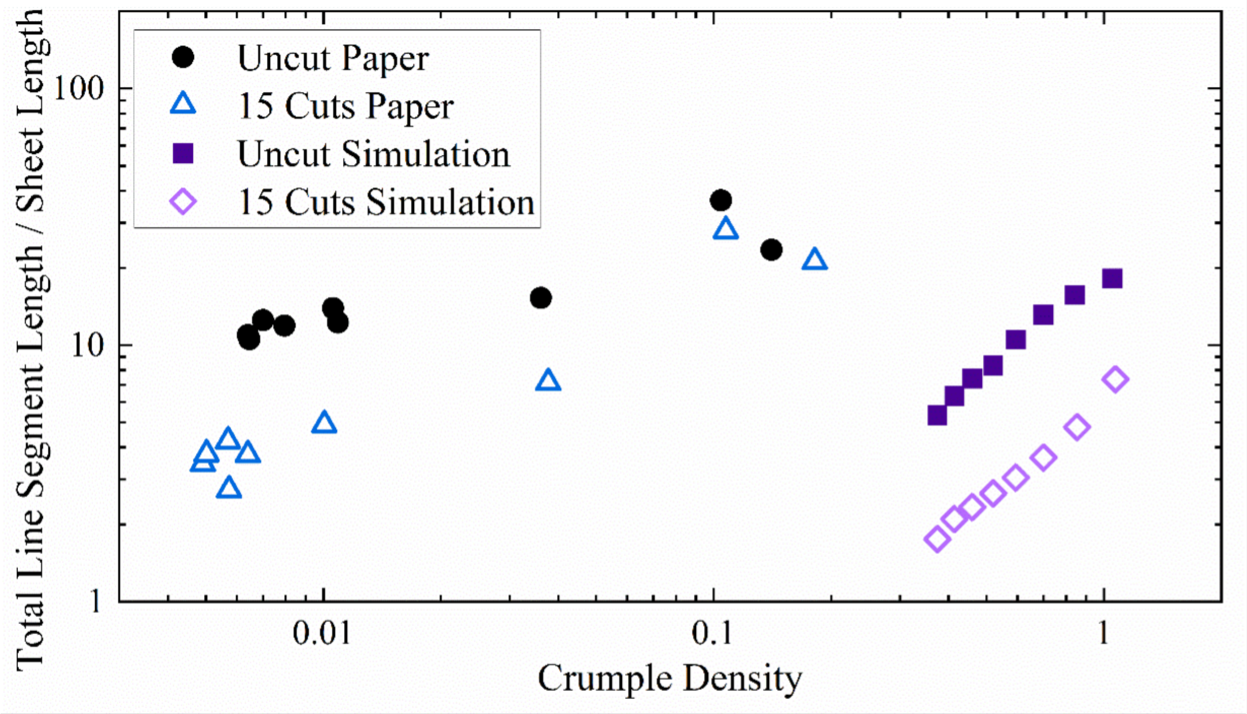

Figure A5. Total line length as a function of crumple density. Both paper and simulated data show an upward trend with density. Simulations and paper crumples differ because the way a line is measured differs between the two.

A.4. Discussion on d-cone Population

It is difficult to define, from the uncrumpled sheet, where exactly d-cones may have been at the point of peak compression. However, it is reasonable to assume this number would be proportional to the number of line-ends observed in the analysis of the uncrumpled sheet. One observes that many lines will begin or end on a cut or sheet edge, which would likely mean that one d-cone has escaped the sheet and exists only virtually. Given this hypothesis, it is then possible to examine changes in the population of d-cones by simply examining the marked sheets (in experiment or theory).

As a preliminary step in such an analysis, Figure S6 shows the fraction of virtual to total d-cones in cut and uncut sheets. Uncut sheets at various crumpled densities tend to have less than 5% of lines interacting with a sheet edge. On the other hand, cut sheets typically have somewhere between 40% to 90% of lines interacting with an edge, trending to higher numbers at lower density. Clearly the "current" location of d-cones is not significant to the crumple's resistance to compression as, once again, very little difference is noted in terms of macroscopic compression of the crumple. This is not inconsistent with the conceptual model discussed in the manuscript, because the folds still represent the path a d-cone has taken through the sheet.

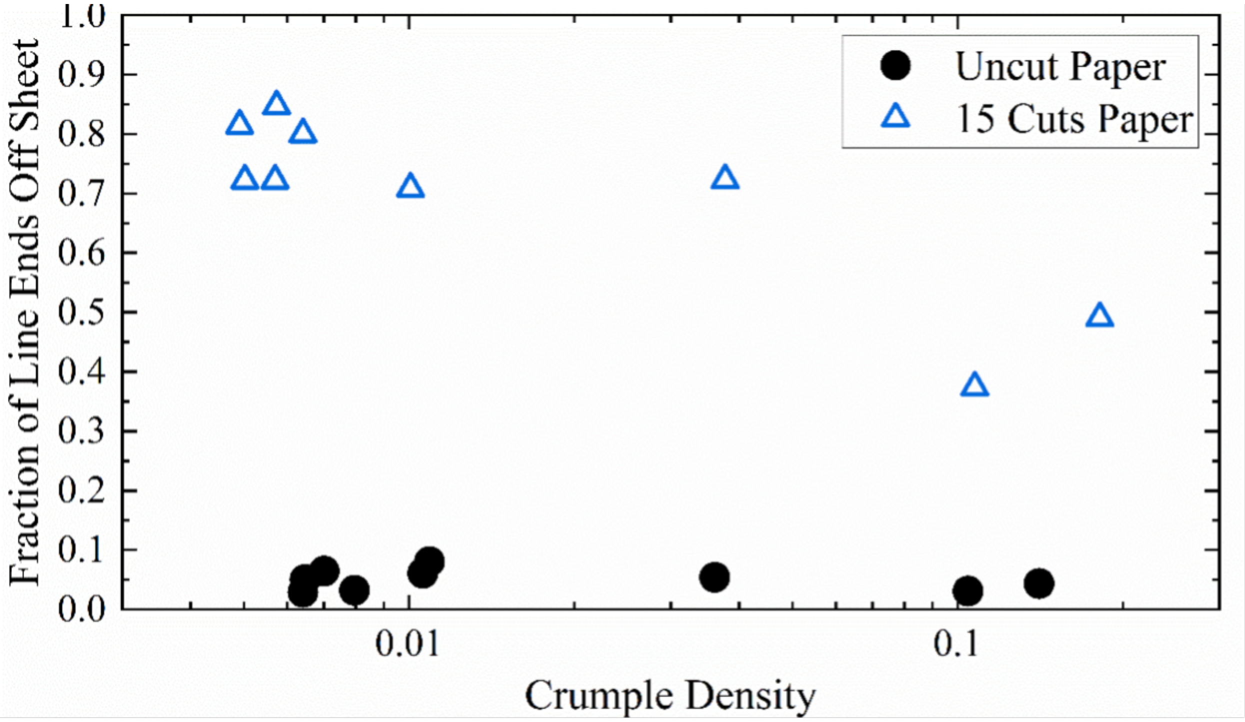

Figure A6. Fraction of line ends occurring off the sheet as a function of crumple density.

A.5. Discussion of Statistical Tests

In the main manuscript we claim to see very little difference between cut and uncut crumpled sheets based on subjective observation of quantitative data extracted from force-displacement curves. However, while clear from observing the presented raw data, for example, the distribution of power-law fit exponents, some readers might be unsatisfied without a quantitative measure. Therefore, we present here a quantitative verification of our conjecture by considering p-test results comparing the null hypothesis (cut sheets are not statistically different from uncut sheets) with the data. Specifically, we consider distributions of power-law fit exponents (α) between cut and uncut sheets. For paper, we find (using a Wilcoxon rank sum test implemented in MATLAB) that p = 0.80 when comparing the power-law exponent of cut and uncut paper crumples. This indicates that there is no significant difference between the two populations as the p value is considerably above any typical cut-off (say p=0.05). For polycarbonate we find p = 0.38 and in the simulations we find $p = 1.27 \times 10^{-34}$. Thus, only the simulations have the statistical power to clearly differentiate the two populations, likely due to the incredible control of sample-to-sample variation possible in a simulation.